

ABSTRACT

CYRIAC, ROSEMARY. Wind and Plume Driven Circulation in Estuarine Systems. (Under the direction of Dr. Joel Casey Dietrich).

Mechanistic models with high spatial resolution are useful tools to represent the dynamic and non-linear feedbacks between tides, winds and freshwater inflows in the nearshore and to predict future conditions. In this thesis, several aspects of the wind- and river-plume-driven hydrodynamics and transport in estuarine systems are examined through barotropic and baroclinic models.

The study begins with an application of a state-of-the-art storm surge model to examine the effects of meteorological forecast errors on coastal flooding predictions along the North Carolina (NC) coastline. As Hurricane Arthur (2014) moved over Pamlico Sound, it increased the total water levels to 2.5 m above sea level; this water pushed first into the river estuaries and against the inner banks, and then moved eastward to threaten the sound-side of the barrier islands. It is hypothesized that a combination of storm track and intensity errors caused errors in the forecast winds and water levels along the NC coast during Arthur. Model results reveal that, as the forecast storm track and intensity errors increase, the errors in forecast wind speeds also increase, but the errors in forecast water levels remain relatively the same, signifying the non-linear response of the coastal ocean to wind effects. By separating the forecast errors in storm track and storm strength, this study quantifies their effects on the coastal ocean, which provides useful guidance for designing relevant forecast ensembles.

In addition to flooding impacts, storms can also cause dramatic changes in estuarine salinities, which can negatively impact estuarine ecosystems. Baroclinic models are useful tools for predicting estuarine salinity response under changing environmental conditions. In the present work, the features of wind- and plume-driven circulation in the vicinity of Choctawhatchee Bay (CB) and Destin Inlet, Florida, are analyzed with a recently-enhanced, three-dimensional, baroclinic model. Satellite imagery showed a visible brackish surface plume at Destin during low tide. The goal of the present study is to quantify variability in the plume signature due to changes in tidal and wind forcing. Modeled tides, salinities and plume signature are validated against in-situ observations and satellite imagery and then applied to analyze plume response in two scenarios. In the first case, model plume behavior is analyzed on successive days of near-constant

tidal amplitudes and changing wind directions due to passing cold fronts. In the second case, plume response is investigated during consecutive days of neap-spring variability in the tides and near-constant wind speeds. Model results reveal a larger plume during spring tides and periods of weak wind forcing. Offshore winds enhance the north-south expansion of the plume, whereas onshore winds restrict the plume to the coastline.

Finally, the validated model is applied to identify salinity and transport characteristics within CB. Based on limited studies in the past, it is hypothesized that CB is a stratified system with limited flushing and zones of distinct salinity gradients. These hypotheses are tested by analyzing bay salinities from the validated model during a period of low river flows. Model surface salinities indicate brackish conditions (20 psu) throughout the bay except for near the river mouth. Stratification (10 – 15 psu) within the bay is high and unaffected by the passage of cold fronts and neap-spring tidal variability. The residence time within the Choctawhatchee Bay, an important indicator of estuarine health, is computed via particle tracking and is equal to roughly 40 days.

This work advances the scientific understanding of multiple aspects of estuarine circulation including wind-driven surge and flooding, brackish plume behavior through inlets and onto the shelf, and salinity transport and stratification properties within estuaries. Research findings lead to a better understanding of estuarine response under a wide range of atmospheric conditions, and the resulting technologies will be useful for oil spill response operations, fisheries and pollution management.

Wind and Plume Driven Circulation in Estuarine Systems

by
Rosemary Cyriac

A dissertation submitted to the Graduate Faculty of
North Carolina State University
in partial fulfillment of the
requirements for the Degree of
Doctor of Philosophy

Civil Engineering

Raleigh, North Carolina

2018

APPROVED BY:

Margery Overton

Ruoying He

Zhilin Li

Clint Dawson (External Member)

Joel Casey Dietrich
Chair of Advisory Committee

DEDICATION

To the pursuit of the True, the Good and the Beautiful

Which motivates all human endeavors

&

To my parents Mary Joseph and Cyriac Kuriakose, and my husband Josin Tom

In gratitude for their unconditional love

&

To my family and friends

For all the joy they bring to my life

BIOGRAPHY

Rosemary Cyriac was born in Thiruvananthapuram, Kerala, India to Mary Joseph and Cyriac Kuriakose. She grew up there and did all her schooling in Holy Angels' ISC School. After graduating high school, Rosemary pursued an undergraduate degree in Civil Engineering at National Institute of Technology, Calicut. She then started graduate studies in Water Resources Engineering at Indian Institute of Technology Bombay. She was introduced to numerical modeling through her Masters thesis on simulation optimization models for ground water systems. She enjoyed developing mathematical models to describe fluid flow and decided to pursue doctoral studies to learn more. Rosemary arrived in Raleigh, North Carolina to pursue her doctoral studies in Coastal Engineering at North Carolina State University. With the help of her advisor, Dr. Casey Dietrich, Rosemary was able to leverage her past experience in finite element modeling of ground water flow for building unstructured grid based coastal models and has thoroughly enjoyed her research experience.

ACKNOWLEDGEMENTS

I am immensely grateful to the many individuals who have contributed to my professional and personal development while at graduate school. I am fortunate to have as a mentor and advisor, Dr. Casey Dietrich, who has taught me many lessons in coastal modeling and science communication and helped me grow into the researcher that I am today. He was always an available, patient and approachable advisor, who showed a genuine interest in my success. I will especially remember his regular words of affirmation and positive feedback, which kept me motivated through the rigors of graduate school life. He will always be a role model to me.

I am also thankful to members of the ADCIRC community, especially Dr. Clint Dawson, Dr. Cheryl Ann Blain, Dr. Kendra Dresback, Dr. Arash Fathi, Dr. Rick Luettich and Dr. Jason Fleming for their active collaboration and constructive feedback at various stages of my research. I also thank members of my thesis committee, Dr. Ruoying He and Dr. Zhilin Li, for their support towards the completion of my doctoral program. I would also like to acknowledge the North Carolina Sea Grant and the Gulf of Mexico Research Initiative for providing the research funds that made my PhD possible. I also thank the SCOPE team of the Consortium for Advanced Research on the Transport of Hydrocarbons (CARTHE) and the Choctawhatchee Basin Alliance for their field data, which was valuable to validate my model.

One of the most valuable part of my PhD experience was being a member of the coastal team at NCSU. I have learned a lot and been enriched through my interactions with the coastal faculty, namely Dr. Elizabeth Sciaudone, Dr. Alejandra Ortiz, Dr. Margery Overton and Dr. Billy Edge. Thank you for sharing your knowledge and your friendly words of advice and encouragement. I will always cherish the many friendships I made in Mann 428. Many thanks: to Lily who walked closely with me since my first day and cheered me on at every stage of my PhD journey; to Ayse, Nelson, Ajimon and Alireza for our friendship, afternoon coffee routines and conversations about the struggles and triumphs of graduate school life. All of you occupy a special place in my heart. It was also a pleasure to work closely with my mentee Emerina Kelly, whose hard work and diligence produced deliverables that were valuable to my research.

I also remember gratefully, my Masters Thesis advisor, Dr. Ashok Kumar Rastogi, who introduced me to the world of finite element modeling and helped me build a foun-

dation in computational fluid mechanics.

While in graduate school, I had the privilege of being surrounded and supported by many close friends. I thank my friends at the NCSU Catholic Campus Ministry, especially Joe, Lori, Indunil, Raisa and Mario and others in our CCM Grads community for their prayers and words of encouragement and support throughout my PhD journey. Many thanks to my friends in the Malayali community at NCSU, my former flat mates Haritha and Sudarshana, and my neighbors Vishnu, Hari and Moses for our friendship and all the memories we share together, which made my graduate school life memorable. I am also grateful to Jismi, Merlin, Dancho, Indu, Maneesha, Anusha, Neethu, Gayathri, Sharada and Leah, for sustaining our long distance friendships and cheering me on through numerous online conversations over the last five years.

Throughout this journey, my most honest critic and biggest cheerleader has been my husband, Josin Tom, whose unwavering love is my greatest comfort. From thousands of miles away, my parents, Mary Joseph and Cyriac Kuriakose, and my brother Antony Cyriac has walked every step of this journey with me. I am grateful for the unconditional love they and the rest of my family showers on me.

Above all, I thank God, for His Divine Providence, which led me to graduate school and sustains me throughout life.

TABLE OF CONTENTS

LIST OF TABLES	viii
LIST OF FIGURES	ix
Chapter 1 Introduction	1
Chapter 2 Variability in Coastal Flooding Predictions due to Forecast Errors during Hurricane Arthur	6
2.1 Overview	6
2.2 Introduction	6
2.3 Hurricane Arthur (2014)	11
2.3.1 Synoptic History	11
2.3.2 Observations	13
2.4 Methods	13
2.4.1 Models for Storm-Induced Waves and Surge	13
2.4.2 Atmospheric Forcing	14
2.4.3 Swapping Information Between HWind and GAHM	16
2.4.4 Unstructured Mesh Describing Coastal NC	18
2.5 Results and Discussion	19
2.5.1 Validation for Atmospheric Products Available Before and After the Storm	19
2.5.2 Error due to Storm Track	34
2.5.3 Error due to Storm Size and Intensity	37
2.6 Summary	40
Chapter 3 A 3D Baroclinic Flow Model for the Choctawhatchee Bay and Destin Inlet System	43
3.1 Overview	43
3.2 Introduction	43
3.3 Methods	46
3.3.1 3D Hydrodynamic Model	46
3.3.2 Unstructured Mesh	49
3.3.3 Physical Forcings	51
3.3.4 Model Setup	52
3.4 Model Validation	53
3.4.1 Water Levels	53
3.4.2 Vertical Salinities	55
3.4.3 Comparisons to Satellite Imagery	60
3.4.4 Drifter Movement	62

3.5	Summary	64
Chapter 4 Wind and Tide Effects on Salinity Characteristics in Choctawhatchee Bay and the Adjacent Continental Shelf . .		67
4.1	Overview	67
4.2	Introduction	67
4.3	SCOPE Observations near the Choctawhatchee Bay System	71
4.4	Variability in Ebb- and Flood-Phase Plume Signature	74
4.4.1	Wind Effects on Plume Geometry	74
4.4.2	Tide Effects on Plume Geometry	76
4.4.3	Discussion	77
4.5	Estuarine Salinities	79
4.5.1	Inlet Salinities	79
4.5.2	Surface Salinities	83
4.5.3	Stratification	86
4.6	Residence Time	89
4.7	Summary	91
Chapter 5 Concluding Remarks		93
APPENDIX		113
Appendix A	Kalpana Visualization Tool	114

LIST OF TABLES

Table 2.1	Summary of selected locations along the North Carolina coast referenced in the text.	9
Table 2.2	Summary of station locations at which measurements of wind speeds and water levels are available for the study period.	10
Table 2.3	Summary of storm tracks, wind and pressure fields used in each simulation. Each forecast simulation uses information from the corresponding NHC forecast advisory, e.g., <i>GAHM(4)</i> uses parameters from NHC forecast advisory 4 to construct wind and pressure fields using GAHM. For hybrid simulations, the track and storm information comes from different sources, e.g., <i>GAHM(12,HWind)</i> uses the storm track from NHC forecast advisory 12, but with parameters for storm size and intensity from the hindcast <i>HWind</i> simulation.	19
Table 2.4	Error statistics for the three hindcast simulations, for both wind speeds and water levels, with comparisons to the available observations in the region, and at every computational point with depths less than 10 m.	24
Table 3.1	Error statistics at selected stations.	60

LIST OF FIGURES

Figure 2.1	Observation stations used for model validations (indicated by numbers) and other important geographic locations along the NC coast that are referenced in the paper (indicated by alphabets). Please refer to Table 2.2 for detailed description. Lines indicate storm track predictions during advisories 4 (pink), 8 (blue) and 12 (cyan) issued by the NHC 54, 30 and 12 hr before Arthur made landfall along the NC coast. The best track (red line) issued after the storm by the NHC and the storm track represented by <i>HWind</i> (light green) is also shown.	8
Figure 2.2	Evolution by forecast advisory number of Arthur’s (left) forecast landfall error (km) at 2014/07/04/0300 UTC, and (right) power dissipation (10^{12} watts) averaged over 24 hr surrounding its initial landfall.	12
Figure 2.3	Bathymetry and topography contours (m, relative to mean sea level) for the NC9 mesh used by the ASGS for generating storm surge forecasts during Hurricane Arthur (2014).	17
Figure 2.4	Hindcasts of wind speeds (m/s) during Arthur in coastal North Carolina. Rows correspond to: (top) <i>HWind</i> , (middle) <i>GAHM(BT)</i> , and (bottom) <i>GAHM(HWind)</i> . Columns correspond to: (left) wind speeds at 2014/07/04/0600 UTC, (center) maximum wind speeds, and (right) difference in maximum wind speeds relative to <i>HWind</i>	21
Figure 2.5	Time series of observed and predicted wind speeds (m/s) from hindcast simulations at 10 stations with locations described in Table 2.2 and Figure 2.1. Gray circles indicate observations, and the lines indicate predictions from (dotted) <i>HWind</i> , (solid) <i>GAHM(BT)</i> , and (dashed) <i>GAHM(HWind)</i>	22
Figure 2.6	Hindcasts of water levels (m) during Arthur in coastal North Carolina. Rows correspond to: (top) <i>HWind</i> , (middle) <i>GAHM(BT)</i> , and (bottom) <i>GAHM(HWind)</i> . Columns correspond to: (left) water levels at 2014/07/04/0600 UTC, (center) maximum water levels, and (right) difference in maximum water levels relative to <i>HWind</i>	25
Figure 2.7	Time series of observed and predicted water levels (m) from hindcast simulations at 8 stations with locations described in Table 2.2 and Figure 2.1. Gray circles indicate observations, and the lines indicate predictions from (dotted) <i>HWind</i> , (solid) <i>GAHM(BT)</i> , and (dashed) <i>GAHM(HWind)</i>	27

Figure 2.8	Forecasts of winds (m/s) and water levels (m) during Arthur in coastal North Carolina. Rows correspond to: (top) <i>GAHM(4)</i> , (middle) <i>GAHM(8)</i> , and (bottom) <i>GAHM(12)</i> . Columns correspond to: (left) maximum wind speeds, and (right) maximum water levels.	30
Figure 2.9	Time series of observed and predicted wind speeds (m/s) from forecast simulations at 10 stations with locations described in Table 2.2 and Figure 2.1. Gray circles indicate observations, and the lines indicate predictions for (lighter gray) <i>GAHM(4)</i> , (darker gray) <i>GAHM(8)</i> , and (black) <i>GAHM(12)</i>	31
Figure 2.10	Time series of observed and predicted water levels (m) from forecast simulations at 8 stations with locations described in Table 2.2 and Figure 2.1. Gray circles indicate observations, and the lines indicate predictions for (lighter gray) <i>GAHM(4)</i> , (darker gray) <i>GAHM(8)</i> , and (black) <i>GAHM(12)</i>	33
Figure 2.11	Error statistics for the forecast simulations using NHC advisories 4 through 12. Columns correspond to (left) winds and (right) water levels. Error statistics are shown for (black) <i>RMS</i> and (gray) <i>B_{MN}</i> , with comparisons to (dashed) observations and (solid) <i>HWind</i> hindcast simulation.	34
Figure 2.12	Forecasts of winds (m/s) and water levels (m) during Arthur in coastal North Carolina, but with constant storm size and intensity parameters from <i>HWind</i> . Rows correspond to: (top) <i>GAHM(4,HWind)</i> , (middle) <i>GAHM(8,HWind)</i> , and (bottom) <i>GAHM(12,HWind)</i> . Columns correspond to: (left) maximum wind speeds, and (right) maximum water levels.	35
Figure 2.13	Error statistics for the forecast simulations using NHC advisories 4 through 12 for storm track, but <i>HWind</i> parameters for storm size and intensity. Columns correspond to (left) winds and (right) water levels. Rows show the same information, but for (top) advisory number and (bottom) landfall error (km). Error statistics are shown for (black) <i>RMS</i> and (gray) <i>B_{MN}</i> , with comparisons to (dashed) observations and (solid) <i>HWind</i> hindcast simulation. . .	37
Figure 2.14	Forecasts of winds (m/s) and water levels (m) during Arthur in coastal North Carolina, but with constant track information from <i>HWind</i> . Rows correspond to: (top) <i>GAHM(HWind,4)</i> , (middle) <i>GAHM(HWind,8)</i> , and (bottom) <i>GAHM(HWind,12)</i> . Columns correspond to: (left) maximum wind speeds, and (right) maximum water levels.	39

Figure 2.15	Error statistics for the forecast simulations using NHC advisories 4 through 12 for storm size and intensity, but HWind parameters for storm track. Columns correspond to (left) winds and (right) water levels. Rows show the same information, but for (top) advisory number and (bottom) power dissipation (10^{12} watts). Error statistics are shown for (black) RMS and (gray) B_{MN} , with comparisons to (dashed) observations and (solid) $HWind$ hindcast simulation. .	40
Figure 3.1	Unstructured ADCIRC mesh used in the present study. Top panel shows contours of element spacing. Bottom panel shows the bathymetry and topography contours values in the Choctawhatchee Bay.	45
Figure 3.2	Wind speeds (top panel, in m/s) and directions (bottom panel, in degrees clockwise from North) from November 20, 2013 - December 17, 2013 at Pensacola, FL. Grey circles denote observations at NOAA station (ID: 8729840) and black line denotes model forcing.	52
Figure 3.3	Comparison of observed and modeled water levels. Grey circles denote observations and solid line denotes ADCIRC water levels. .	54
Figure 3.4	Locations in the bay, inlet and shelf waters where vertical salinity (circles) and water level observations (asterisks) are available. . .	56
Figure 3.5	Comparisons of observed (grey circles) and modeled (black asterisks) vertical salinities inside Choctawhatchee Bay (top two panels) and within Destin Inlet (bottom panel).	57
Figure 3.6	Comparisons of observed (grey circles) and modeled (black asterisks) vertical salinities in the shelf waters adjacent to Choctawhatchee Bay.	58
Figure 3.7	Error statistics (from left to right - correlation coefficient, mean bias and centered root mean squared error) computed for model salinities. Top row corresponds to model skill in stratified conditions. Bottom row corresponds to model skill in well mixed conditions. Blue, green and red circles represent “stratified-single”, “double” and “mixed-single” conditions respectively.	61
Figure 3.8	Ebb-phase plume footprint at Destin Inlet observed in SAR satellite imagery and represented by the 33 psu model salinity contour (red line). Wind roses represent the wind forcing over the past 24 hours. (COSMO-SkyMed TM Product ©ASI 2013 processed under license from ASI – Agenzia Spaziale Italiana. All rights reserved. Distributed by e-GEOS. Downlinked and processed by CSTARS.)	63
Figure 3.9	Observed drifter movement (grey lines) and trajectories of Lagrangian particles advected by modeled surface currents (black lines). Drifters are released in the inlet during the ebb-phase on 5 December and 8 December.	65

Figure 3.10	Observed drifter movement (grey lines) and trajectories of Lagrangian particles advected by modeled surface currents (black lines) on 10 December.	66
Figure 4.1	Model plume signature described by the 33 psu salinity contour on 24–27 November overlaid on ArcGIS Map Imagery. Red line shows model plume response to realistic wind forcing. Grey line shows model plume behavior when the wind forcing is disabled.	75
Figure 4.2	Model plume signature described by the 33 psu salinity contour (red line) during a period of neap-to-spring variability in the tides (28 November to 3 December) overlaid on ArcGIS Map Imagery. .	76
Figure 4.3	Model salinities across an east-west transect in the middle of the inlet (viewing from outside the bay). Inset images show the time relative to the tidal cycle.	80
Figure 4.4	Model plume signature described by the 33 psu salinity contour on 24–27 November overlaid on ArcGIS Map Imagery. Red line shows model plume response to realistic wind forcing. Grey line shows model plume behavior when the wind forcing is disabled.	81
Figure 4.5	Model plume signature described by the 31 psu salinity contour (red line) during a period of neap-to-spring variability in the tides (28 November to 3 December) overlaid on ArcGIS Map Imagery. .	82
Figure 4.6	Locations at which monthly salinity measurements are collected by the Choctawhatchee Basin Alliance.	83
Figure 4.7	Observations for monthly surface (blue circles) and bottom salinities (red squares) collected by CBA at six stations inside the bay during 2013 and 2014. Black line represents the river discharge measured (in m^3/s) at the USGS gage located in Bruce, Florida for the same period.	85
Figure 4.8	Top panel shows surface salinities inside the bay. Black line represents model salinities along the bay axis. Circles correspond to observed salinities at 6 stations inside the bay. Circles are colored according to their time-stamp. Bottom panel shows how bathymetry changes from west to east in the bay.	87
Figure 4.9	Model salinity contours at the six CBA stations inside the bay during November-December 2013.	88
Figure 4.10	Path traced by Lagrangian particles advected by ADCIRC surface currents. Red circles denote particle position. Contours represent magnitude of surface currents predicted by the model.	90

Figure 5.1 Representation of Choctawhatchee River in the ADCIRC mesh. Top panel shows the ‘synthetic’ channel and bottom panel shows the ‘realistic’ channel. Inset images zoom to the east end of the bay where the river enters the bay. 99

Chapter 1

Introduction

Estuaries are unique coastline features where freshwater from land drainage mixes with the saline waters of the open ocean. Estuaries also act as buffer zones between the land and the ocean and reduce the impact of storm surge and flooding. Due to their unique locations and physiographic features, estuaries also contain many different types of plant and animal habitats, such as shallow open waters, swamps, sandy beaches, mudflats and sand flats, rocky shores, oyster reefs, mangrove forests, river deltas, tidal pools, seagrass beds, etc., thereby forming a diverse and vibrant ecosystem. Estuaries act as feeding, spawning and nesting grounds for many coastal species and are known as ‘nurseries of the sea.’ Estuaries are also an important economic resource and generate significant revenue for the adjacent coastal communities through activities such as recreational and commercial fishing, boating, tourism etc. Biological processes within estuarine ecosystems are significantly influenced by hydrodynamic processes within an estuary, which are primarily driven by the bay geometry, tidal action, wind effects and freshwater inflows. Therefore, it is critical for estuarine resource management to have a knowledge of the key features of estuarine circulation and have the ability to predict estuarine response to changing winds, tides and freshwater inflows.

The present study examines several aspects of the wind- and plume-driven hydrodynamics and transport near estuarine systems using barotropic and baroclinic models. The study begins with an application of the state-of-the-art in storm surge modeling, in which wind and surge impacts in the estuaries and sounds of North Carolina coastline during Hurricane Arthur are analyzed. In the later chapters, the features of wind and plume driven circulation in the vicinity of Choctawhatchee Bay and Destin Inlet, Florida,

is discussed. Through these analyses, we will explore questions about wind effects on the ebb-phase plume and surface transport at Destin and the salinity gradients and estuarine timescales associated with Choctawhatchee Bay. An overview of each of the individual chapters of this report is provided below.

Hurricane Arthur (2014) was a Category 2 storm that made landfall along the North Carolina (NC) coast during early July 2014. The sensitivity of forecast guidance during Arthur to errors in the storm parameters issued by the National Hurricane Center (NHC) is investigated in Chapter 2. The impacts of Arthur are best represented by the storm surge forecast model (ADCIRC+SWAN) with winds from *HWind*, a data-assimilated, post-storm wind product. However, winds from *GAHM*, a parametric vortex model that is based on wind input from the NHC Best Track provide a reasonable approximation of Arthur's effects and is applied in the current study to reproduce forecast predictions during Arthur. As Arthur moved over Pamlico Sound, it created storm surges up to 2.5 m, which pushed first into the river estuaries and against the inner banks, and then moved eastward to threaten the sound-side of the barrier islands. Forecast advisories from the NHC differed in their track and intensity predictions. Their track predictions improved over time but successive advisories predicted the storm to become too powerful. This caused the forecast of the wind speeds and water levels to get worse (or deviate more from post-storm determined results) as Arthur approached landfall. It is hypothesized that a combination of track and intensity (quantified by a storm's power dissipation) errors caused forecast errors in the winds and water levels along the NC coast during Arthur. Model results reveal that, as the forecast storm track and intensity errors increase, the errors in forecast wind speeds also increase, but the errors in forecast water levels remain relatively the same signifying the non-linear response of the coastal ocean to wind effects.

As hurricane winds push storm surge into estuaries, they can cause a short-term and dramatic increase in estuarine salinities. Storms are also associated with heavy precipitation, which can cause an increase in freshwater runoff into estuarine systems. Future anthropogenic climate change also has the potential to alter estuarine water quality beyond their natural range of variation through changes in land drainage, increased air and water temperatures, and sea level rise (SLR), etc. These changes can significantly alter the habitats of estuarine plant and animal species, who often have distinct tolerance ranges for salinities, temperatures and velocities throughout or during parts of their life cycle. Therefore, for effective decision making for managing estuarine fisheries, plant and

animal habitats, it is important to have the capability to predict changes in estuarine water chemistry. Numerical models that have the ability to model changes in estuarine salinities and temperatures under changing environmental conditions are important tools for this purpose. Such models have an additional level of complexity in comparison to depth-integrated, barotropic tide models such as the one described previously, due to additional physics (baroclinicity) and computational requirements (due to vertical resolution).

In this thesis, a three-dimensional, fully baroclinic ADCIRC model is applied with recent improvements to predict wind-, tide- and density-driven circulation within the Choctawhatchee Bay and adjacent continental shelf. While two-dimensional, depth-integrated ADCIRC is widely used for storm surge applications, its three-dimensional baroclinic version has only undergone limited testing. This study marks the first time a recently-enhanced, three-dimensional, fully baroclinic ADCIRC is applied to model the mixing and transport of freshwater within an estuary.

Choctawhatchee Bay, the third largest estuary in Florida, is a shallow back barrier estuary aligned in an east-west direction along the Florida Panhandle. It receives freshwater predominantly from the Choctawhatchee River, which enters the bay at the east end and connects to the Gulf of Mexico via Destin Tidal Inlet. The bay supports a rich and diverse ecosystem and provides great economic benefit to the adjacent coastal communities through fisheries, navigation and recreational activities. However, the last comprehensive studies of the bay dates back to the 1980s and only limited information exists about key features of the circulation inside Choctawhatchee Bay, such as trends in salinity gradients, stratification and residence times.

The inner shelf in the vicinity of Destin Inlet, where oil washed ashore during the Deepwater Horizon Oil spill in June 2010, was the site of a series of experiments conducted by CARTHE (Consortium for Advanced Research on Transport of Hydrocarbon in the Environment) scientists during December 3–17, 2013. The aim of these experiments, collectively referred to as SCOPE (Surfzone Coastal Oil Pathways Experiment), was to identify circulation features that influence the near-shore transport of oil. SCOPE measurements documented the presence of a brackish estuarine outflow from Choctawhatchee Bay during the ebb-phase of the tidal cycle. Nearshore current measurements and drifter pathways revealed the wind- and plume-driven nature of the circulation offshore of Destin. These observations showed that as wind conditions changed the plume response

varied. However, due to limitations associated with a field experiment, the plume behavior was documented only on selected days in December. Variability in the surface plume geometry on consecutive days of variable wind and tidal forcing is unknown.

What is the length and width of the ebb-phase plume that exits out of Destin Inlet? Does the plume geometry exhibit substantial changes as passing cold fronts bring about changes in wind direction in consecutive days? What are the magnitudes of these changes? What is the plume response if the wind forcing is disabled? What are the trends in salinity gradients within the bay? What is the degree of stratification within the bay? Does the stratification change considerably due to changes in tidal and wind forcing during the study period? What are estimates of the residence times within the Choctawhatchee Bay? By answering these questions, this research work aims to address the gaps in our scientific understanding of salinity transport in the vicinity of Destin Inlet and within Choctawhatchee Bay.

To answer the above questions, we adopt a numerical modeling approach. A three-dimensional, baroclinic, unstructured, shelf-scale ADCIRC model is developed for Choctawhatchee Bay. Different aspects of model development and set-up including governing equations, mesh development, initial and boundary conditions, physical forcings and bathymetry smoothing are described in Chapter 3. Model predictions for water levels, vertical salinities, surface currents and the ebb-phase plume signatures are validated using in-situ observations, observed drifter movements and satellite imagery. Overall, the model is able to capture key features of the salinity transport and circulation in the vicinity of Choctawhatchee Bay.

The validated model is then applied in Chapter 4 to investigate those research questions. In the Northern Gulf of Mexico, extra-tropical storms or cold air outbreaks are common during winter. These storms last for 3–8 days and are accompanied by 360 degree reversals in wind direction. It is hypothesized that changing wind conditions during the passing of a cold front and neap-spring variability in tides will influence the geometry of the ebb-phase surface plume at Destin. Model salinities prove this hypothesis and are used to quantify the degree of plume variability in two scenarios. In the first scenario, plume behavior during a period of near-constant tides and changing wind conditions is quantified. In the second scenario, plume behavior during a period of near-constant winds and neap to spring variability in tides is analyzed.

Based on limited studies in the past, it is hypothesized that unique zones exist within

the bay that have distinct surface salinity gradients. It is also hypothesized that the bay is highly stratified. Model predictions reveal that during periods of low river flows surface salinities are brackish and are roughly of the same magnitude throughout most of the bay except near the river. Model salinities also indicate a large gradient in vertical salinities throughout most of the bay and show the highly stratified condition of the bay. Finally, the validated model is also applied to analyze other aspects of estuarine salinity transport including variability in the surface signature of the flood-phase salt plume, inlet salinities over a tidal cycle and residence time within the bay.

Research findings provide important insights about wind- and plume-driven circulation in estuaries through predictive modeling. Forecast systems based on depth integrated, barotropic models are useful for real-time predictions of storm surge in estuarine systems. This study presents a novel analysis that demonstrates the potential for errors in the forecast storm's track and intensity and therefore, shows the need to account for both while running forecast systems. As mentioned earlier, one of the defining characteristics of estuaries is the mixing and transport of freshwater. This work demonstrates the successful application of a three dimensional baroclinic model to predict salinity characteristics in a relatively less-known shelf-estuarine system. Model predictions quantify the wind-driven behavior of the ebb-phase plume, which influences surface transport in the nearshore. Modeled estuarine salinities and stratification indicate the range of salinities within the bay and its degree of variability, which has implications for the survival of estuarine habitats. Thus, research insights contribute to our scientific understanding of salinity transport within shelf-estuarine environments, and are therefore, useful for effective decision making for estuarine resource management.

Chapter 2

Variability in Coastal Flooding Predictions due to Forecast Errors during Hurricane Arthur

2.1 Overview

In this chapter, the sensitivity of surge predictions to forecast uncertainties in the track and strength of a storm are analyzed in the context of Hurricane Arthur (2014). First, hindcast simulations of a coupled hydrodynamic-wave model are performed on a large unstructured mesh to analyze the surge impact of Arthur along the North Carolina coastline. Then, surge predictions driven by forecast advisories issued by the National Hurricane Center (NHC) during Arthur are analyzed to evaluate the performance of the forecast system. Finally, the sensitivity of forecast wind speeds and water levels during Arthur to errors in forecast storm parameters such as storm track and intensity are separately analyzed. This chapter has been published in *Coastal Engineering* as Cyriac et al. (2018).

2.2 Introduction

The coastal communities of North Carolina (NC) are under the constant risk of hurricanes. The State Climate Office of NC estimates that a tropical cyclone makes landfall in NC every 2.5 years (State Climate Office of North Carolina, 2017), and the network of

bays, estuaries, sounds and barrier islands that define the NC coastline further increases the vulnerability of its coastal regions to the impacts of storm surge and flooding. Surge levels have ranged from 2 m during recent hurricanes like Isabel (2003) and Irene (2011), to 3 m during Floyd (1999) and to more than 6 m during Hazel (1954). The strong winds, storm surge and rainfall associated with these hurricanes, each differing in track and intensity, have caused damages worth billions of dollars (Barnes, 2013).

Technological advancements in flood forecasting have enabled emergency managers to be better informed about the behavior of a threatening storm and its potential impact on their coastal communities. To provide accurate predictions, flood forecasting systems rely on estimations of the storm parameters (e.g., track, size and intensity), accurate representation of coastal geometry, accurate simulations of meteorological and coastal ocean conditions by numerical models, and communication of forecast guidance to policymakers and emergency managers in the coastal counties. Emergency managers use these predictions to prepare coastal communities by issuing appropriate warnings, planning evacuation strategies, managing emergency shelters and estimating potential damage to infrastructure during the hurricane (Cheung et al., 2003).

The ADvanced CIRCulation (ADCIRC) model is an unstructured-mesh, finite-element, hydrodynamic model used to simulate storm surge, tides and riverine flow that has been applied extensively for retrospective and risk based storm surge predictions and validation (Westerink et al., 2008; Bunya et al., 2010; Dietrich et al., 2010; Dietrich et al., 2011a; Blanton et al., 2012b; Lin et al., 2012; Atkinson et al., 2013; Bhaskaran et al., 2013; Murty et al., 2014; Lin et al., 2016). ADCIRC comprises the core of the ADCIRC Surge Guidance System (ASGS) that has been deployed to forecast storm surge along the US East and Gulf of Mexico coasts (Fleming et al., 2008; Dresback et al., 2013; Dietrich et al., 2013b). For storm surge simulations, ADCIRC is implemented typically to have basin scale coverage with finest resolution of about 20 m in specific areas of interest. The resulting mesh may have millions of finite elements and thus require substantial computing resources to solve. For example, during Hurricane Arthur (2014), a 5-day ASGS forecast on 480 processor cores took 34 minutes on an unstructured mesh with 295328 vertices. Individual ADCIRC simulations have higher fidelity than limited-domain, low-resolution simulations (Kerr et al., 2013), because of the larger computational domain and the higher resolution of coastal features that may influence surge propagation along and across the coast. As a result, predictions from ADCIRC

simulations may be more sensitive to storm characteristics, especially the storm surge response near fine-scale topographic features.

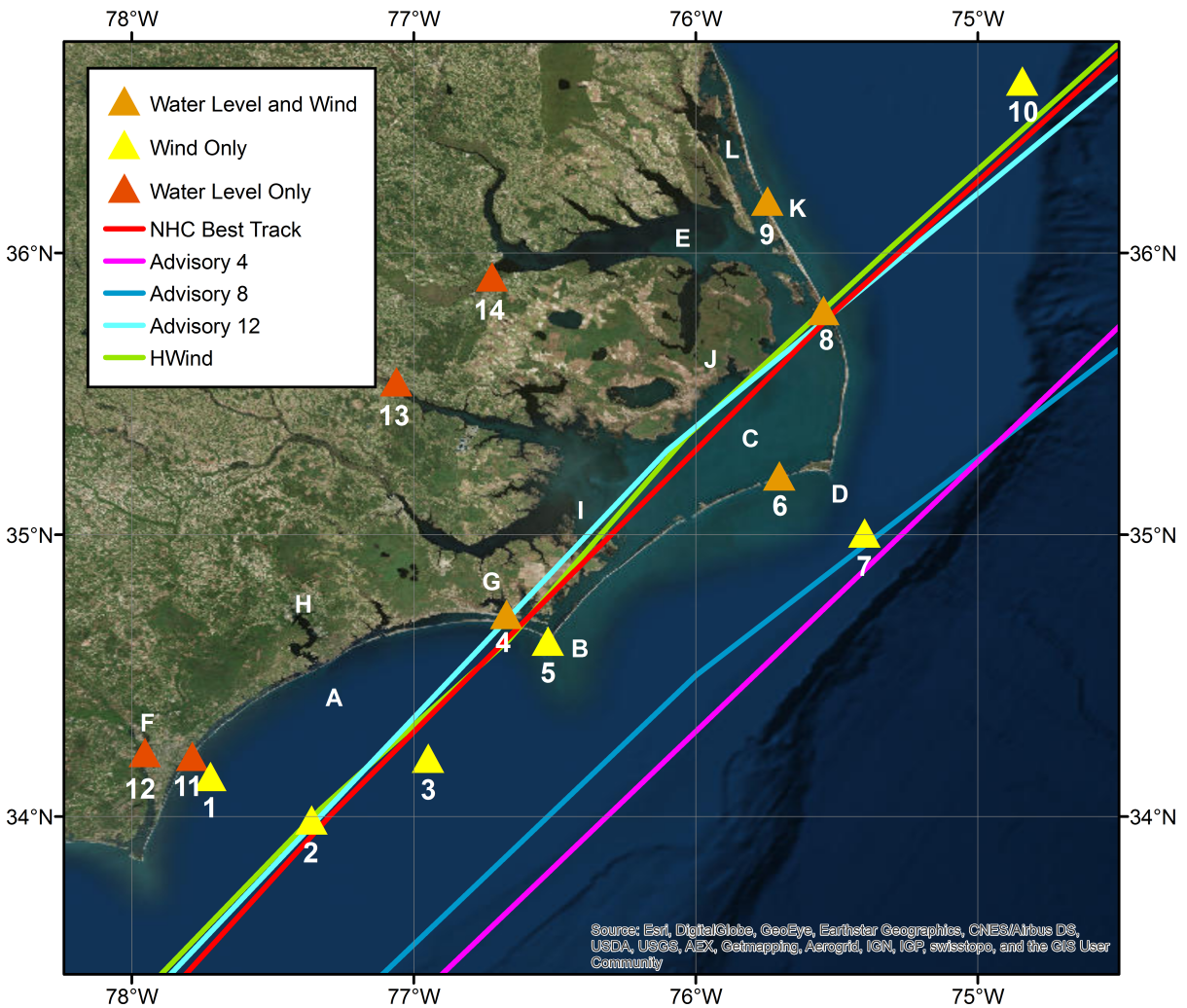


Figure 2.1 Observation stations used for model validations (indicated by numbers) and other important geographic locations along the NC coast that are referenced in the paper (indicated by alphabets). Please refer to Table 2.2 for detailed description. Lines indicate storm track predictions during advisories 4 (pink), 8 (blue) and 12 (cyan) issued by the NHC 54, 30 and 12 hr before Arthur made landfall along the NC coast. The best track (red line) issued after the storm by the NHC and the storm track represented by HWind (light green) is also shown.

The ASGS was employed during Hurricane Arthur (2014), a Category 2 storm that impacted the North Carolina (NC) coastal region during early July 2014 (Berg, 2015). As

Table 2.1 Summary of selected locations along the North Carolina coast referenced in the text.

Code	Location
A	Onslow Bay
B	Cape Lookout
C	Pamlico Sound
D	Cape Hatteras
E	Albemarle Sound
F	Wilmington
G	Beaufort
H	Jacksonville
I	Cedar Island
J	Hyde County
K	Kitty Hawk Island

the storm moved over Pamlico Sound (Figure 2.1), it created storm surges up to 2.5 m, which pushed first into the river estuaries and against the inner banks, and then moved eastward to threaten the sound-side of the barrier islands. Early forecast advisories from the National Hurricane Center (NHC) predicted the storm to remain offshore. These forecast advisories also differed in their predictions of the storm’s intensity. These track errors were not large in an absolute sense (about 130 km, which is less than the annual average track error for NHC predictions for the period 2010-2016 (National Hurricane Center, 2017)), but we hypothesize that their effects on flooding predictions were significant due to the nonlinear interactions of winds, waves and storm surge within the NC coastal system.

Recent studies have examined the sensitivity of storm surge predictions to errors in forecast storm parameters. Site- and time-specific forecast uncertainties in storm parameters (storm intensity, size, forward speed and track angle) were estimated from archived historical storm data and applied to develop probabilistic surge estimates for synthetic storms at point locations inside New Orleans (Resio et al., 2017). For idealized storms over coastal NC, it was found that storm surge and inundation are sensitive to the forward speed, size, and track angle relative to the coast (Peng et al., 2004; Peng et al., 2006).

For Isabel (2003) in Chesapeake Bay, it was found that the storm surge magnitude and timing were sensitive to errors in the storm track, intensity, and forward speed, although the response varied spatially (Zhong et al., 2010). However, the above de-

terministic studies used hypothetical perturbations from either idealized storms or the best-track information, i.e., the storm track was shifted by 100 km, or the wind speed was increased or decreased by 50 percent. They did not consider the real uncertainties in storm information during the forecasts before landfall. For Isaac (2012) in Louisiana, the forecast performance of ADCIRC was evaluated for different sources of atmospheric forcing (Dietrich et al., 2018), but the relative effects of storm parameters were not considered.

Table 2.2 Summary of station locations at which measurements of wind speeds and water levels are available for the study period.

Number	Longitude	Latitude	Station ID	Agency	Winds	Water Levels
1	-77.721	34.142	41038	CORMP	X	
2	-77.363	33.988	41037	CORMP	X	
3	-76.949	34.207	41036	NDBC	X	
4	-76.667	34.716	BFTN7/8656483	NOAA/NOS	X	X
5	-76.525	34.622	CLKN7	NOAA/NOS	X	
6	-75.704	35.209	HCGN7/8654467	NOAA/NOS	X	X
7	-75.402	35.006	41025	NDBC	X	
8	-75.548	35.796	ORIN7/8652587	NOAA/NOS	X	X
9	-75.746	36.184	DUKN7/8651370	NOAA/NOS	X	X
10	-74.842	36.61	44014	USACE	X	
11	-77.786	34.213	8658163	NOAA/NOS		X
12	-77.9533	34.2267	8658120	NOAA/NOS		X
13	-77.062	35.543	2084472	USGS		X
14	-76.723	35.915	208114150	USGS		X

In this study, we analyze the performance of ADCIRC during Arthur, especially with respect to errors in the storm track forecasts from the NHC. Arthur provides a suitable opportunity for this analysis, because track forecasts evolved from a scenario without landfall (and minimal impact to coastal regions) to a scenario with the storm moving directly over Pamlico Sound, creating significant storm surge and flooding. The earlier forecast advisories from the NHC (e.g., advisory 4 issued 54 hours before landfall) estimated that Arthur would follow an eastward track without making landfall along the NC

coast, but these predictions changed progressively in advisories issued closer to landfall (Figure 2.1). Advisory 12 (issued 6 hours before landfall) was a close representation of the storm’s true track over Pamlico Sound. However, even as the projected storm track was improving, the forecasts were projecting the storm to grow too powerful. Through comparisons with observed water levels during the storm, and with simulations forced by the best-track, post-storm guidance issued by the NHC, it is shown that the later surge predictions were a progressively-worse representation of the storm’s impact on the surge environment in coastal NC. By isolating the effects of errors in storm track and storm strength, we will quantify the relative importance of these parameters in predicting peak wind speeds and storm surge. This knowledge will benefit real-time storm surge forecast systems to suitably incorporate the effects of errors in storm track and intensity while providing flooding predictions. Geospatial visualizations for this study were produced using a new visualization tool called Kalpana, which is described in more detail in Appendix A.

2.3 Hurricane Arthur (2014)

2.3.1 Synoptic History

Hurricane Arthur was the first named storm of the 2014 Atlantic hurricane season. It formed off the southeastern coast of United States and was classified as a tropical depression on 2014/07/01/0300 UTC (Berg, 2015), when the NHC issued its first forecast advisory. At 2014/07/01/1200 UTC, the depression developed into a tropical storm located about 111 km east of Ft. Pierce, FL. During the next three days, the storm moved northward and strengthened into a hurricane by 2014/07/03/0000 UTC, as it moved offshore of Savannah, GA. Arthur made landfall along the NC coast near Shackleford Banks at 2014/07/04/0315 UTC as a Category 2 hurricane on the Saffir-Simpson scale. The storm moved northeastward over Pamlico Sound, moved over the northern Outer Banks at 2014/07/04/0800 UTC, and then continued into the northern Atlantic Ocean (Berg, 2015).

The NHC forecasts changed significantly during the two days before Arthur’s initial landfall in NC. For most of the forecast advisories, the storm was projected to remain offshore, with a track that moved northeastward off the Outer Banks. The forecast

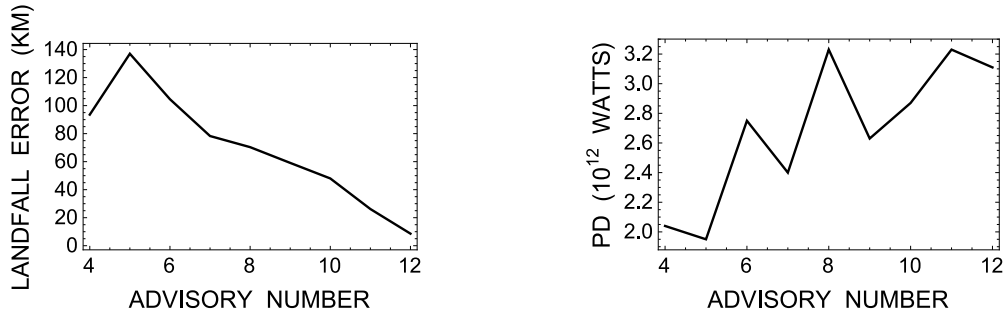


Figure 2.2 Evolution by forecast advisory number of Arthur’s (left) forecast landfall error (km) at 2014/07/04/0300 UTC, and (right) power dissipation (10^{12} watts) averaged over 24 hr surrounding its initial landfall.

track shifted westward, and by advisory 10, the storm was projected to move over Cape Hatteras. By advisory 12, the projected landfall location was very close to the storm’s initial landfall near Shackleford Banks, NC. This improvement in track forecast accuracy can be quantified via the error in storm center position (Figure 2.2, left). These errors are computed as distances relative to the storm center in a data-assimilated wind product, which is described below, at 2014/07/04/0300 UTC, as the storm was making its initial landfall. For advisory 5, the storm center was in error by 137 km; by advisory 12, the storm center had corrected to within 9 km of the correct landfall location. Thus, the forecast track accuracy improved by about 3 km/hr (or 18 km per advisory) as Arthur approached NC.

During that same time, the storm was projected to increase in size and intensity. The storm’s strength can be represented by the power dissipation (PD , (Emanuel, 2005)):

$$PD = \int_A C_D \rho |\mathbf{V}|^3 dA$$

in which C_D is the drag coefficient, ρ is the surface air density, $|\mathbf{V}|$ is the magnitude of the surface wind velocity, and the integral is evaluated over the surface area A of the storm. PD has units of energy per time, or power, with units of watts. Herein, we assume the linear drag coefficient relationship from (Garratt, 1977) with a maximum value of $C_D = 0.0035$, and assume a surface air density of 1 kg/m^3 . For each of the atmospheric products described below, the integral will be computed over the entire computational domain, including any land masking used by the wave and circulation models; thus, the

PD can be seen as a measure of the available power to the wave and circulation models. For the NHC forecast advisories, the PD increased generally as Arthur approached NC, from a value for advisory 4 of $2.04 \cdot 10^{12}$ watts, to a value for advisory 12 of $3.11 \cdot 10^{12}$ watts. Thus, as the forecast track was improving, the projected storm strength was increasing by more than 50 percent.

2.3.2 Observations

Arthur's effects in the coastal environment were captured by observations at: offshore buoys operated by the National Data Buoy Center (NDBC), Coastal Ocean Research and Monitoring Program (CORMP), and US Army Corps of Engineers; tide gauges operated by the National Ocean Service (NOS); and river gauges operated by the U.S. Geological Survey (USGS). These stations (described in Figure 2.1 and Table 2.2) provide a valuable description of the evolution of wind speeds and surge levels as Arthur moved through coastal NC. Wind speeds measured at the NDBC offshore buoys and land stations are processed to match the 10-min averaging period of ADCIRC wind speeds. The averaging periods for the measurement data are 8-min for buoys (41036, 41037 and 41025) and 2-min for land stations (BFTN7, HCGN7, ORIN7, DUKN7 and CLKN7). Using site-specific inputs such as terrain roughness and Coriolis parameter, the measurement data are referenced to 1-hr mean wind speeds, and then gust factors are computed for the conversion to 10-min wind speeds ((Vickery et al., 2005)). Based on an analysis at station ORIN7, a factor of 1.076 is used to convert the observations to 10-min wind speeds at all the land stations. A similar analysis yielded a conversion factor of 1.005 for observations at the NDBC buoys (41037 and 41025).

2.4 Methods

2.4.1 Models for Storm-Induced Waves and Surge

The hydrodynamic model ADCIRC (adcirc.org) solves modified forms of the shallow water equations. It uses the Generalized Wave Continuity Equation (GWCE) for water levels and either the three-dimensional or the vertically integrated momentum equations for currents U and V ((Luettich et al., 2004; Dietrich et al., 2012a; Dawson et al., 2006; Murty et al., 2014; Bhaskaran et al., 2013)). The evolution of waves is simulated using

SWAN (Simulating WAves Nearshore), a phase-averaged wave model that describes the evolution of action density $N(t, \lambda, \phi, \theta, \sigma)$ in time (t), geographic space (with longitudes λ and latitudes ϕ) and spectral space (with directions θ and frequencies σ). During tightly coupled ADCIRC+SWAN simulations, wind speeds, water level, current velocities and roughness lengths provided by ADCIRC are used by SWAN to calculate the radiation stress gradients responsible for the wave-induced setup that contributes to water levels ((Dietrich et al., 2011b; Dietrich et al., 2012a; Hope et al., 2013)). For the present study, ADCIRC simulations are performed with a time step of 0.5 seconds, while the SWAN time step and coupling interval are 1200 seconds. Spatially-variable settings are used for the weighting factor (τ_0) in GWCE (0.005 in open water, 0.03 inland), eddy viscosity ($2m^2/s$ in open water, and $10 m^2/s$ inland), and Mannings n (default value of 0.02 in open water, with larger inland values based on land-cover).

2.4.2 Atmospheric Forcing

We utilize two sources of atmospheric forcing: an analysis product based on observations, and a parametric vortex model based on storm parameters from the NHC guidance.

2.4.2.1 Real-Time Hurricane Wind Analysis System (HWind)

Spatially- and temporally-varying wind fields can be constructed from observations of wind velocities during a storm. The Real-Time Hurricane Wind Analysis System (HWind) was developed as part of the NOAA Hurricane Research Division (Powell et al., 1998). Observations of wind velocity relative to the storm center are incorporated by HWind, which converts them to a common reference frame at 10-m height, peak 1-min-averaged sustained wind speed, and marine exposure. Wind velocities from airborne stepped-frequency microwave radiometers, GPS dropsondes, buoys, ships, satellite-based visual imagery, and land-based platforms (DiNapoli et al., 2012) are then smoothed and interpolated onto a regular grid by minimizing the least-square differences between observations and analysis (Powell et al., 1996). Starting with the 2013 hurricane season, these wind fields have been produced by Risk Management Solutions, Inc. (RMS, <http://www.rms.com/perils/hwind/>). These wind fields are developed with observations during the storm, and thus can be used only for hindcasting.

The HWind fields for Arthur are available for 3.625 days from 1800 UTC on 1 July 2014 through 0900 UTC on 5 July 2014. The gridded HWind field is interpolated spa-

tially onto ADCIRC mesh vertices at every available snap of HWind data, and then interpolated temporally to derive the wind field for intermediate time steps. The storm vortex structure is preserved by utilizing HWind data snaps that are spaced closely in time (every three hours during the peak of the storm). The wind speeds are converted from a 1-minute sustained wind speed to a 10-minute wind speed for use by ADCIRC, by using a multiplier of 0.893 (Powell et al., 1996). The HWind fields do not include surface pressures, so central pressures from the NHC Best-Track guidance were used to generate pressure fields in space and time. This method uses the Holland vortex model (Holland, 1980) to compute barometric pressure with distance from the storm center.

2.4.2.2 Generalized Asymmetric Holland Model (GAHM)

When ADCIRC is used for real-time storm surge forecasting during tropical cyclones, it constructs pressure and wind fields within its computational domain by using a parametric vortex model based on (Holland, 1980). Axisymmetric pressure and wind fields can be computed from a limited set of parameters such as the storm’s eye location, central pressure, radius to maximum winds (RMW), and maximum sustained wind speed, all of which are available in the advisories issued by the NHC. This model has been modified to reflect storm asymmetry with an azimuthally-varying RMW, by using the distance to the highest-specified isotach in each of the storm quadrants (Xie et al., 2006). This parametric vortex model, which do not include the background wind field, has been used as atmospheric forcing to generate storm surge predictions for previous storms (Mattocks et al., 2006; Mattocks et al., 2008; Forbes et al., 2010; Dietrich et al., 2013a).

In this study, we utilize a newer version of the parametric vortex model that removes the assumption of cyclostrophic balance at the location of the maximum wind speed around the storm and also allows the use of multiple isotachs in each wind quadrant to better specify the storm wind field. The cyclostrophic assumption (i.e., neglecting the Coriolis force) at RMW is valid for strong and compact TCs, but it introduces errors for generally weak or large TCs, or TCs at their developing or dissipating stages. The Generalized Asymmetric Holland Model (GAHM) has been developed to avoid these assumptions. The assumption of cyclostrophic balance is eliminated, and multiple isotachs are used to construct the wind field, thus ensuring that modeled winds match all available information. GAHM has been shown to be a better representation of the storm, via comparisons of model results for past hurricanes with the corresponding best-track guidance,

e.g., for Hurricane Isaac (2012) in southeastern Louisiana (Dietrich et al., 2018).

GAHM is integrated within the ADCIRC source code and uses information from NHC advisories in the Automated Tropical Cyclone Forecast (ATCF) format. It requires parameters about the wind field: maximum sustained wind speed (column 9 in the ATCF format), wind intensities for the identified isotachs (column 12), radii to the isotachs (columns 14-17), and RMW (column 20). It also requires information about the pressure field: minimum sea level pressure (column 10), and background pressure (column 18). The file containing this information is preprocessed to add columns with quadrant-specific values for RMW, maximum wind speed, and the Holland B parameter.

2.4.3 Swapping Information Between HWind and GAHM

The studies below consider scenarios in which these two atmospheric forcings are mixed, i.e., storm parameters from the HWind analysis are applied in GAHM. The reasoning for this mixture of storm parameters is discussed in the sections below; for now, we describe how we move storm information between the two forcings.

To examine the affects of errors associated with storm track, one set of scenarios replaces the storm strength parameters from the NHC forecast guidance with the same parameters derived from post storm analysis. For the wind field, the isotach values are replaced with wind speeds and radii interpolated from isotachs in the gridded HWind fields. For example, to find the radii to the 34-knot isotach, we move outward in the HWind field in each quadrant until we find the grid cell containing the isotach, and then use a linear interpolation to find its distance from the storm center. For the pressure field, the values are replaced with information from the NHC best-track guidance, because the HWind analysis does not provide information about the pressure fields. Values are replaced in the appropriate columns in the ATCF-formatted files for use with GAHM. In this way, the storm intensity and size are unchanged, but the storm track varies with each advisory.

To examine the effects of errors associated with storm strength, another set of scenarios replaces the track in the NHC forecast guidance with the track extracted from the HWind analysis. The storm center positions are identified in the HWind gridded files, and then used to adjust the values used with GAHM. For example, to adjust the track for the wind- and pressure-fields corresponding to 2014/07/02/0000 UTC, we find the storm center position from the HWind gridded file for that date and time, and then use

it to replace the position in the corresponding entry in the ATCF-formatted file. This process is repeated for the other dates and times during the simulation. In this way, the storm track is unchanged, but the storm strength parameters (that determine the wind- and pressure-fields) vary with each advisory.

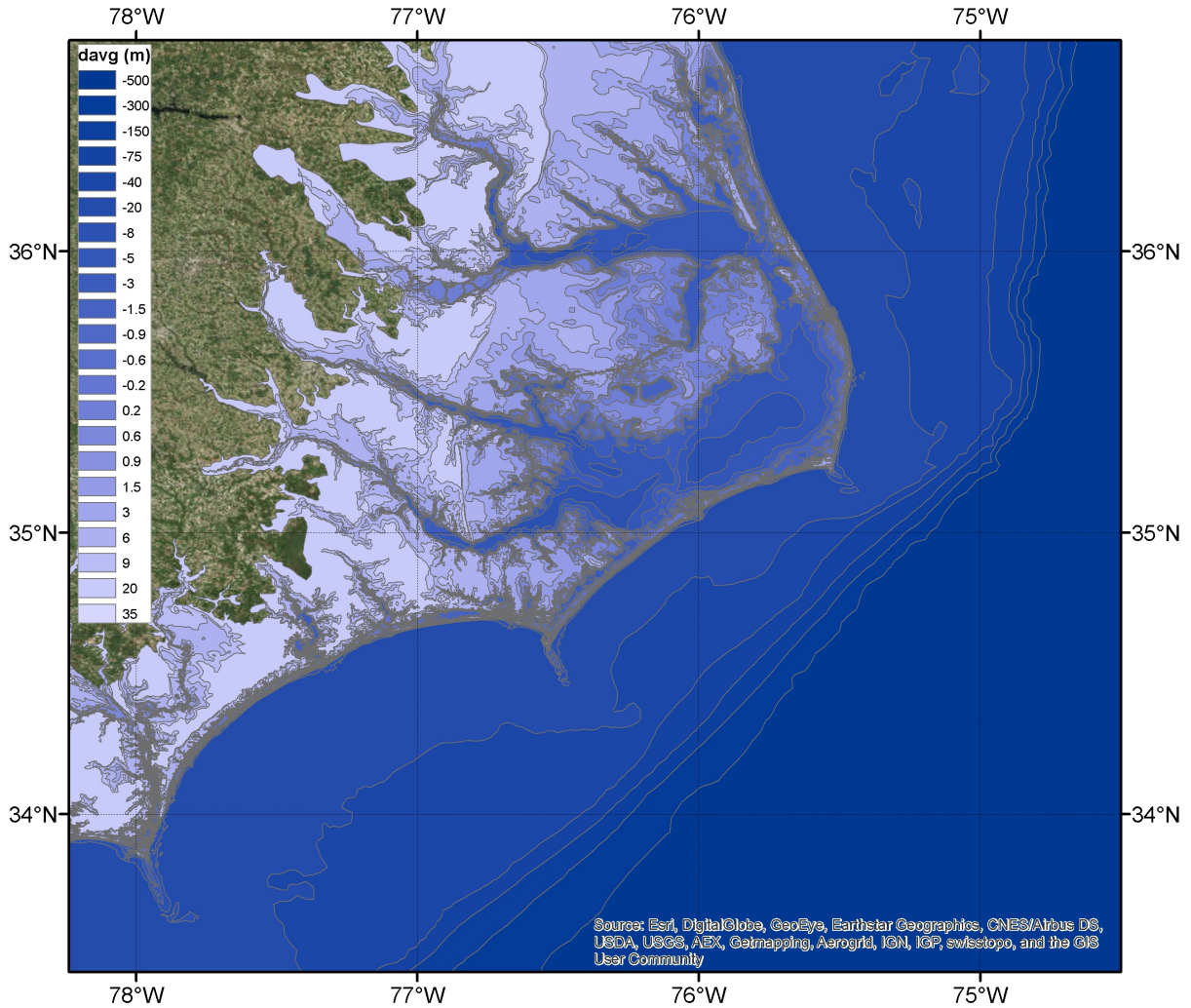


Figure 2.3 Bathymetry and topography contours (m, relative to mean sea level) for the NC9 mesh used by the ASGS for generating storm surge forecasts during Hurricane Arthur (2014).

2.4.4 Unstructured Mesh Describing Coastal NC

The unstructured, finite-element mesh used in the present study is NC v9.98 (referred to as the NC9 mesh throughout this study), which covers the entire Western North Atlantic, the Gulf of Mexico and the Caribbean Sea. Such a large domain for ADCIRC helps to minimize errors associated with open ocean boundary conditions and to track hurricane movement throughout the domain ((Dresback et al., 2013)). The mesh extends inland along the NC coast to the 15-m topographic contour to allow for storm surge flooding (Figure 2.3). In this region, the mesh has been designed to resolve bathymetric and topographic features such as inlets, dunes and rivers as identifiable on satellite images, NOAA charts, shoreline datasets and high-resolution DEMs with data from multiple sources ((Blanton et al., 2008b)). This mesh includes sufficient resolution to represent realistically the numerous inlets through the NC barrier islands, the back bays and sounds, and the Atlantic Intracoastal Waterway that runs north-south through the NC sounds (Blanton et al., 2008a),(Blanton et al., 2012a)). There are a total of 622,946 computational vertices and 1,230,430 elements in the NC mesh; more than 90 percent of this resolution is applied within coastal NC. Large elements with a mesh spacing of 50 to 100 km describe the Gulf of Mexico and open Atlantic, and the elements decrease in size as the bathymetry transitions to near-shore conditions. Mesh spacing along the NC coastline varies from 3 to 4 km on the continental shelf to about 100 m near the Outer Banks. Resolution in Pamlico and Albemarle Sounds is 1500 to 1800 m in the deeper regions and, reduces to 100 to 300 m at the entrance of the river channels and in the shallower regions that border the sounds. Resolution of the narrow river channels that extend inland from the sounds and elsewhere along the NC coastline is generally less than 50 m. The topography/bathymetry values have NAVD88 as their vertical datum and NAD83 as the horizontal datum.

Table 2.3 Summary of storm tracks, wind and pressure fields used in each simulation. Each forecast simulation uses information from the corresponding NHC forecast advisory, e.g., $GAHM(4)$ uses parameters from NHC forecast advisory 4 to construct wind and pressure fields using GAHM. For hybrid simulations, the track and storm information comes from different sources, e.g., $GAHM(12,HWind)$ uses the storm track from NHC forecast advisory 12, but with parameters for storm size and intensity from the hindcast $HWind$ simulation.

Type	Simulation	Track	Wind	Pressure
Hindcast	$HWind$	HWind	HWind	NHC BT
	$GAHM(BT)$	NHC BT	NHC BT	NHC BT
	$GAHM(HWind)$	HWind	HWind	NHC BT
Forecast	$GAHM(4-12)$	NHC 4-12	NHC 4-12	NHC 4-12
Track Uncertainty	$GAHM(4-12,HWind)$	NHC 4-12	HWind	NHC BT
Storm Uncertainty	$GAHM(HWind,4-12)$	HWind	NHC 4-12	NHC 4-12

2.5 Results and Discussion

2.5.1 Validation for Atmospheric Products Available Before and After the Storm

2.5.1.1 Hindcasts

To understand the true effects of Arthur on coastal North Carolina, we consider the best-available representations of Arthur from two atmospheric forcings: the $HWind$ analysis product, and GAHM using the Best-Track guidance for storm parameters issued by the NHC. We denote the first simulation as $HWind$, and the second simulation as $GAHM(BT)$. Also, to examine GAHM’s ability to reproduce the wind field described by $HWind$, we consider a third simulation with a hybrid of forcings: GAHM using the track and wind-field parameters from $HWind$, denoted as $GAHM(HWind)$. The sources of tracks, wind- and pressure-fields for all simulations are summarized in Table 2.3.

Winds – The hindcasts represent the observed path of Arthur as it made landfall, passed over Pamlico Sound, and then followed a northeastward track away from the coast. At 2014/07/04/0000 UTC, Arthur was positioned in Onslow Bay and was moving toward the shore with mean wind speeds greater than 35 m/s. The eye was positioned southeast of Wilmington, and the storm had mean wind speeds of 25 – 30 m/s to the south of

Beaufort, NC. (Geographic locations of specific cities, bays, sounds, etc. are summarized in Figure 2.1 and Table 2.1.) Three hours later at 2014/07/04/0300 UTC, Arthur made its first landfall at Shackleford Banks near Beaufort, NC, as a category 2 storm with mean wind speeds between 35 – 40 m/s along the coast from Jacksonville to Cedar Island, NC (Berg, 2015). Further north, the mean wind speeds were larger than 25 m/s over Pamlico Sound behind the barrier islands. The winds were beginning to blow southeasterly over this region because of the storm’s northeastern trajectory.

By 2014/07/04/0600 UTC, Arthur made a second landfall near Hyde County, NC, as the storm moved over Pamlico Sound. This landfall was accompanied by northwesterly winds with mean speeds as large as 37 m/s blowing over Pamlico Sound and adjacent regions. The *HWind* and *GAHM(BT)* simulations are a good match in the storm track and forward speed, and are a decent match for the peak wind speed, but are different in the size of the storm. This behavior can be observed in the predictions as the storm was moving over Pamlico Sound (Figure 2.4, left column). For *HWind*, the peak wind speeds (larger than 30 m/s) are contained within the southeast quadrant of the storm, while for *GAHM(BT)*, these peak winds extend into the southwest and northeast quadrants, thus affecting regions along the track of the storm. In the Neuse and Pamlico River estuaries on the west end of Pamlico Sound, and also within Albemarle Sound to the north, the wind speeds are about 5 m/s larger in *GAHM(BT)* than in *HWind*. These trends are repeated in the maximum wind fields experienced during the storm (Figure 2.4, center and right columns). The *GAHM(BT)* wind speeds are about 10 m/s larger along the storm track, but the difference is smaller to the east of the track, where the peak winds occurred during the storm. Using the NHC best-track storm parameters, *GAHM(BT)* is producing a storm with the correct track and peak intensity, but that is too large.

When GAHM is applied with the storm track and wind information from *HWind*, the *GAHM(HWind)* simulation is a better match to the size of the storm (Figure 2.4, bottom row). The peak wind speeds are contained within the southeast quadrant, although rotated southward relative to *HWind*. The maximum wind speeds are still too large in *GAHM(HWind)* by about 5 – 8 m/s along the storm track, but there is a significant improvement relative to *GAHM(BT)*. Given a similar set of storm parameters, *GAHM(HWind)* matches well to the wind field in the *HWind* analysis product.

The observations reveal similar behavior (Figure 2.5). While *HWind*, whose wind forcing is most realistic due to post storm data assimilation, is generally a good match

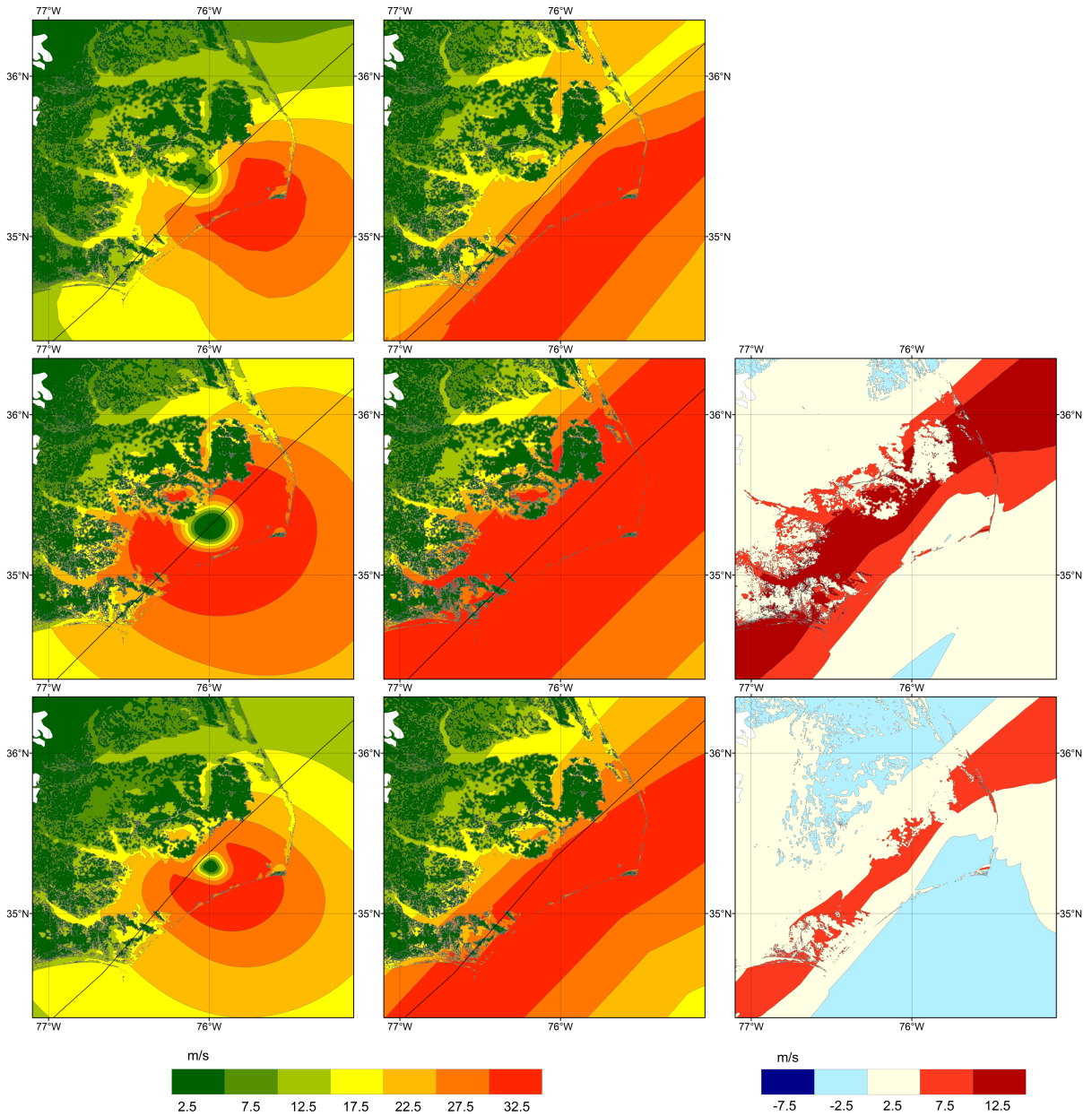


Figure 2.4 Hindcasts of wind speeds (m/s) during Arthur in coastal North Carolina. Rows correspond to: (top) *HWind*, (middle) *GAHM(BT)*, and (bottom) *GAHM(HWind)*. Columns correspond to: (left) wind speeds at 2014/07/04/0600 UTC, (center) maximum wind speeds, and (right) difference in maximum wind speeds relative to *HWind*.

to the observations, including at the storm peak, *GAHM(BT)* has wind speeds that are generally too large by 5 – 10 m/s, including both before and at the storm peak. At

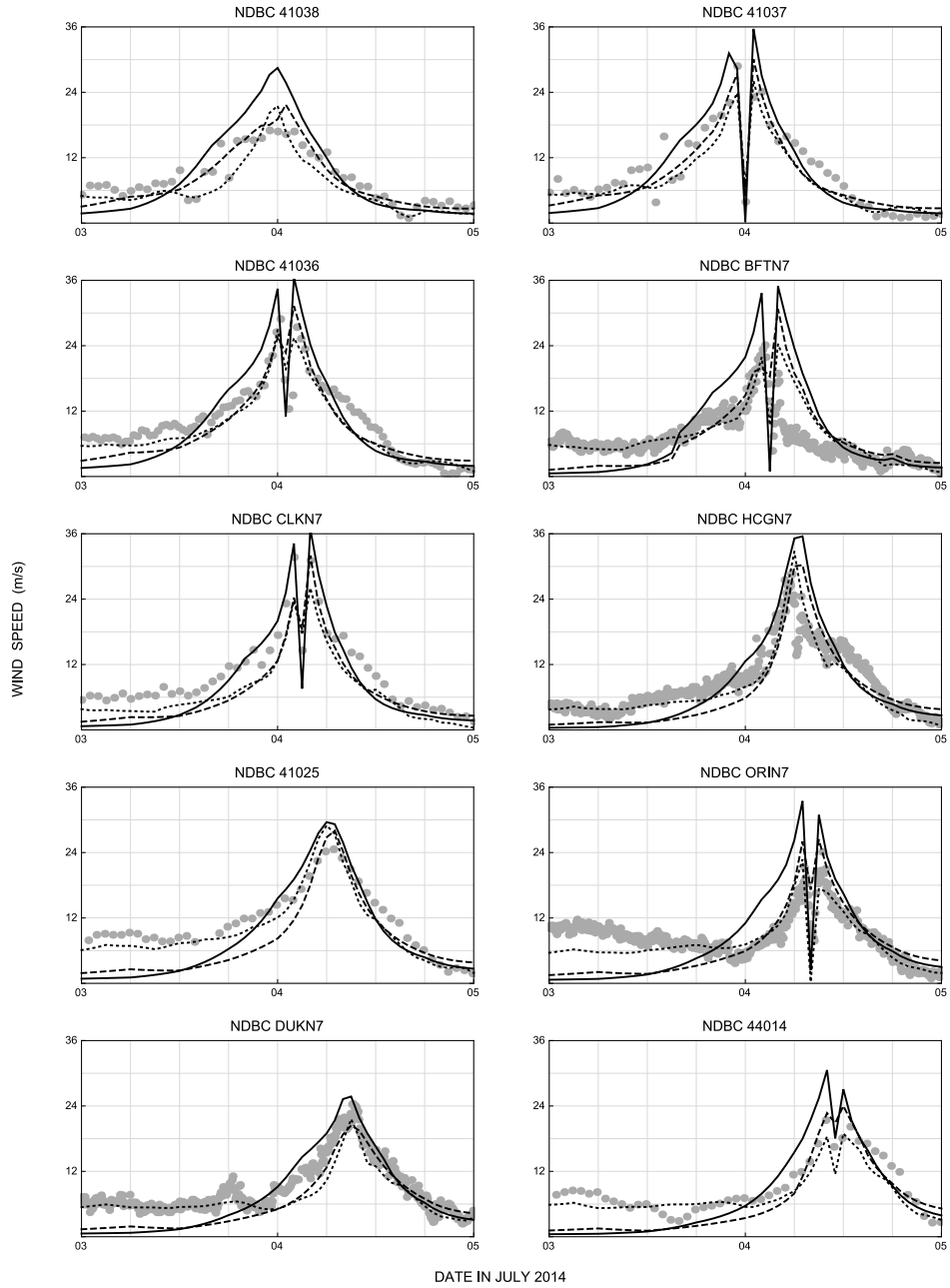


Figure 2.5 Time series of observed and predicted wind speeds (m/s) from hindcast simulations at 10 stations with locations described in Table 2.2 and Figure 2.1. Gray circles indicate observations, and the lines indicate predictions from (dotted) *HWind*, (solid) *GAHM(BT)*, and (dashed) *GAHM(HWind)*.

the NDBC stations 41037 and BFTN7, the peak wind speed is overpredicted by *HWind* as above 34 m/s, when the observed peaks are less than 30 m/s at these locations. At stations farther east, such as the stations at Oregon Inlet and Duck, the observed peaks were between 24 – 27 m/s, but *GAHM(BT)* overpredicts by as much as 8 m/s. Many of these errors are corrected in *GAHM(HWind)*, which has wind speeds that are a better match to the peak winds. The model predictions are compared to observations using statistical measures including mean normalized bias (B_{MN} , which is a measure of the model’s magnitude of over- or under-prediction normalized to the observed value, with an ideal value of zero):

$$B_{MN} = \frac{\frac{1}{N} \sum_{i=1}^N E_i}{\frac{1}{N} \sum_{i=1}^N |O_i|}$$

and root-mean-squared difference (*RMS*, which is a measure of the magnitude of the error, with an ideal value of zero):

$$RMS = \sqrt{\frac{1}{N} \sum_{i=1}^N E_i^2}$$

where O is the observed value, E is the error in terms of model minus observed, and N is the number of observations (or computational points, for later comparisons). For these 10 stations with observations of wind speeds, the *RMS* difference is nearly doubled from 2.69 m/s for *HWind* to 4.63 m/s for *GAHM(BT)*, but it is lowered to 3.79 m/s for *GAHM(HWind)* (Table 2.4). All three hindcasts show a slightly negative B_{MN} ranging from -0.05 for *GAHM(BT)* to -0.17 for *GAHM(HWind)*. It is noted that *GAHM(HWind)* does not contain the background wind and pressure fields, and thus it cannot represent the wind speeds of 6 – 8 m/s before and after the storm (such as those during the first 12 hr of Figure 2.5). The negative bias values for *GAHM(BT)* and *GAHM(HWind)* reflect the combined effect of the under prediction of observed wind speeds prior to the storm and over estimation at the peak. *HWind* is a post-storm, data assimilated wind product and is expected to provide a more accurate representation of Arthur compared to parametric vortex models that utilize limited storm information. The *HWind* errors can therefore be seen as a baseline, to which the *GAHM* simulations can be compared in later sections.

Water Levels – Arthur had a significant effect on water levels throughout coastal NC, particularly by the generation of storm surge within the shallow sounds. At 2014/07/04/0000 UTC as the storm was still offshore, the water levels were increased by less than 0.5 m along the NC coast and in Pamlico and Albemarle Sounds. Three hours later, as the storm made its initial landfall at 2014/07/04/0300 UTC, the water levels had increased along the barrier islands to the south of Hatteras Island near Cape Lookout, NC. Wind and wave forcing were primarily responsible for this surge. At this time, the water levels were between 1 – 1.5 m where the storm made its first landfall near Beaufort, NC, and between 0.5 – 1.25 m in the Neuse and Pamlico Rivers extending inland from Pamlico Sound.

Table 2.4 Error statistics for the three hindcast simulations, for both wind speeds and water levels, with comparisons to the available observations in the region, and at every computational point with depths less than 10 m.

Simulation	Comparison to Observations				Comparison to <i>HWind</i>			
	Wind Speeds		Water Levels		Wind Speeds		Water Levels	
	B_{MN}	RMS	B_{MN}	RMS	B_{MN}	RMS	B_{MN}	RMS
<i>HWind</i>	-0.12	2.69	-0.17	0.16				
<i>GAHM(BT)</i>	-0.05	4.63	-0.03	0.19	0.38	5.90	0.24	0.30
<i>GAHM(HWind)</i>	-0.17	3.79	-0.20	0.17	0.08	2.47	0.00	0.13

By 2014/07/04/0600 UTC, the eye of the storm was centered over Pamlico Sound (Figure 2.6, left column), and water was pushed away from the Outer Banks creating storm surges between 0.5 – 1.75 m in the bays and channels extending from the northern parts of Pamlico Sound. Storm surge between 1.5 – 2 m also existed in the rivers and channels (Neuse and Pamlico River) along the southern and shallower parts of Pamlico Sound. There is significant variability in the water level predictions, both at this time and in the maxima during the storm (Figure 2.6, left and center columns). *HWind* predicts peak water levels of about 1.5 m along the ocean-side of the barrier islands between Capes Lookout and Hatteras, and along the sound-side of Hatteras Island north of its cape. In *GAHM(BT)*, these peaks are increased to more than 2 m, and additional flooding is experienced along the Neuse River estuary. The peak water levels in *GAHM(BT)* are higher than in *HWind* by almost 0.5 m along the barrier islands, and by more than 1 m

in the estuaries on the west side of Pamlico Sound. These differences are decreased for $GAHM(HWind)$ due to its improved representation of the wind fields.

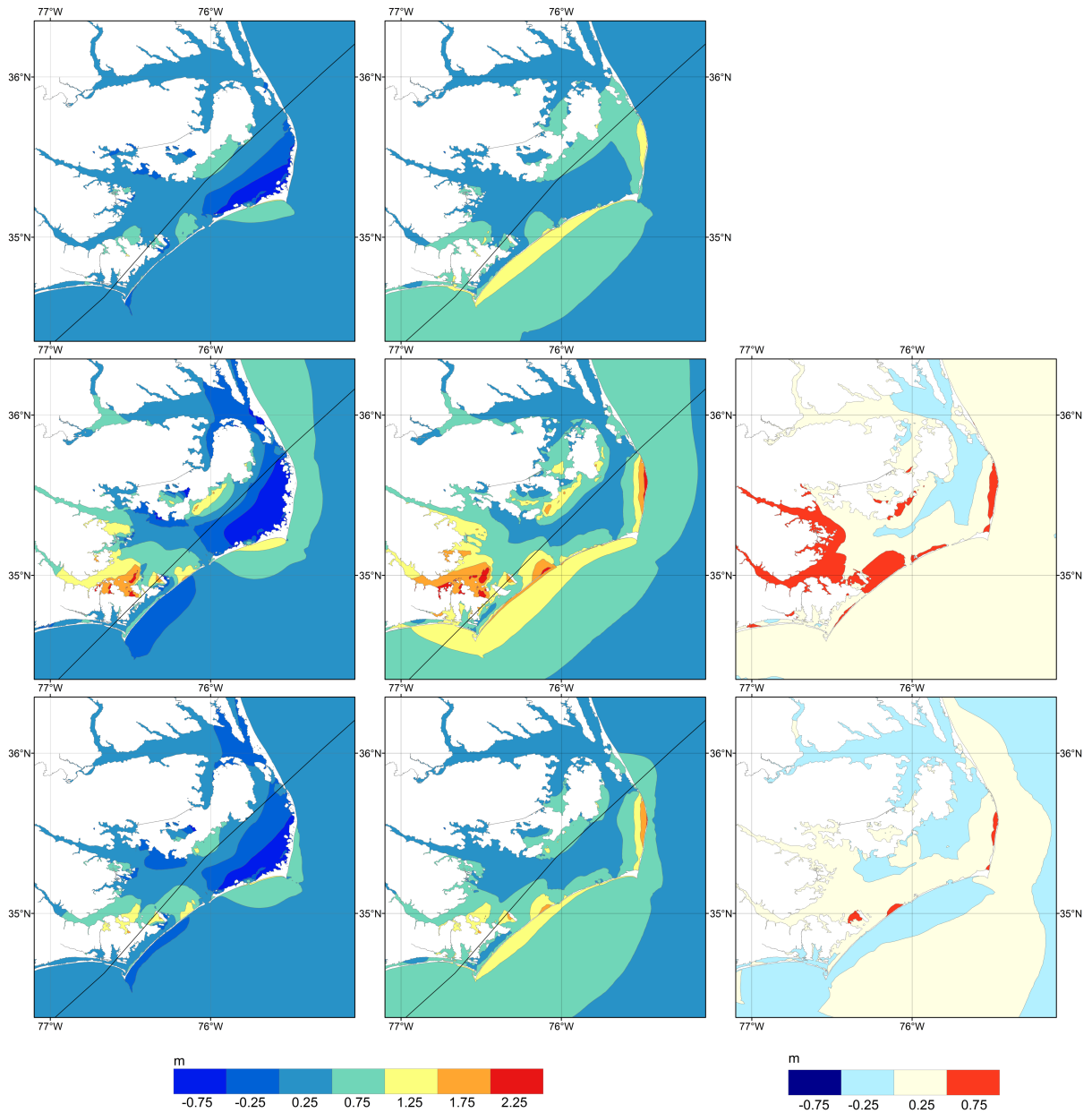


Figure 2.6 Hindcasts of water levels (m) during Arthur in coastal North Carolina. Rows correspond to: (top) $HWind$, (middle) $GAHM(BT)$, and (bottom) $GAHM(HWind)$. Columns correspond to: (left) water levels at 2014/07/04/0600 UTC, (center) maximum water levels, and (right) difference in maximum water levels relative to $HWind$.

The storm’s effects on the shallow waters along the NC coast are evident in a comparison to observations at six locations described in Figure 2.1 and Table 2.2. At NOS station 8656483 (Beaufort), which is located near the path of the storm, the water levels predicted by the model using the best-track information agree well with the observations (Figure 2.7). The northeasterly winds blowing over coastal NC created a storm surge, which matches within 0.2 m of the peak for all three hindcasts. At NOS station 8652587 (Oregon Inlet Marina), *GAHM(BT)* predicted a pre-peak drawdown of 0.3 m, while *HWind* showed rising water levels as the storm approached this location. The USGS stations are representative of locations farther inland in the river channels extending from the sounds. At USGS station 02084472 (Pamlico River), the observed peak water level of 0.6 m is bracketed by the model predictions, with *HWind* too low, and *GAHM(BT)* too high. At USGS station 0208114150 (Roanoke River), the observed peak water level is matched well by *GAHM(BT)*, but *HWind* is too low by 0.3 m. At NOS station 8651370 (Duck Pier), which is located to the east of Currituck Sound on the open Atlantic coast and farthest to the north (among all the stations), the storm does not cause an observable change from the tidal cycle, but the overestimated winds in *GAHM(BT)* cause the peak water levels to be overpredicted by 0.1 – 0.2 m.

Error statistics are computed for modeled and observed water levels at 8 observation stations (Table 2.4). The *RMS* differences are between 0.16 – 0.19 m for the three hindcasts, indicating a generally-good match between the predictions and the observations. However, these errors are highly dependent on station location relative to the storm track. To better represent the spatial distribution of errors in the region, the B_{MN} and *RMS* differences were computed for peak water levels between *HWind* and the *GAHM* hindcasts at every computational point (mesh vertex) with depth less than 10 m (similar to the analysis in (Forbes et al., 2010)). Relative to the *HWind* simulation, the *GAHM(BT)* peak water levels were too high, with a positive bias of 0.24 m and a root-mean-square error of 0.30 m in the region. The relatively-good bias for *GAHM(BT)* simulation reflects model performance over a full simulation. Water levels were overpredicted during the storm, the resulting positive bias is offset to a certain degree by the underprediction prior to the storm due to the absence of background winds. When the *HWind* storm parameters were used to construct the vortex wind field in *GAHM*, the *GAHM(HWind)* peak water levels were a close match, with a bias near zero and a root-mean-square error of 0.13 m. These values are much closer to the errors for *HWind* (Table 2.4), which again

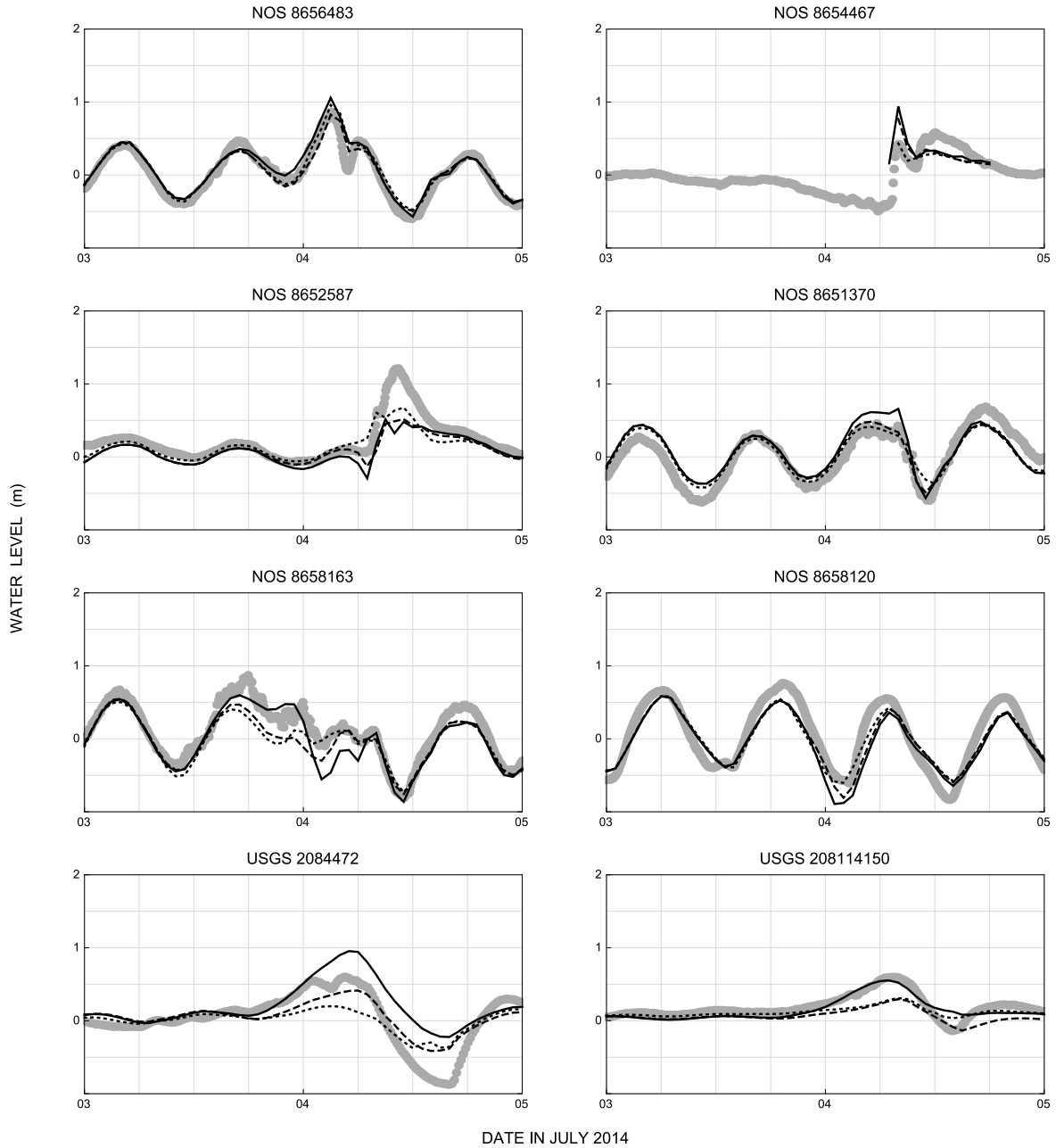


Figure 2.7 Time series of observed and predicted water levels (m) from hindcast simulations at 8 stations with locations described in Table 2.2 and Figure 2.1. Gray circles indicate observations, and the lines indicate predictions from (dotted) *HWind*, (solid) *GAHM(BT)*, and (dashed) *GAHM(HWind)*.

can be seen as a baseline to which to compare the GAHM simulations. Taken together, these analyses show that the *HWind* hindcast is the best representation of the winds and water levels during Arthur in coastal NC. However, *GAHM(HWind)* also matches well to the storm’s behavior and effects on the coastal ocean, and thus GAHM can be used to explore forecast errors.

2.5.1.2 Forecasts

During Arthur, the ASGS system was running simulations of SWAN+ADCIRC to predict the storm-driven waves and flooding along coastal NC (<http://nc-cera.renci.org>). Using the forecast advisories issued by the NHC, those simulations were forced by vortex wind and pressure fields from the Asymmetric Holland Model (AHM, (Mattocks et al., 2006; Mattocks et al., 2008)), the predecessor to GAHM. Herein, we evaluate the performance of GAHM by using the same forecast advisories as input, and thus these simulations can be considered as forecasts. While guidance was developed for all forecast advisories during the storm, we focus on three forecasts:

- Advisory 4, issued 2014/07/01/2100 UTC, about 54 hr before landfall
- Advisory 8, issued 2014/07/02/2100 UTC, about 30 hr before landfall
- Advisory 12, issued 2014/07/03/2100 UTC, about 6 hr before landfall

As noted previously, the storm track was fairly consistent during the early forecasts, with a projected movement offshore of coastal NC, but then the storm track changed during the forecasts issued in the last 24 hr before landfall, toward a projected landfall near Beaufort, NC.

These storm track errors cause variability in the wind and surge predictions (Figure 2.8). In the earlier advisories 4 and 8, the hurricane-strength winds (with speeds larger than 32 m/s) are located offshore, while coastal NC is subjected to lesser winds of tropical-storm- or tropical-depression-strength (Figure 2.8, left column). Wilmington and Cape Fear are forecast to experience maximum wind speeds of about 20 m/s, and the sounds and Outer Banks are forecast to experience maximum wind speeds of 25 – 30 m/s. By advisory 12, the track shows the storm’s correct movement over Pamlico Sound, and thus the entire region is subjected to wind speeds corresponding to a Category 1 storm on the Saffir-Simpson scale. The predicted maximum wind speeds are almost 40 m/s along a

swath from Beaufort through Oregon Inlet, and thus effectively doubled from the earlier forecasts.

The track predictions from the later forecast (e.g., NHC advisory 12, issued 6 hr before initial landfall) are a better representation of the storm's movement near four stations: 41037 (27 miles SE of Wrightsville Beach, NC), BFTN7 (Beaufort, NC), CLKN7 (Cape Lookout, NC) and ORIN7 (Oregon Inlet Marina, NC). The sharp drop in wind speed at 2014/07/04/2345 UTC at these stations and the presence of a double peak (Figure 2.9) can be attributed to the influence of the storm eye near these locations; this effect is well-represented by the model wind speeds. However, the model over-predicts the wind speeds. At station 41037, the peak wind speeds for the later forecast (NHC advisory 12) were about 35 m/s, which is larger than the model predictions of 22 m/s from the earlier NHC advisories 4 through 8, but closer to the observed value of 29 m/s. At station BFTN7, the peak wind speeds from the later forecast are 7 m/s larger than the observations, while the peak wind speeds from the earlier forecasts are smaller and occur later than the observations. At station ORIN7, for the earlier forecasts, the errors in the track predictions cause the absence of a double peak and lower predicted peak wind speeds. However, the RMS difference for forecast advisory 4 at these four stations is about 5 m/s and is smaller than that of forecast advisory 12. Thus, while the later forecast advisory 12 is a better representation of the storm's track near these stations, their *RMS* differences are larger due to over-predictions of the wind speeds as Arthur moved through the system.

The effect is reversed at stations located farther offshore. At station 41025 (Diamond Shoals, NC) located southwest of Hatteras Island, NC, the wind speeds decrease sharply at the peak to less than 15 m/s and less than 5 m/s for forecast advisories 4 and 8, respectively, before rising again (Figure 2.9). This behavior is indicative of the eye of the storm being simulated at this location, due to the erroneous storm trajectories predicted to pass over this station. For these earlier forecasts, the wind speeds are higher than the observations by about 5 m/s. At station 41025, the *RMS* differences are about 5.2 m/s for advisories 4 and 8, but they increase to about 5.6 m/s for the later advisory 12, during which the peak wind speeds are over-predicted by 9 m/s. These comparisons indicate that errors in track predictions can lead to over- or under-prediction of wind speeds at locations far or near to the actual storm track.

The ocean responded differently to these wind predictions. In the earlier advisories

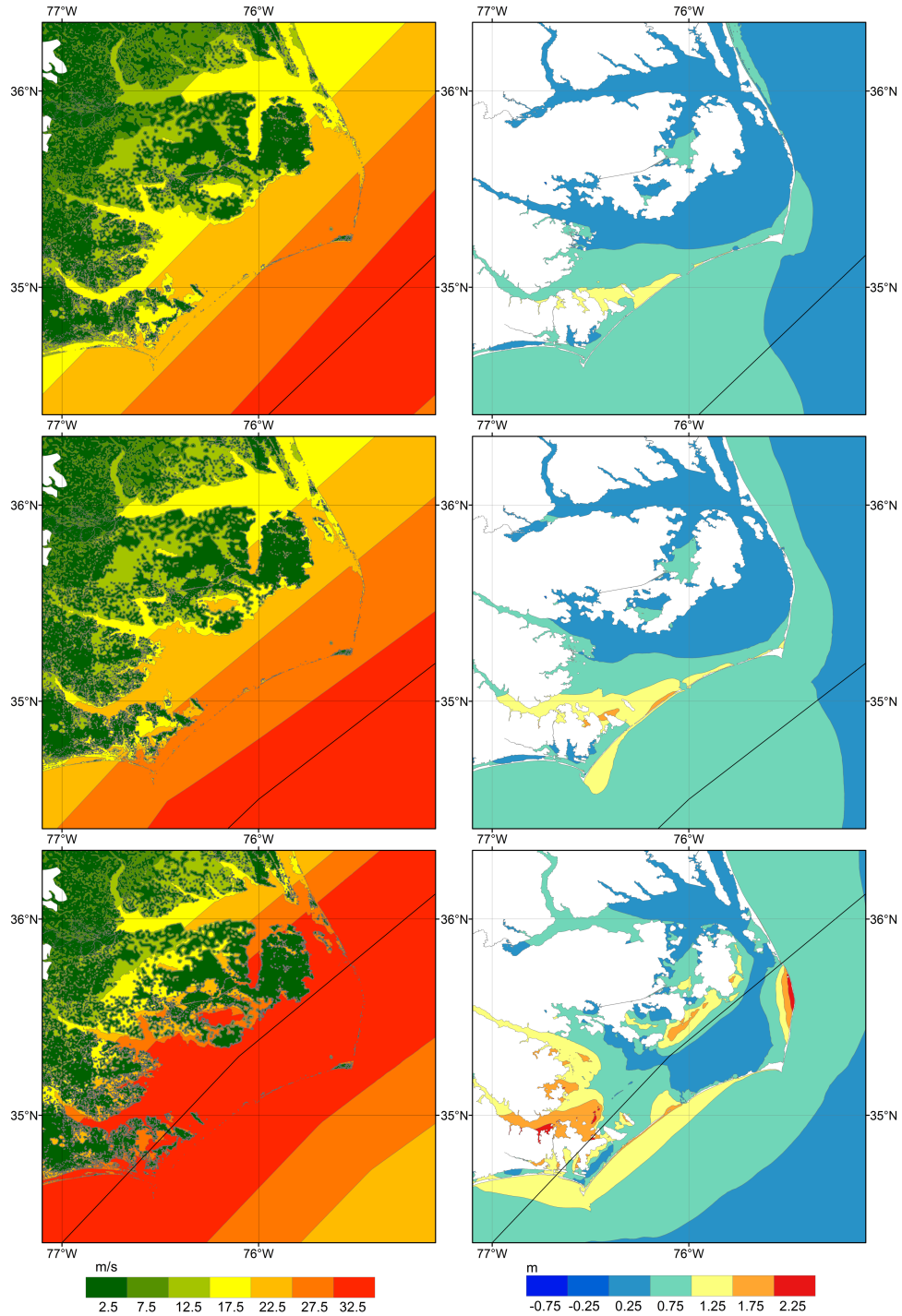


Figure 2.8 Forecasts of winds (m/s) and water levels (m) during Arthur in coastal North Carolina. Rows correspond to: (top) *GAHM(4)*, (middle) *GAHM(8)*, and (bottom) *GAHM(12)*. Columns correspond to: (left) maximum wind speeds, and (right) maximum water levels.

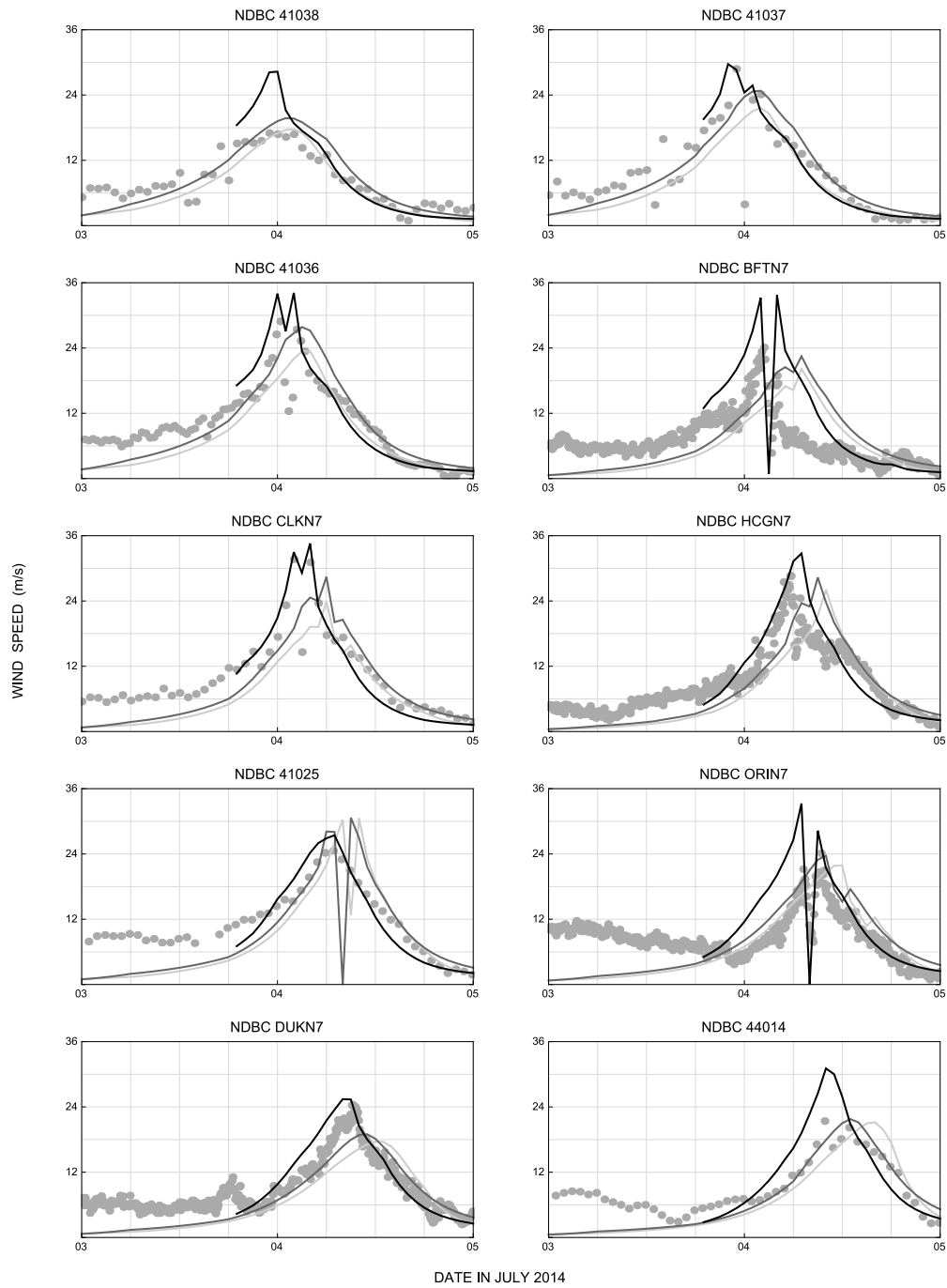


Figure 2.9 Time series of observed and predicted wind speeds (m/s) from forecast simulations at 10 stations with locations described in Table 2.2 and Figure 2.1. Gray circles indicate observations, and the lines indicate predictions for (lighter gray) $GAHM(4)$, (darker gray) $GAHM(8)$, and (black) $GAHM(12)$.

4 and 8, the winds are easterly and then northerly as the storm moved offshore, and thus water was pushed in a southwestward direction (Figure 2.8, right column). Water levels were decreased in the eastern Pamlico and Albemarle Sounds, and increased in southwestern Pamlico Sound and the Neuse River estuary. The maximum water levels are about 1 m along the ocean-side of the Outer Banks between Capes Lookout and Hatteras, and about 1.5 m in southwest Pamlico Sound. By advisory 12, the predicted storm effects are increased throughout the region. Water levels higher than 2 m are pushed into the Neuse River and against the sound-side of Hatteras Island, and the maximum water levels have increased along the ocean-side of the Outer Banks. This later forecast is qualitatively similar to the wind and surge predictions in the hindcasts (Figures 2.4 and 2.6).

Comparisons at 8 stations show the evolution of the water-level predictions (Figure 2.10). At station 8656483 (Beaufort, NC), which is located near the path of the storm, the peak water levels predicted in the earlier advisories 4 and 8 were lower than the observed values by about 0.40 m. At station 8652587 (Oregon Inlet Marina), the forecasts showed a drawdown of as much as 0.5 m during advisories 4 and 8. However, there was a rise in water level of about 1.25 m at this location. This rise is evident in predictions based on later advisories (as in advisory 12), but the model under-predicts the observed peak surge by about 0.5 m, likely because this rise was not sufficient to counter the modeled drawdown of 0.25 m that occurred a few hours prior to the rise in surge. This drawdown was not observed and can be attributed to overestimation of the winds.

To quantify the change in model performance over time, the B_{MN} and RMS are computed in two ways. First, these quantities are computed relative to the observations at the 10 wind and 8 water-level stations. Error statistics were averaged in time at each station, and then averaged over the stations; these are the dashed lines in Figure 2.11. Despite the improvement in storm track projections in the later advisories, the error statistics do not show any clear improvement. For the wind speeds, the RMS difference is relatively constant at 4 m/s, and for the water levels, the RMS difference is steady at 0.25 m until it decreases at the last advisory. Second, these quantities were computed relative to the peak values in the $HWind$ hindcast simulation; these are the solid lines in Figure 2.11. For the wind speeds, the peak values were compared at every point in the computational domain; for the peak water levels, the comparison was limited to points with depths less than 10 m. For this comparison of peak values, there is a clear increase in

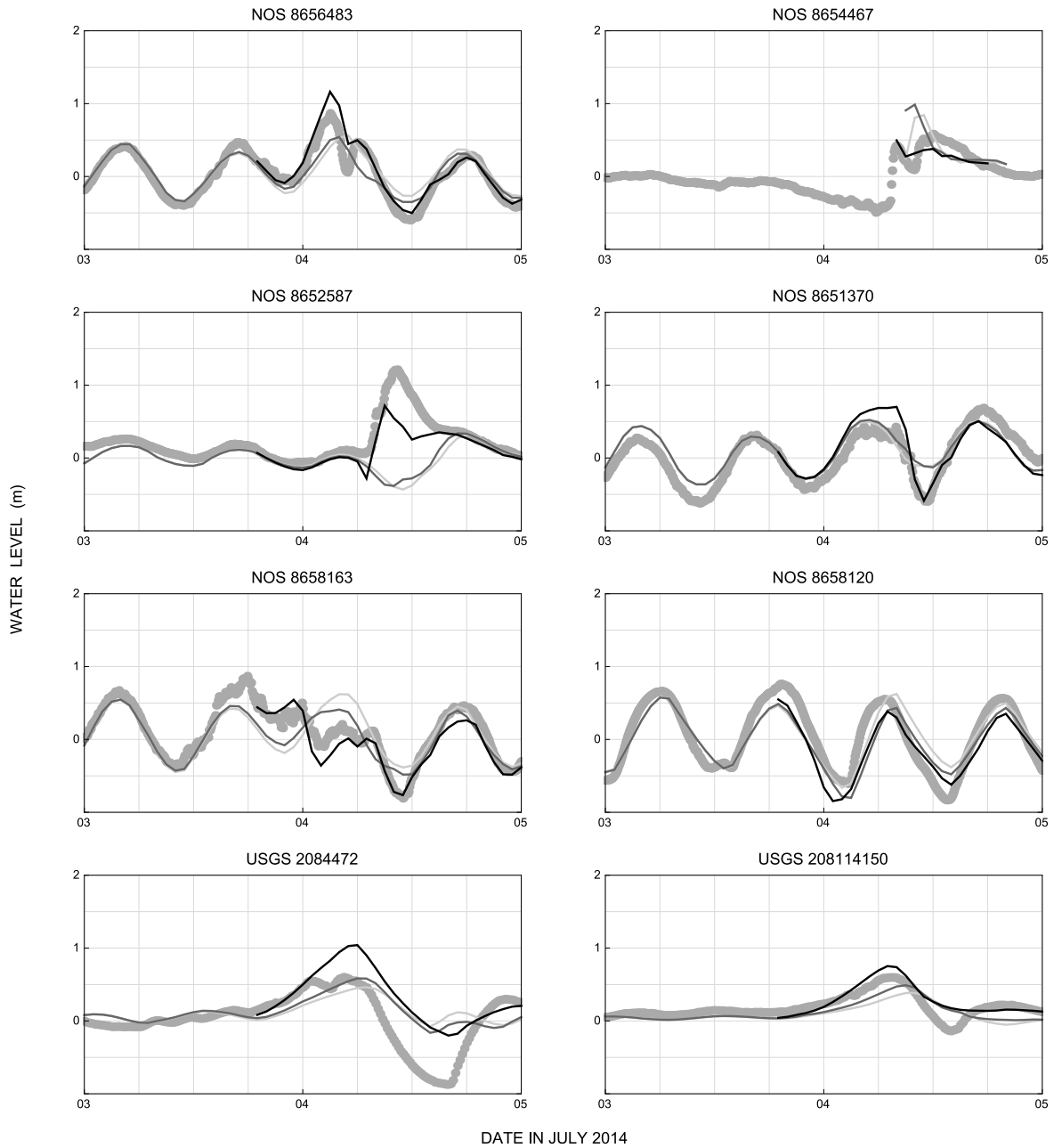


Figure 2.10 Time series of observed and predicted water levels (m) from forecast simulations at 8 stations with locations described in Table 2.2 and Figure 2.1. Gray circles indicate observations, and the lines indicate predictions for (lighter gray) $GAHM(4)$, (darker gray) $GAHM(8)$, and (black) $GAHM(12)$.

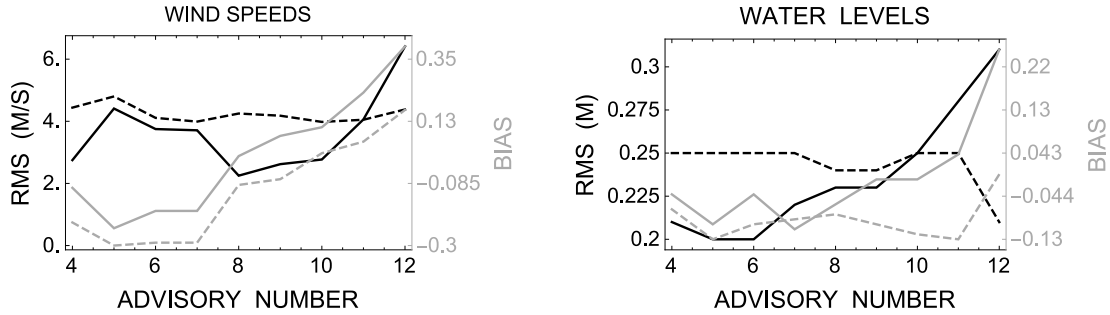


Figure 2.11 Error statistics for the forecast simulations using NHC advisories 4 through 12. Columns correspond to (left) winds and (right) water levels. Error statistics are shown for (black) RMS and (gray) B_{MN} , with comparisons to (dashed) observations and (solid) $HWind$ hindcast simulation.

the errors at the later advisories 10-12, during the day before the storm’s initial landfall. The global RMS errors increase in NHC advisory 12 to 6.47 m/s for winds, and 0.31 m for water levels. The forecasts were not converging to the storm as represented by the $HWind$ hindcast ($RMS = 2.69$ m/s for winds, $RMS = 0.16$ m for water levels).

2.5.2 Error due to Storm Track

To control for the relative effects of errors in storm track and storm strength, the forecast simulations were repeated, but with parameters from the $HWind$ hindcast. To examine the affects of errors due to storm track, GAHM was employed with the storm track from each NHC forecast advisory, but with parameters for storm size and intensity from the $HWind$ analysis product (as summarized in Table 2.3). For example, $GAHM(4, HWind)$ denotes a simulation with the storm track from NHC forecast advisory 4, but parameters for storm size and intensity from the $HWind$ hindcast. Thus, the same storm is applied on forecast tracks, which converge toward the true landfall location.

The power dissipation for $HWind$ (about $1.87 \cdot 10^{12}$ watts) was similar to that for $GAHM(4)$ (about $2.04 \cdot 10^{12}$ watts), and thus the projected storm size and wind speed were generally consistent at this time. The swath of hurricane-strength winds was located entirely offshore, and only the barrier islands and Pamlico Sound experienced tropical-storm-strength winds (Figure 2.12, top left). For NHC advisory 8 issued 24 hr later, there is a noticeable improvement in the maximum wind speeds, and thus the associated

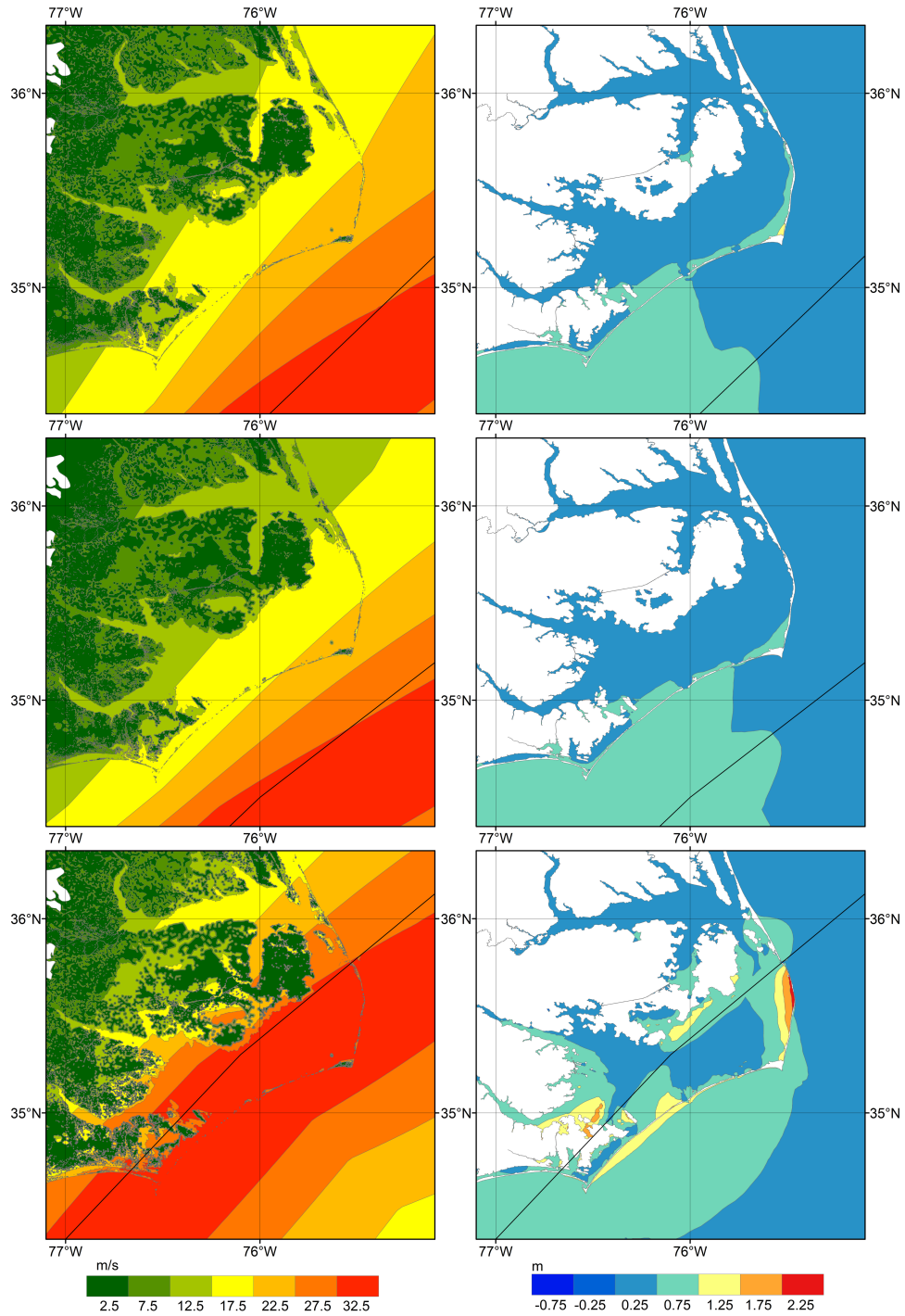


Figure 2.12 Forecasts of winds (m/s) and water levels (m) during Arthur in coastal North Carolina, but with constant storm size and intensity parameters from HWind. Rows correspond to: (top) $GAHM(4, HWind)$, (middle) $GAHM(8, HWind)$, and (bottom) $GAHM(12, HWind)$. Columns correspond to: (left) maximum wind speeds, and (right) maximum water levels.

water-level response. For the *GAHM(8)* simulation (Figure 2.8, middle row), the tropical-storm-strength winds larger than 18 m/s extended throughout coastal NC, and pushed water levels larger than 1.5 m in the southwest Pamlico Sound. For the *GAHM(8,HWind)* simulation (Figure 2.12, middle row), the maximum wind speeds are much smaller in coastal NC, and the associated water-level response is negligible. The maximum wind speeds are also smaller for *GAHM(12,HWind)*, with hurricane-strength winds confined to the barrier islands and Pamlico Sound (Figure 2.12, bottom row). The projected water levels have similar peak values of about 2 m, but these peaks are confined to smaller regions along the sound-side of Hatteras Island, and near the Neuse River estuary.

The error statistics show how the wind and water-level predictions are sensitive to track errors. For the wind speeds, the RMS and bias errors converge both with later advisories and landfall error (Figure 2.13, left column). For the early advisories 4-7, the global RMS errors are larger than 5.6 m/s, but they decrease to 2.83 m/s for advisory 12, which is only slightly larger than the RMS error computed for *HWind* wind speeds (2.69 m/s, Table: 2.4). This convergence is linked to the landfall error, which decreases from 137 km for advisory 5 to less than 9 km for advisory 12. The global RMS errors for the wind speeds decrease gradually as the storm track shifted toward coastal NC.

The water levels did not converge gradually as the storm track is improved (Figure 2.13, right column). Instead, the global RMS errors are relatively constant for advisories 4-11 at about 0.2 m, even as the landfall error decreases by more than 120 km. It is only during advisory 12, in which the projected track had the storm moving correctly over coastal NC, when the errors are improved. For *GAHM(12,HWind)*, the global RMS error improves to 0.13 m, and the global bias improves to 0.03. These statistics are slightly better than the computed RMS error and bias for the *HWind* water levels that are equal to 0.16 m and -0.17 respectively (Table 2.4). These results show the nonlinearity of the water-level response. The drop in both station and global RMS errors from *GAHM(11,HWind)* to *GAHM(12,HWind)* is attributed to differences in the tracks of advisories 11 and 12. The initial landfall error of about 15 km for advisory 11 is similar to the initial landfall error of less than 9 km for advisory 12, but their tracks diverge over coastal NC. The track of advisory 11 predicted the storm center to move along the eastern edge of Pamlico Sound with a potential landfall at Hatteras Island, thereby causing a significant drawdown in parts of the northern Pamlico Sound (not shown). Forecast corresponding to advisory 12, however, shifted the track west and provided

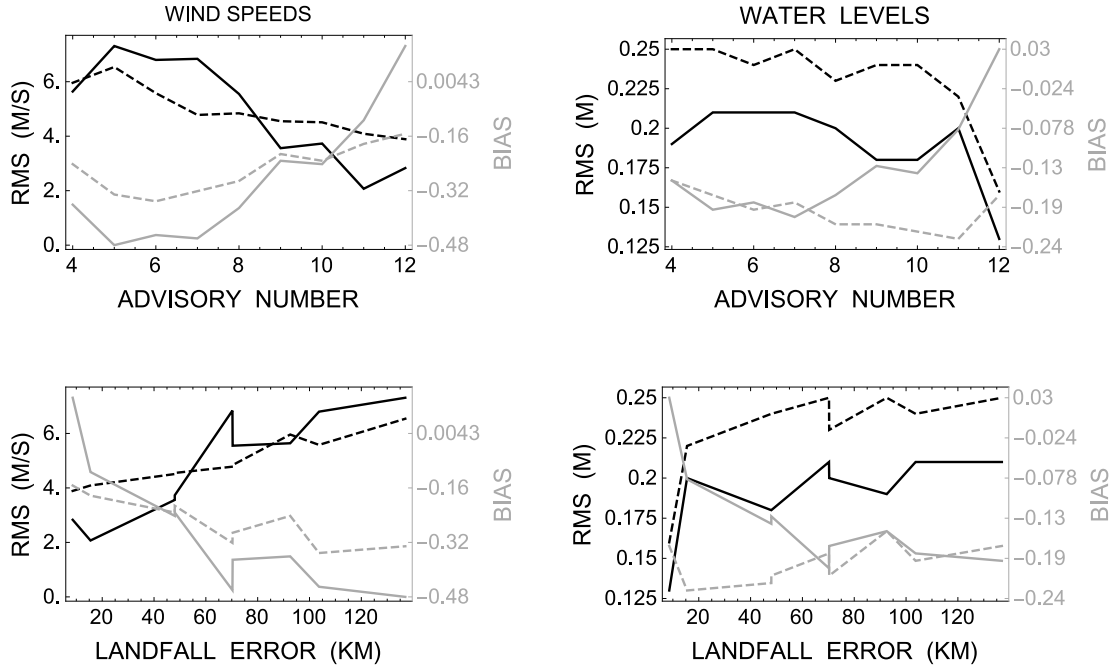


Figure 2.13 Error statistics for the forecast simulations using NHC advisories 4 through 12 for storm track, but *HWind* parameters for storm size and intensity. Columns correspond to (left) winds and (right) water levels. Rows show the same information, but for (top) advisory number and (bottom) landfall error (km). Error statistics are shown for (black) *RMS* and (gray) *B_{MN}*, with comparisons to (dashed) observations and (solid) *HWind* hindcast simulation.

a more accurate representation of the storm center’s real path. Thus, in contrast to *GAHM(11,HWind)*, the entire eastern portion of the Pamlico Sound fall to the right of the storm center for *GAHM(12,HWind)* and experience positive surges, which are a better match to measured water levels and *HWind* hindcast results. As the storm size and intensity are held constant, and as the storm track is improved gradually, the water level predictions do not change until the wind speeds and directions are correct in coastal NC.

2.5.3 Error due to Storm Size and Intensity

As the forecast track was converging to the correct landfall location, the forecast storm was increasing in power dissipation (Figure 2.2). By advisory 12, the forecast power dissipation of $3.10 \cdot 10^{12}$ watts was more than 50 percent larger than the post storm

determined power dissipation of $1.87 \cdot 10^{12}$ watts in the *HWind* simulation. To examine the effects of this overestimation of storm power on the surge and coastal flooding, we repeated the forecast simulation while holding the storm track constant as determined from the *HWind* fields (see Table 2.3). For example, *GAHM(HWind,4)* denotes a simulation with parameters for storm size and intensity from NHC forecast advisory 4, but the storm track from the *HWind* hindcast. Thus, the same track is used for the forecast storms, which increases in power dissipation.

These simulations show the growth of the storm in size and intensity in subsequent forecasts (Figure 2.14, left column). In *GAHM(HWind,4)*, much of the NC coastal regions see maximum wind speeds greater than 18 m/s (corresponding to a tropical storm), but the largest maximum wind speeds greater than 33 m/s (Category 1 hurricane) are confined over the Outer Banks and Cape Hatteras. In the later forecast advisories, this region of hurricane-strength maximum winds is expanded to include all of Pamlico Sound and, in *GAHM(HWind,12)*, regions to the west of the *HWind* hindcast track. There is a correlation between the forecast increase in power dissipation and the global root-mean-square and bias errors in the simulated wind fields (Figure 2.15, left column). As the power dissipation is increased, the global *RMS* errors increase from about 3.6 m/s for advisories 4 and 5, to more than 5 m/s for advisories 11 and 12. This correlation is not perfect, e.g., the largest global *RMS* error is observed for advisory 11, when the power dissipation was $2.6 \cdot 10^{12}$ watts and thus less than its maximum value. And there is no correlation for the error statistics computed relative to the observations, e.g., their *RMS* errors are consistently 4 – 5 m/s, which is larger than the *RMS* errors for *HWind* wind speeds (2.69 m/s, Table 2.4), regardless of the power dissipation of the forecast storm. However, the global error statistics do increase as the forecast storms increase in strength.

A similar behavior can be observed for the maximum water levels (Figure 2.14). In *GAHM(HWind,4)*, the largest water levels of 1.5 m or greater are confined to southwest Pamlico Sound and the Neuse River estuary. In the later forecast advisories, these water levels increase in magnitude, similar peaks in water levels are evident on the sound-side of Hatteras Island north of its cape, and on the ocean-side of the Outer Banks between Capes Lookout and Hatteras. As the forecast storms increase in power, they push water more effectively. This correlation is seen in the error statistics for the water levels (Figure 2.15, right column). The global *RMS* errors increase from about 0.24 m in advisories 4 and 5, to about 0.28 m in advisories 11 and 12, and the global bias increases from

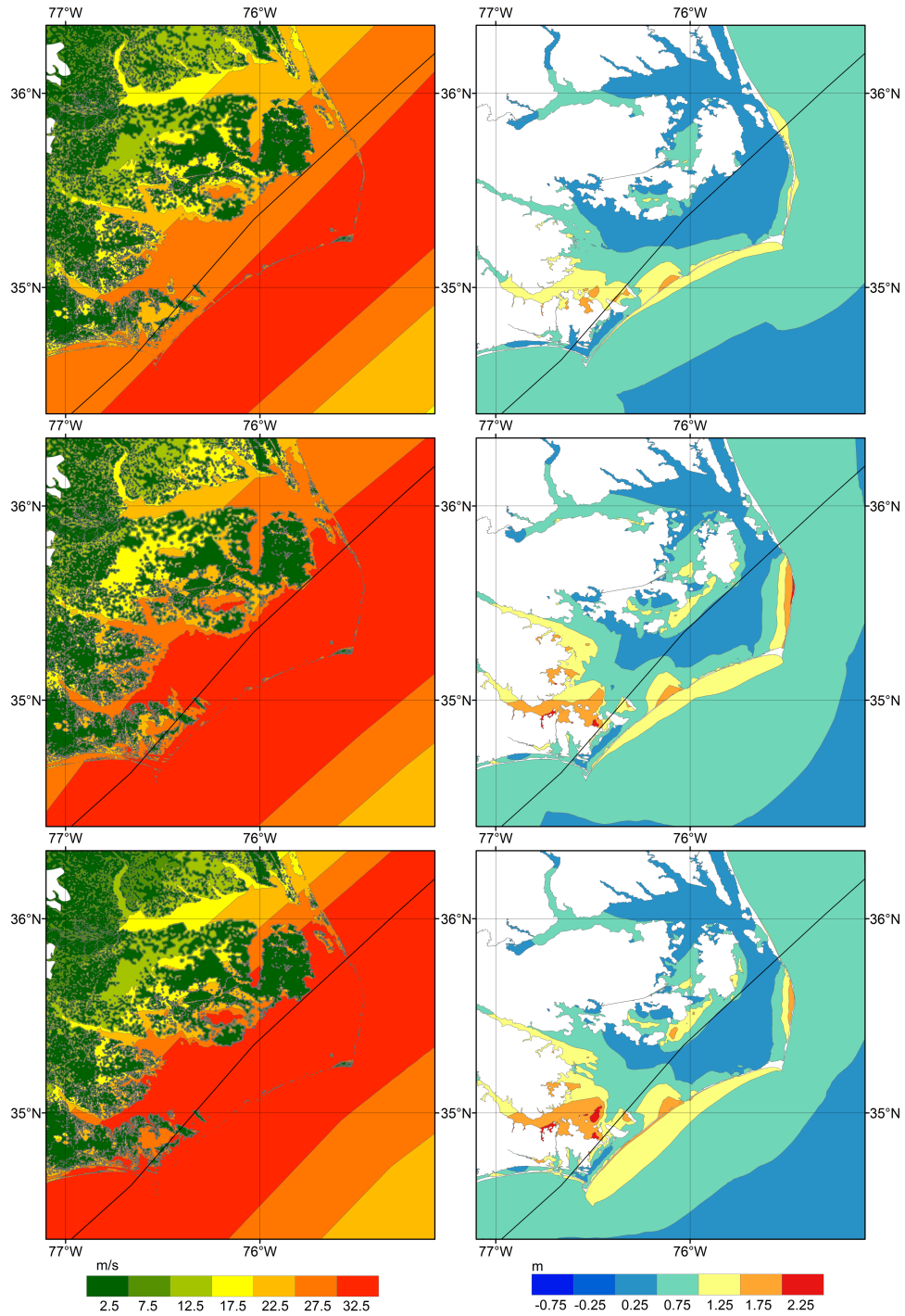


Figure 2.14 Forecasts of winds (m/s) and water levels (m) during Arthur in coastal North Carolina, but with constant track information from HWind. Rows correspond to: (top) $GAHM(HWind,4)$, (middle) $GAHM(HWind,8)$, and (bottom) $GAHM(HWind,12)$. Columns correspond to: (left) maximum wind speeds, and (right) maximum water levels.

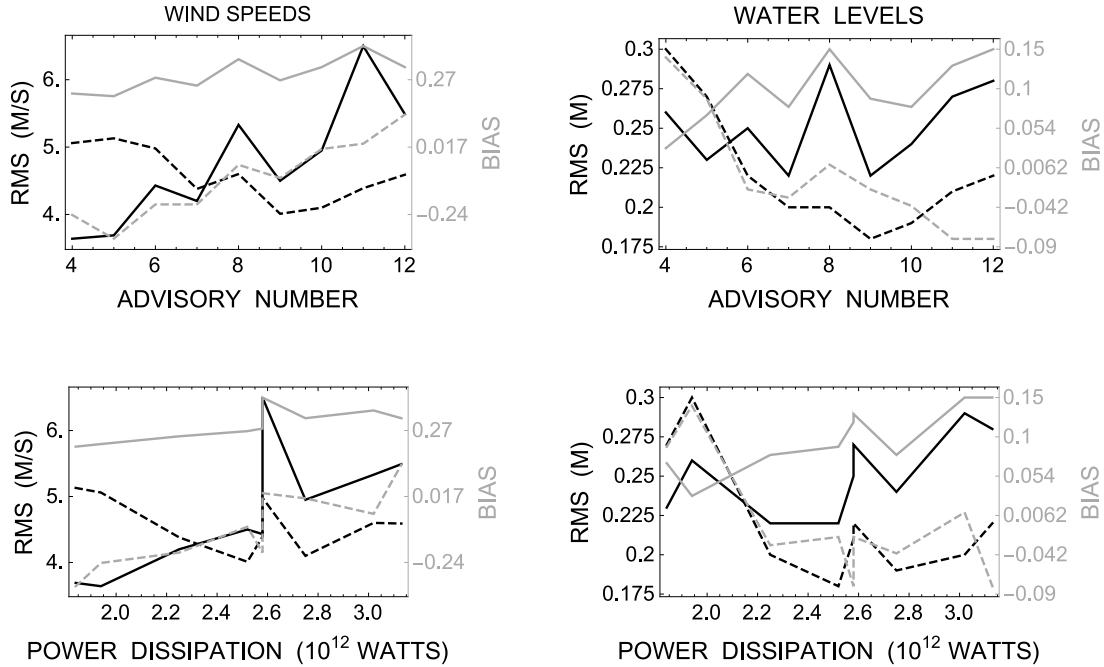


Figure 2.15 Error statistics for the forecast simulations using NHC advisories 4 through 12 for storm size and intensity, but *HWind* parameters for storm track. Columns correspond to (left) winds and (right) water levels. Rows show the same information, but for (top) advisory number and (bottom) power dissipation (10^{12} watts). Error statistics are shown for (black) *RMS* and (gray) *B_{MN}*, with comparisons to (dashed) observations and (solid) *HWind* hindcast simulation.

about 0.03 to about 0.15. The RMS errors computed relative to observations are larger than that of *HWind* water levels (0.16 m, Table 2.4) and stay above 0.25 m for most of the advisories and rise up to 0.3 m for advisory 12. These increases correlate with the increasing power dissipation, although not as strongly as for the wind speeds, thus indicating the nonlinearity of the coastal ocean response.

2.6 Summary

The SWAN+ADCIRC modeling system was applied to high-resolution simulations of storm surge and coastal flooding during Hurricane Arthur (2014). The surge model was forced with wind velocities from the *HWind* analysis product, and surface pressures and wind velocities from the GAHM parametric vortex model. The effects of the atmospheric

forcing were evaluated for hindcasts using the best-available information after the storm, as well as for forecasts containing information released as the storm approached NC. Then, by repeating the forecast simulations and replacing their uncertainties with known information from after the storm, we quantified the errors in computed wind speeds and water levels due to errors in storm power and track. Our findings can be summarized as follows:

1. *The HWind simulation was the best representation of Arthur’s wind hazards and associated ocean response, but GAHM(HWind) was a close approximation.* The HWind wind fields and water levels were the best match to observations at stations offshore and in coastal NC. When GAHM was used with the NHC best-track information as *GAHM(BT)*, it did not match as well at the observations, but its performance improved considerably when the best-track information was replaced with parameters from HWind as *GAHM(HWind)*. Thus, given correct information about the storm’s size, intensity, and track, GAHM can reproduce the key characteristics of the storm.
2. *Forecasts of wind speeds and water levels became less accurate (i.e. deviated more from post-storm determined HWind results) as the storm approached landfall.* For wind speeds, the global root-mean-square error more than doubled, while for the water levels, the global root-mean-square error increased by 50 percent. This deterioration in forecast accuracy was due to the combined errors in storm track and power dissipation (a measure of combined size and intensity). The storm track improved in later advisories, but the forecasted intensity (as represented by the PD) was significantly larger than the post-storm determined intensity. This resulted in forecasts that overpredicted the peak winds and surge.
3. *As the forecast storm track and intensity errors increase, the errors in forecast wind speeds also increase, but the errors in forecast water levels remain relatively consistent.* By using parameters from the HWind analysis product, we repeated the forecast simulations to control for these errors. The wind-speed errors decreased significantly as the storm track converged to the correct landfall location, and they increased significantly as the storm was projected to grow in size and intensity. The water-level errors responded nonlinearly, with only a late improvement when the track became ‘correct,’ and only a slight worsening as the storm became too

powerful. The ocean response will also depend on the tide level, coastline geometry, and other characteristics of the coast.

Although this study is specific to Arthur, it demonstrates the potential for forecast errors in peak wind speeds and surge levels due to separate errors in storm track and power. It is typical for Atlantic storms to follow a shore-parallel track and move near or over coastal NC, such as Irene (2011) and Hermine and Matthew (2016), and thus we are encouraged to continue improving our modeling system to advance storm preparation efforts in North Carolina. Future work will focus on improving the computational speed to make forecast guidance available sooner and to benefit ensemble forecasting, and on improving the communication of forecasts and their potential errors to local stakeholders.

Chapter 3

A 3D Baroclinic Flow Model for the Choctawhatchee Bay and Destin Inlet System

3.1 Overview

This chapter describes the development and validation of a three dimensional baroclinic numerical model to study density driven flows near estuarine systems. The model of choice is the recently enhanced baroclinic ADCIRC, a coastal circulation model that solves momentum and transport equations over large high resolution unstructured grids in which intricate coastlines are well represented. Section 3.2 introduces the study area, near-shore physical processes that are relevant for the present study and ADCIRC. This is followed by a description of the three dimensional governing equations solved by ADCIRC and the unstructured mesh, physical forcings and other parameters associated with the model set-up in Section 3.3. The chapter concludes with Section 3.4, in which model predictions are validated against in-situ observations, satellite imagery and drifter movement.

3.2 Introduction

In the shallow coastal ocean, circulation is typically driven by the complex interaction of tides, winds, waves and density gradients (Blain et al., 2012). These density gradients

are especially prominent in river dominated estuarine systems, owing to low salinities at river mouths and higher salinities near tidal inlets. During the tidal ebb phases, brackish estuarine outflows can form distinct buoyant plumes, near the inlet and the associated density gradients can cause the slowing down and convergence of offshore surface material along the plume edges (Roth et al., 2017). The Choctawhatchee Bay (Figure 3.1) is one of the several estuaries situated in Northwest Florida, which receives significant land drainage and has a limited connectivity to the Gulf waters through narrow tidal inlets. The present study aims to understand features of the tide, wind and density driven circulation within Choctawhatchee Bay and the interaction of the ebb-phase brackish plume at Destin Inlet with the shelf waters.

Coastal circulation models based on unstructured grids, which provide significant flexibility to model complex geometric features along coastlines are typically used to study such river-estuarine-shelf scale processes. Some examples of coastal circulation models that have been successfully applied to model such systems are FVCOM (Chen et al., 2003), SUNTANS (Fringer et al., 2006), ELCIRC (Zhang et al., 2004), SELFE (Zhang et al., 2008) and SCHISM (Zhang et al., 2016). A common approach for studying regional dynamics involves nesting unstructured coastal ocean models with large structured ocean models. This involves specifying realistic forcing at the open boundaries of the local model and can be a cause for inaccuracies. Unstructured grids have the potential to locally refine regions of interest while maintaining coarser resolution elsewhere in a large domain, thereby providing a more effective nesting approach with reasonable computational costs (Danilov, 2013). The present study aims to demonstrate the ability of baroclinic ADCIRC to be applied in this manner by modeling density driven flows over a shelf-scale unstructured grid (previously validated for two dimensional barotropic flows) that has coarse elements over the shelf and finer resolution at the coastline, which captures details of the estuarine environment pertinent to the current research efforts. This study is unique because it is the first time a recently-enhanced, three-dimensional, baroclinic version of the ADvanced CIRCulation (ADCIRC) model (Luettich et al., 1992; Westerink et al., 2008; Fathi et al., 2017), which has been widely applied for depth-averaged tidal and storm surge studies (Bunya et al., 2010; Dietrich et al., 2012b; Cyriac et al., 2018), is applied to represent density-driven estuarine and shelf circulation. This effort will also build confidence for future modeling attempts that aim to make assessments about storm impacts on estuarine salinities and stratification, which are important indicators of the

ecological health of estuaries.

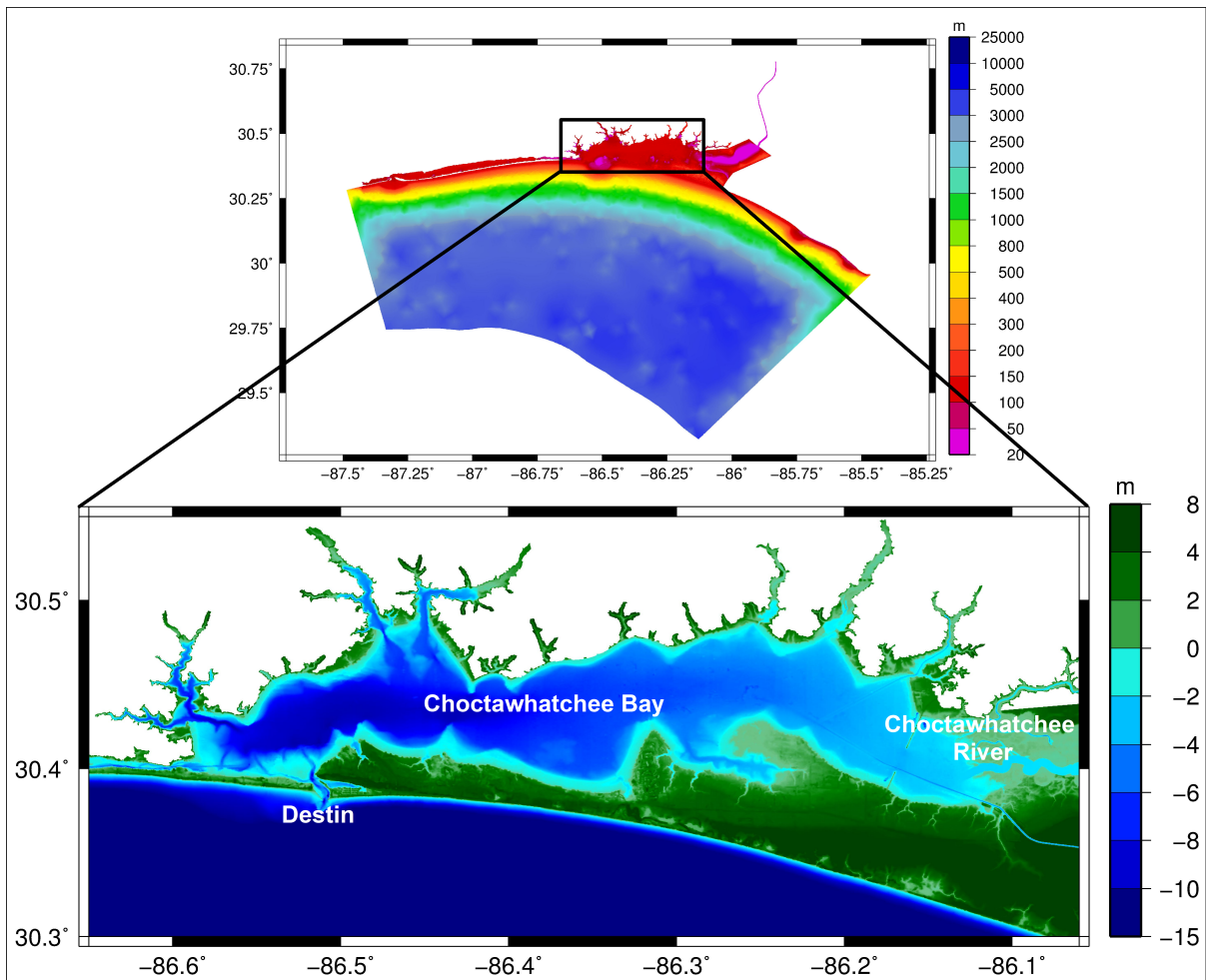


Figure 3.1 Unstructured ADCIRC mesh used in the present study. Top panel shows contours of element spacing. Bottom panel shows the bathymetry and topography contours values in the Choctawhatchee Bay.

3.3 Methods

3.3.1 3D Hydrodynamic Model

The prediction of circulation within the Choctawhatchee Bay system must represent the interactions between components driven by tides, winds, and density gradients, as well as their interactions with the complex coastline, bay, and river. The ADvanced CIRCulation (ADCIRC) model is a finite-element, hydrodynamic model that is widely used for tidal and storm surge studies (Luettich et al., 1992; Westerink et al., 2008). It represents the coastal environment via unstructured meshes that can consist of millions of triangular finite elements of varying sizes to describe variations in open water, in the nearshore, and overland. ADCIRC has achieved prominence for predictions of storm surge and coastal flooding (Bunya et al., 2010; Dietrich et al., 2010; Dietrich et al., 2011a; Blanton et al., 2012b; Lin et al., 2012; Atkinson et al., 2013; Bhaskaran et al., 2013; Murty et al., 2014; Passeri et al., 2015; Bilskie et al., 2016), via the use of its depth-averaged, barotropic version. This study will utilize its fully three-dimensional, baroclinic version to predict the plume dynamics near Choctawhatchee Bay.

Previous studies have validated the baroclinic abilities of ADCIRC through idealistic and realistic applications. The former includes the lock exchange or dam break test, in which waters of different densities initially separated by a vertical barrier are allowed to mix, which is representative of the mixing processes that occur frequently in the coastal ocean, such as that of a fresh- water river emptying into a salt water estuary. ADCIRC was able to provide reasonable predictions for the location, thickness, speed and mixing width of the density front for a laboratory lock exchange test (Kolar et al., 2009). Other studies have demonstrated ADCIRC's ability to predict density-driven flows in regions of shallow bathymetry, such as bays, marshes, and channels adjacent to complicated coastlines that may be under-represented in structured global or regional circulation models. One such study involved modeling the two-layer stratified flow conditions in the Turkish Dardanelles Strait that connects the Aegean Sea to the Marmara Sea and the evolution of the Dardanelles Plume (Blain et al., 2009). Open ocean boundary conditions for the ADCIRC model were derived through one- way coupling with a regional HYbrid Coordinate Ocean Model (HYCOM). The coupled ADCIRC-HYCOM model predicted the behavior of the Dardanelles outflow into the Aegean Sea when forced with accurate initial conditions for stratification in the Dardanelles Strait. In another study, a coastal

forecast system designed to predict ocean currents near the entrance of Chesapeake Bay was tested with baroclinic ADCIRC as its core circulation model (Blain et al., 2012). Baroclinic ADCIRC was also validated for a larger study area in the NGOM that extended along the Texas, Louisiana, Mississippi, Alabama and Florida coasts (Dresback et al., 2010). The salinity and heat transport predicted by ADCIRC over the model domain, which represented the Mississippi and Louisiana coastal waters in detail, were found to match model results from a structured Gulf of Mexico HYCOM model. In all of these studies, HYCOM represented the coastlines with a typical resolution of 4 km, while ADCIRC’s unstructured meshes had maximum resolutions of 50 m, thus allowing a better representation of coastal dynamics.

Recent improvements have advanced ADCIRC’s ability to predict basin-wide density-driven flows involving multiple spatial scales and steep bathymetric gradients (Fathi et al., 2017), b) using a biharmonic operator (Holland, 1978; Zhang et al., 2008) for the viscosity and diffusion coefficients of the momentum and transport equations instead of a Laplacian scheme, which is known to be overly diffusive when multiple spatial scales are involved, c) adaptive filtering of the velocity at every time step based on a weighted average of the velocity at neighboring nodes to smooth noisy oscillations (Asselin, 1972; Shapiro, 1970), and d) systematic bathymetry smoothing to prevent numerical instability (Barnier et al., 1998; Sikiric et al., 2009).

With these improvements, ADCIRC was successfully applied as a three-dimensional, Gulf-wide baroclinic model to predict conditions in the Gulf for June 2010, during the Deepwater Horizon oil spill event. The model sea surface velocities captured the Loop Current in the Gulf. The sea surface velocities, salinities, and temperatures predicted by ADCIRC were in good agreement with model results from the data-assimilated HYCOM model (Fathi et al., 2017). In the present work, we build on these recent improvements and successfully apply ADCIRC to represent the three dimensional transport and mixing of riverine freshwater in the vicinity of the coastline.

3.3.1.1 Mathematical Formulation

3.3.1.2 Three dimensional shallow water equations

ADCIRC solves the three-dimensional, shallow water momentum equations listed below, which are derived from the Navier-Stokes equations after applying the Boussinesq and hydrostatic approximation (Luettich et al., 1992; Luettich et al., 2004; Fathi et al., 2017).

$$\begin{aligned}\frac{\partial u}{\partial t} + u\frac{\partial u}{\partial x} + v\frac{\partial u}{\partial y} + w\frac{\partial u}{\partial z} - fv &= -g\frac{\partial[(\zeta + p_s/g\rho_0 - \alpha\eta)]}{\partial x} + \frac{\partial}{\partial z}\left(\frac{\tau_{zx}}{\rho_0}\right) - b_x + m_x \\ \frac{\partial v}{\partial t} + u\frac{\partial v}{\partial x} + v\frac{\partial v}{\partial y} + w\frac{\partial v}{\partial z} + fu &= -g\frac{\partial[(\zeta + p_s/g\rho_0 - \alpha\eta)]}{\partial y} + \frac{\partial}{\partial z}\left(\frac{\tau_{zy}}{\rho_0}\right) - b_y + m_y\end{aligned}$$

where:

$$\begin{aligned}\frac{\tau_{zy}}{\rho_0} &= E_z \frac{\partial u}{\partial z}; & \frac{\tau_{zy}}{\rho_0} &= E_z \frac{\partial u}{\partial z}; \\ b_x &= \frac{g}{\rho_0} \frac{\partial}{\partial x} \int_z^\zeta \rho \, dz; & b_y &= \frac{g}{\rho_0} \frac{\partial}{\partial y} \int_z^\zeta \rho \, dz; \\ m_x &= -E_h \nabla^2 \nabla^2 u; & m_y &= -E_h \nabla^2 \nabla^2 v;\end{aligned}$$

$$\begin{aligned}E_h &= \frac{L^5}{8\pi^3} \sqrt{\Lambda^6 |\nabla\omega|^2 + \Lambda_d^6 |\nabla\nabla \cdot u_h|^2} \\ |\nabla\omega| &= \sqrt{\left[\frac{\partial}{\partial x} \left(\frac{\partial v}{\partial x} - \frac{\partial u}{\partial y} \right) \right]^2 + \left[\frac{\partial}{\partial y} \left(\frac{\partial v}{\partial x} - \frac{\partial u}{\partial y} \right) \right]^2}, \\ |\nabla\nabla \cdot u_h| &= \sqrt{\left[\frac{\partial}{\partial x} \left(\frac{\partial u}{\partial x} + \frac{\partial v}{\partial y} \right) \right]^2 + \left[\frac{\partial}{\partial y} \left(\frac{\partial u}{\partial x} + \frac{\partial v}{\partial y} \right) \right]^2}.\end{aligned}$$

in which t is time; ζ is the free surface elevation relative to the geoid; u , v , w are velocity components in the x , y , and z coordinate directions, respectively; g is the gravitational acceleration; f is the Coriolis effect; p_s is the atmospheric pressure at the free surface; η is the Newtonian equilibrium tide potential; α is the effective Earth elasticity factor; ρ_0 is the reference density of water; E_z is the vertical eddy viscosity; m_x and m_y are the horizontal diffusion terms; b_x and b_y terms are the baroclinic pressure gradient terms; E_h is the modified Leith biharmonic horizontal viscosity (Fox-Kemper et al., 2013); L denotes local grid spacing; and Λ and Λ_d are non-dimensional coefficients of $\mathcal{O}(1)$.

ADCIRC uses a terrain-following, generalized σ -coordinate system to solve the above

equations. This involves mapping $(x, y, z, t) \mapsto (x_\sigma, y_\sigma, \sigma, t_\sigma)$ such that:

$$\begin{aligned}x_\sigma &= x, \\y_\sigma &= y, \\ \sigma &= a + \frac{a-b}{H}(z - \zeta) \\t_\sigma &= t.\end{aligned}$$

where $a = 1$ and $b = -1$ are constants, $H = \zeta + h$ is the total water depth, and h is the bathymetric depth relative to the geoid. To minimize inaccuracies in regions of steep bathymetry, this transformation is not applied for the baroclinic pressure gradient terms b_x and b_y , and the horizontal diffusion terms m_x and m_y (Dresback et al., 2002; Fathi et al., 2017), which are computed in a z -coordinate system. A Mellor-Yamada level 2.5 turbulence closure model is adopted to compute vertical eddy viscosity and diffusivity. The minimum value for vertical eddy diffusivity is set to be spatially variable.

3.3.1.3 Transport Equation

The time-dependent scalar transport of salinity and temperature is modeled by the following advection-diffusion equation:

$$\frac{\partial c}{\partial t} + u \frac{\partial c}{\partial x} + v \frac{\partial c}{\partial y} + w \frac{\partial c}{\partial z} - \mathcal{D}_h(c, N_h) - \mathcal{D}_v(c, N_v) = 0,$$

where c represents the species that is being transported (i.e., salinity or temperature), $\mathcal{D}_h(c, N_h)$ is the biharmonic horizontal diffusion term, and $\mathcal{D}_v(c, N_v)$ is the vertical diffusion term. Sigma coordinate transformation is applied to all the terms in the transport equation except for the horizontal diffusion term, which is computed in a z -coordinate system. The modeled temperature and salinity are then used by ADCIRC to compute the density field according to the equation of state described by McDougall et al. (2003).

3.3.2 Unstructured Mesh

The unstructured, finite-element, shelf-scale mesh used in the present study (Figure 3.1) is derived from an existing larger Gulf- and Atlantic- wide ADCIRC mesh, which has been validated for tides and storm surge predictions for the coastal regions of Northwest

Florida and Alabama (UCF, 2011a; UCF, 2011b; Passeri et al., 2015; Bilskie et al., 2016).

3.3.2.1 Adjustments for Choctawhatchee Bay Region

The existing mesh was modified for this study by increasing resolution at the inlet and in the open ocean, adding the Choctawhatchee River, and cutting out a shelf-scale mesh with an offshore boundary located along the 200 m depth contour. Floodplains up to the 3 m contour are maintained around the Choctawhatchee Bay and River. The Choctawhatchee River enters the bay at the east end of the bay. The river’s realistic profile is traced from satellite imagery up to the USGS gage at Bruce, Florida. Beyond Bruce, the river is given a simplified ‘synthetic’ profile, which is devoid of all the irregularities and twists and turns of the real river. The upstream river boundary is located at the USGS gage at Caryville, Florida. River bed elevations were derived from FIS study reports for Walton County (Federal Emergency Management Agency, 2008; Federal Emergency Management Agency, 2010). Mesh resolution varies from approximately 20 – 30 m at Destin Inlet and Choctawhatchee River, to approximately 100 – 500 m in the Choctawhatchee Bay, to 1 – 3 km in the shelf (Figure 3.1).

3.3.2.2 Bathymetry Smoothing

Insufficient resolution at regions of steep bathymetric gradients in the ocean can cause inaccuracies and lead to numerical instability (Haney, 1991). To minimize these errors, models can smooth bathymetry (Adcroft et al., 2016; Marshall et al., 1997). The present study uses the bathymetry smoothing approach implemented by Fathi et al. (2017) and applies it to smooth all regions in the mesh deeper than the 15 m contour. The smoothing utilizes common strategies such as limiting the relative variation of the ocean depth over a grid element (Barnier et al., 1998):

$$\max r x_0 = \frac{|h_i - h_j|}{h_i + h_j} \leq 0.2,$$

and also limiting the hydrostatic inconsistency (Haney) number (Sikiric et al., 2009):

$$\max r x_1 = \frac{|h_i^k - h_j^k + h_i^{k-1} - h_j^{k-1}|}{h_i^k + h_j^k - h_i^{k-1} - h_j^{k-1}} \leq 3 \sim 6,$$

where h_i and h_j denote bathymetry at adjacent grid nodes i and j , respectively, and h_i^k

is the depth of the k^{th} σ -layer from the top surface. To eliminate noisy features that may arise after applying the above criteria, a Gaussian filter is also applied to the mesh bathymetry.

3.3.3 Physical Forcings

The ADCIRC model for the Choctawhatchee Bay and River system requires initial and boundary conditions for winds, tides, river discharge, surface heat fluxes, salinities and temperatures.

3.3.3.1 Winds, Tides, and River Discharge

Tidal forcing is applied in the model through open ocean boundary conditions and via the tidal potential term and consists of seven harmonic constituents: K_1 , O_1 , Q_1 , M_2 , S_2 , N_2 and K_2 . The applied winds and surface pressures are from the North American Mesoscale (NAM) model, which is run by the National Centers for Environmental Prediction (<http://www.ncep.noaa.gov/>) four times a day at a spatial resolution of about 12 km. NAM winds show good agreement with the measured wind speeds and directions at the NOAA Penscola station (Figure 3.2). The upstream river boundary of the synthetic channel is forced with a discharge of $150 \text{ m}^3/\text{s}$, which was the observed river discharge during SCOPE (Roth et al., 2017).

3.3.3.2 Salinities, Temperatures, and Heat Fluxes

The open ocean boundaries are forced by vertical salinities and temperatures extracted from HYCOM output (Dresback et al., 2010). HYCOM is a data assimilated, global circulation model that is run operationally by the Naval Research Laboratory for the Gulf of Mexico at a resolution of 1/12 degrees. For the present study, initial conditions for salinities and temperatures are derived from publicly available HYCOM output (http://tds.hycom.org/thredds/dodsC/GOM10.04/expt_31.0/2013/hrly.html) for most of the model domain. HYCOM utilizes a structured grid that does not extend far into inland regions. Therefore, to initialize estuarine conditions, we relied on vertically-varying salinity and temperature profiles provided by the Choctawhatchee Basin Alliance (CBA) (<http://www.basinalliance.org/>). HYCOM output and CBA measurements were combined in the following manner. First, HYCOM output is interpolated onto AD-

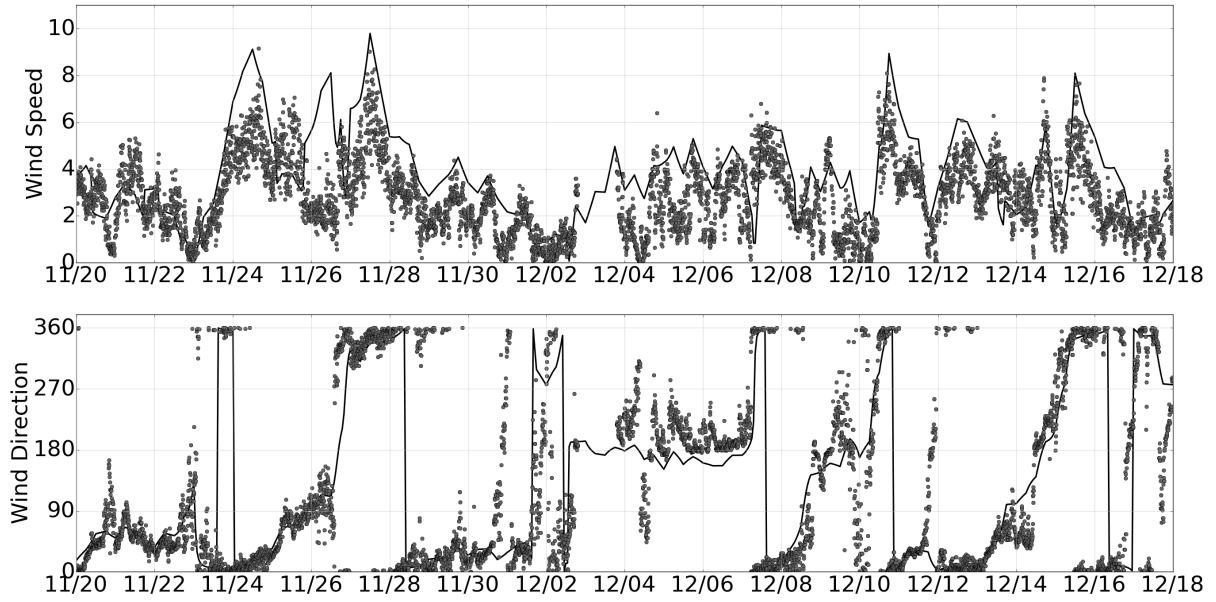


Figure 3.2 Wind speeds (top panel, in m/s) and directions (bottom panel, in degrees clockwise from North) from November 20, 2013 - December 17, 2013 at Pensacola, FL. Grey circles denote observations at NOAA station (ID: 8729840) and black line denotes model forcing.

CIRC mesh vertices that fall within the HYCOM domain. This initializes all the offshore regions of the ADCIRC mesh. ADCIRC mesh vertices that coincide with CBA measurement locations are then seeded with the measured vertical profiles. This is followed by extrapolation outward from the near-shore and offshore ADCIRC mesh vertices that are already initialized. The “final” near-shore initial conditions reflect a gradual transition from the interpolated offshore HYCOM salinities to measured values inside the bay.

3.3.4 Model Setup

The simulation period spans the months of November–December 2013 to match the timing of the SCOPE experiment. The model is forced by realistic tides, winds, riverine freshwater discharge, and surface heat flux values for this period. Model runs have a diagnostic phase of 5 days (1-6 November 2013) followed by the prognostic phase through 16 December. In the diagnostic phase, the transport of salinity and temperature is disabled and thus the density field is constant, while tides, winds and river inflow are allowed to spin up (Dresback et al., 2010). Salinities and temperatures are allowed to evolve at the beginning of the prognostic phase, and density gradients begin to drive the

flow conditions. The model was run for a 45-day simulation with 21 vertical layers at a time step of 0.5 sec.

3.4 Model Validation

A series of experiments collectively referred to as the Surfzone Coastal Oil Pathways Experiment (SCOPE, <http://carthe.org/scope/>) were performed near Destin by scientists from the Consortium for Advanced Research on Transport of Hydrocarbon in the Environment (CARTHE, <http://carthe.org/>). Field observations were collected during SCOPE to identify processes that influence surface transport in the inner shelf, which need to be better understood to improve future predictions of nearshore oil transport pathways in the event of an oil spill. During a 2 week period between 3-17 December 2013, data were collected with GPS-equipped surface drifters, helicopters, drones, balloons/kites, jet skis, small boats, ADCPs, CTD casts, and dye releases to describe nearshore wave and current movements (Valle-Levinson et al., 2015; Huguenard et al., 2016; Roth, 2016; “Along-shelf Currents Forced by Crossshore Winds in the Inner Shelf of the Northeastern Gulf of Mexico”; Roth et al., 2017). In this section model results are validated by comparisons against SCOPE data including in-situ observations for water levels and vertical salinities, observed drifter movement and satellite imagery.

3.4.1 Water Levels

Model water levels are compared against observations (96 hr high pass filtered to remove low-frequency oscillations) collected at four locations: Panama City Beach (NOAA station 8729210), Panama City (NOAA station 8729108), SCOPE moored pressure sensor located at 10 m depth off the coast of Beasley Park about 6 to 7 km west of Destin Inlet, and SCOPE pressure sensor at the Mid-Bay Bridge in Choctawhatchee Bay (Figure 3.3). Overall, observed and modeled water levels are in good agreement, with ADCIRC sometimes underestimating the observed water levels by 0.1 to 0.2 m. There is a slight phase difference between observed and measured water levels at Panama City Beach, likely because the ADCIRC mesh does not extend into the estuary where the NOAA gage is situated. Tidal amplitudes inside Choctawhatchee Bay are attenuated to roughly 30% of the amplitudes at the shelf with a phase delay of 5.5 hours, thus matching the observed behavior (Valle-Levinson et al., 2015).

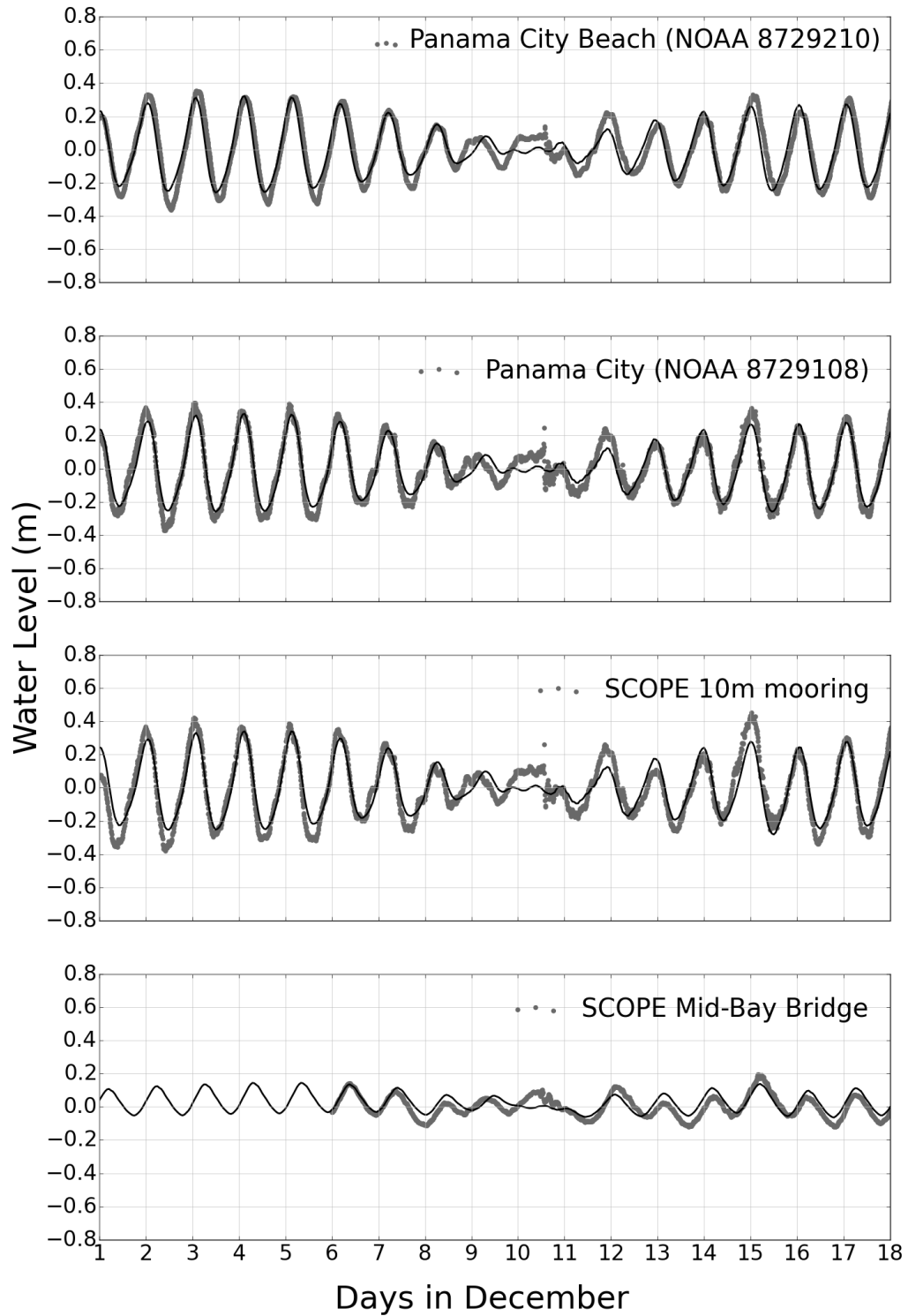


Figure 3.3 Comparison of observed and modeled water levels. Grey circles denote observations and solid line denotes ADCIRC water levels.

3.4.2 Vertical Salinities

The model's ability to represent the vertical salinity distribution inside the Choctawhatchee Bay and on the shelf were quantified by computing standard error statistics (Wilkin et al., 2013). The error metrics in this study include the Pearson correlation coefficient (r):

$$r = \frac{\frac{1}{N} \sum_{i=1}^N ((o - \langle o \rangle)(m - \langle m \rangle))}{\sigma_m \sigma_o}$$

the centered root mean square error (E_{CRMS}):

$$E_{CRMS} = \sqrt{\frac{1}{N} \sum_{i=1}^N ((m - \langle m \rangle) - (o - \langle o \rangle))^2}$$

and the mean bias (B_M):

$$B_M = \langle m \rangle - \langle o \rangle$$

in which o is a set of observed values of size N ; m is a set of model predictions; $\langle m \rangle$ and $\langle o \rangle$ are the means of m and o , respectively; and σ_m and σ_o are the standard deviations of m and o , respectively.

Each metric has its own strengths and limitations in describing model performance. Therefore, it is prudent to use a suite of metrics to avoid an incomplete or limited description of model skill (Koh et al., 2012). The correlation coefficient r is a statistical measure of whether the model and observed salinities are related linearly, and it varies from 1 (for perfectly negatively correlated), through 0 (for uncorrelated), to +1 (for perfectly positively correlated). Therefore it quantifies the model's ability to capture the pattern of vertical variability in the measured salinity data. However, it does not provide any information about the amplitude of variability, which is quantified by the standard deviation (σ_m , σ_o). The root mean square error is another widely-used estimate of the differences in magnitude between model and observed quantities. It can be resolved into two components, namely differences between the means (mean bias B_M) and the differences in their patterns of variation (centered root mean square error E_{CRMS}) (Taylor, 2011). The mean bias B_M is a measure of the overall systematic differences between the model and observed salinities and therefore can quantify whether the model is "too high"

or “too low.” Centered root mean square error compares model and observed quantities after removing any bias associated with their mean values. The E_{CRMS} approaches zero as the modeled and measured profiles become identical. However, a given value of E_{CRMS} can be biased by the amplitude of variations from mean, and thus can be larger when there is a larger variability in the observed profile.

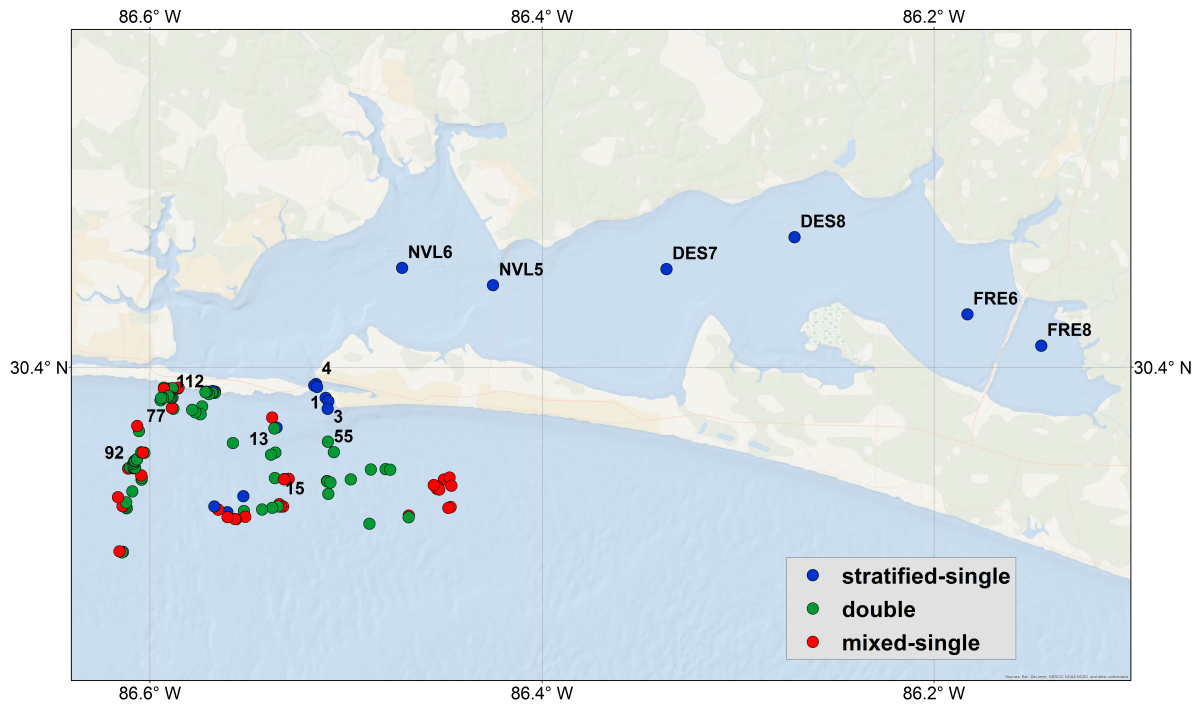


Figure 3.4 Locations in the bay, inlet and shelf waters where vertical salinity (circles) and water level observations (asterisks) are available.

Model salinities are compared against observed vertical salinities at 121 stations, collected between 3-17 December 2013, in the Choctawhatchee Bay and adjacent shelf waters (Figure 3.4). These observations show three types of salinity profiles. Observations collected by the Choctawhatchee Basin Alliance inside the bay indicate stratified conditions. In the central and western portions of the bay, observed salinities range from 15 to 20 psu at the surface to about 30 psu at the bottom. Model salinities represent

well this large variability in the vertical profile (Figure 3.5). At the eastern end, where Choctawhatchee River drains into the bay, the water column is relatively shallow (about 3 m depth) and highly stratified, with a difference of 15 to 20 psu between surface and bottom salinities. Although model salinities also indicate a large difference between surface and bottom salinities (15 psu) they predict well-mixed conditions below the surface layer. Outside the estuary and onto the shelf, the water column is observed to be either well-mixed (see salinity profiles at CTD 15, CTD 92 and CTD 77 in Figure 3.6) or has an upper stratified layer and a lower mixed layer (see salinity profiles at CTD 13, CTD 55 and CTD 112 in Figure 3.6). Brackish conditions in the surface at the stations located on the shelf indicate the effects of the surface ebb phase outflow from Destin Inlet.

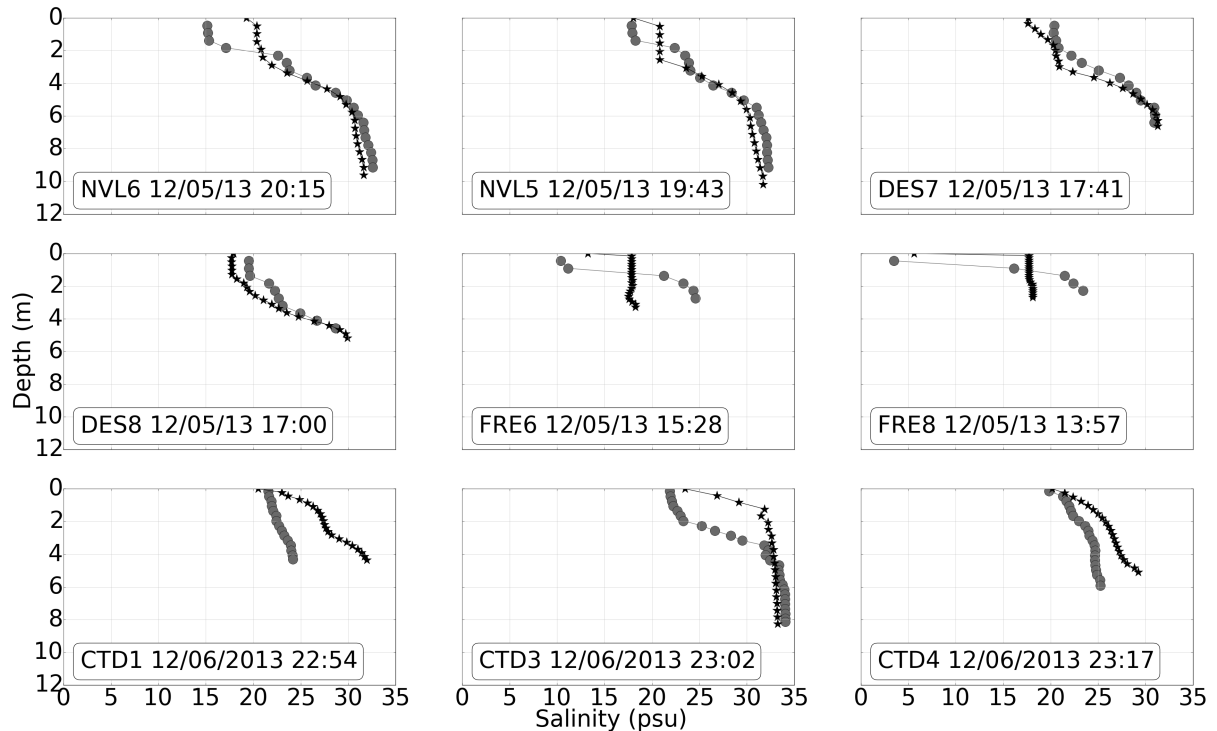


Figure 3.5 Comparisons of observed (grey circles) and modeled (black asterisks) vertical salinities inside Choctawhatchee Bay (top two panels) and within Destin Inlet (bottom panel).

To characterize their differing geographical location and circulation features, the observed salinity profiles are grouped into three main categories: highly stratified conditions (“single-stratified”), in which the salinities vary through the entire water column; par-

tially stratified conditions (“double”), in which the salinities vary only in an upper layer and are relatively constant in a lower layer; and well-mixed conditions (“single-mixed”), in which the salinities are relatively constant through the entire water column. The “single-stratified” profiles are located typically in shallow waters and in the bay; the “double” profiles are located typically on the shelf near the inlet; and the “single-mixed” profiles are located typically on the shelf far from the inlet. Taken together, these observations provide a comprehensive description of the spatial and temporal variability in the salinity characteristics of the water column in the study area. For “double” profiles, error statistics are computed separately for the upper stratified layer (called “double-stratified”) and the lower mixed layer (called “double-mixed”). For “single-stratified” and “double-stratified” profiles, the model should represent accurately the vertical salinity variability, and thus r is used to quantify this variability.

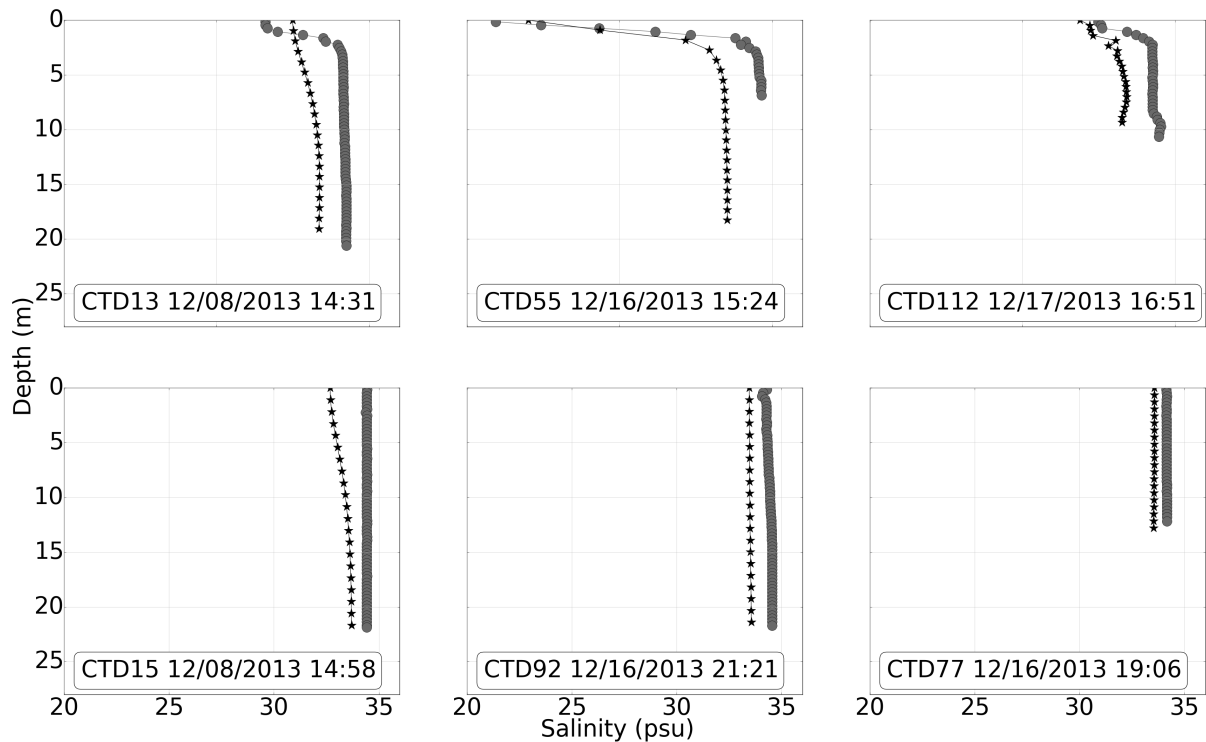


Figure 3.6 Comparisons of observed (grey circles) and modeled (black asterisks) vertical salinities in the shelf waters adjacent to Choctawhatchee Bay.

The error metrics are computed to quantify model performance. We first discuss the error statistics at selected stations (Table 3.1), which are chosen to be representative of the features of the three categories. At stations DES7, CTD1, and CTD5, (Figure 3.5) which are located in the estuary, inlet and inner shelf respectively, the r values are 0.980, 0.960 and 0.802, respectively, signifying a high degree of correspondence between model and observed profiles. Similarly, r can be used to evaluate the model’s ability to capture the rapid change in salinities in the “double-stratified” profiles located in the shelf waters. At stations CTD13, CTD 55 and CTD 112, (Figure 3.6) the salinities increase rapidly (2 to 8 psu) within the top 0 to 2.5 m of the water column (3.6). Model and observed salinities in this upper layer are in a good agreement with $r > 0.8$.

The variability in observed salinities can be quantified by the standard deviation, which is very small (less than 0.1 psu) for “double-mixed” and “single-mixed” profiles), signifying a well-mixed water column. Due to this absence of vertical variation, it is meaningful to compare overall differences between modeled and observed salinities, rather than quantifying the degree to which the model can replicate patterns in the observed salinity profile. Therefore, B_M and E_{CRMS} are more appropriate metrics for these profiles. The standard deviation of vertical salinities in the bottom mixed layer at stations CTD 13, CTD 55 and CTD 112 is about 0.05 psu, which indicates almost zero vertical variability. Model salinities are in good agreement with observed mixed-layer salinities at these stations with E_{CRMS} less than ± 0.2 psu and B_M of ± 1 psu. The water column is well-mixed over its entire depth with measured salinities of 34 psu at CTD 15, CTD 92 and CTD 77.

Error metrics are computed at all the 121 stations by considering separately the model performance in the stratified and well-mixed portions of the water column (Figure 3.7). The water column is observed to be highly-stratified within the estuary, partially stratified in the shelf waters near the inlet and fully mixed with an oceanic salinity of 34 psu several kilometers away from the inlet. Stratified conditions within the bay and in the upper layers of the shelf waters are well represented by the model with a high degree of correlation with the observations ($r > 0.5$). The B_M and E_{CRMS} , which are computed for the stratified water column, are largest for stations within the estuary where the water column is highly stratified (σ_o between 4 to 6). However, the variability in vertical salinities is captured very well by the model with a high degree of correlation ($r > 0.9$) at these locations. As we move further away from the inlet, the effects of the ebb-phase

Table 3.1 Error statistics at selected stations.

Station Name	Type	B_M	E_{CRMS}	r	σ_m	σ_o
DES7	single-stratified	-1.193	1.116	0.980	4.816	4.157
CTD1	single-stratified	4.957	1.847	0.960	2.707	0.915
CTD5	single-stratified	3.686	1.078	0.802	1.765	1.190
CTD13	double-stratified	0.138	0.791	0.977	0.031	0.821
	double-mixed	-1.002	0.183	0.899	0.232	0.057
CTD55	double-stratified	-0.908	1.175	0.981	1.877	2.957
	double-mixed	-1.295	0.093	0.955	0.146	0.057
CTD112	double-stratified	-0.851	0.440	0.811	0.214	0.595
	double-mixed	-1.015	0.146	0.237	0.149	0.049
CTD15	single-mixed	-1.09	0.348	-0.08	0.347	0.007
CTD92	single-mixed	-0.935	0.096	0.845	0.03	0.12
CTD77	single-mixed	-0.597	0.015	-0.803	0.008	0.008

river plume are minimized and the water column is observed to be well mixed. The model provides an accurate representation of the well-mixed water column with the B_M being less than 0.5 psu and E_{CRMS} being less than 0.5 psu at these stations. Overall, these statistics indicate that ADCIRC is able to represent well the salinity characteristics in the study area, including the transition from brackish waters in the bay to saline waters on the shelf.

3.4.3 Comparisons to Satellite Imagery

In Synthetic Aperture Radar (SAR) images, the convergence zones associated with river plumes are visible as narrow, bright features, and therefore these images are widely used to identify plume footprints (Zheng et al., 2004; Nash et al., 2005; Jiayi et al., 2006; Huguenard et al., 2016). SAR images collected during SCOPE, utilizing VV polarization in Stripmap mode with a spatial resolution of 5 m, indicate a distinct ebb-phase river plume at Destin Inlet (Huguenard et al., 2016). Based on the approach followed in previous studies (Androulidakis et al., 2011; Pan et al., 2014; Xia et al., 2011), we use the 33-psu salinity contour to identify the cross-shore extent of the model plume. It is noted that coastal models are known to underestimate the spreading of a river plume due to limitations in representing the fine-scale turbulent processes that occur at the plume front (Huguenard et al., 2016). Here, we adopt a qualitative approach to investigate model

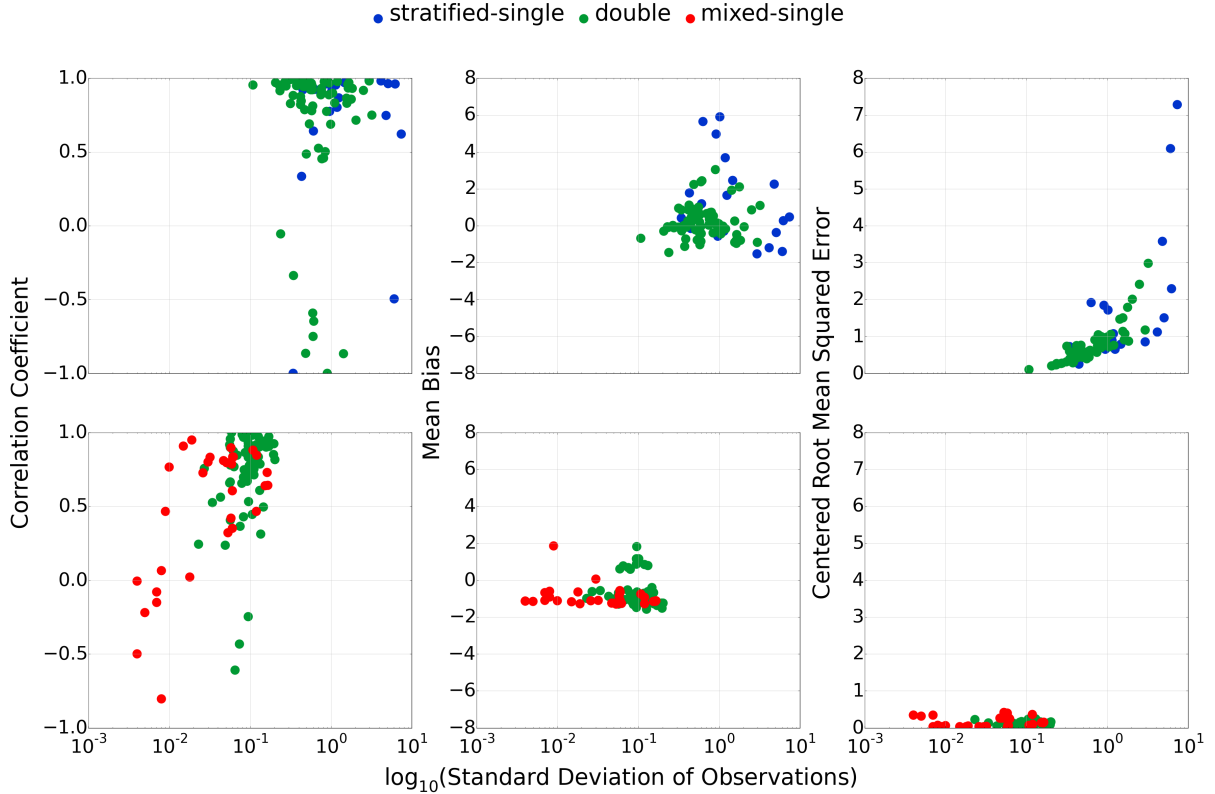


Figure 3.7 Error statistics (from left to right - correlation coefficient, mean bias and centered root mean squared error) computed for model salinities. Top row corresponds to model skill in stratified conditions. Bottom row corresponds to model skill in well mixed conditions. Blue, green and red circles represent “stratified-single”, “double” and “mixed-single” conditions respectively.

skill in predicting the plume geometry. Overall, the model and observed plume footprints are in good agreement with the cross-shore extent of the plume being underestimated by roughly 1.5 to 2 km in the model (see the red lines vs the plume extents in Figure 3.8).

Model salinities (33-psu salinity contour) during the ebb phase on 3-4 December reveal that, under the influence of weak southerly winds (2 to 4 m/s), the model plume spreads radially onto the shelf and along the coastline. The plume cross-shore extents are roughly 6 km and 4.4 km in the satellite and model plumes, respectively, on 3 December. On 4 December both the model and satellite plume have a similar cross-shore extent of 5 km. The winds continue to be weak and southerly on 5 December. The model and the satellite plume show a preferential expansion towards the west and have a similar cross-shore extent (5 km). The ebb-phase plume is more restricted to the coastline on

9 December, in the SAR imagery, when the tides are the weakest in the month (neap tides) and the prevailing winds are southeasterly. During this time, the model plume has a slightly larger cross-shore extent (4.2 km) than the satellite plume (3.6 km). On 13 December, winds with moderate wind speeds (6 – to 8 m/s) blow predominantly from the north and enhance the offshore spreading of the plume. The 33-psu model salinity contour is located at a distance of 5 km south of the inlet, whereas the maximum cross-shore extent of the plume is roughly 6 km in the satellite image. The model plume, forced by weak northerly winds on 17 December, expands offshore to about 4.37 km south of the inlet, whereas the cross-shore extent of the observed plume is roughly 7 km. These validation results are an indication that ADCIRC can represent the response of the buoyant plume to wind forcing, and they allow for exploratory studies in a following chapter.

3.4.4 Drifter Movement

During SCOPE, drifters were released at the inlet to study surface transport characteristics near the inlet. Here, we use Lagrangian particles as a proxy for SCOPE drifters and advect them by modeled surface currents utilizing an existing particle tracking algorithm (Dietrich et al., 2012b). Particle trajectories are compared with observed drifter pathways to evaluate model skill in representing nearshore plume- and wind-driven surface currents (Figure 3.9, Figure 3.10). SCOPE drifter releases were made at the inlet during the ebb phase of the tidal cycle on 5 December, 8 December and 10 December (Roth et al., 2017). On 5 December, winds are weak and southerly and the drifters first trace an offshore radial bulge as it exits from the inlet before being transported to the west. On 8 December, a moderate easterly component in the prevailing winds force the SCOPE drifters to immediately turn west and proceed along the coast as they exit the inlet. On 10 December, the wind forcing is northerly and moderate and the drifters are advected southward and offshore away from the inlet. As in other studies (Callies et al., 2017; Edwards et al., 2006), it is challenging to represent realistic drifter pathways with model particle trajectories. On 5 December, particles trace a radial bulge and are transported to the west in a manner similar to that observed in the real drifters. However, the modeled currents do not carry the particles as far down coast as is observed in reality. On 8 December, the particles turn west and proceed along the coastline as soon as they exit the inlet, thus matching the observed drifter behavior. However, these particles beach

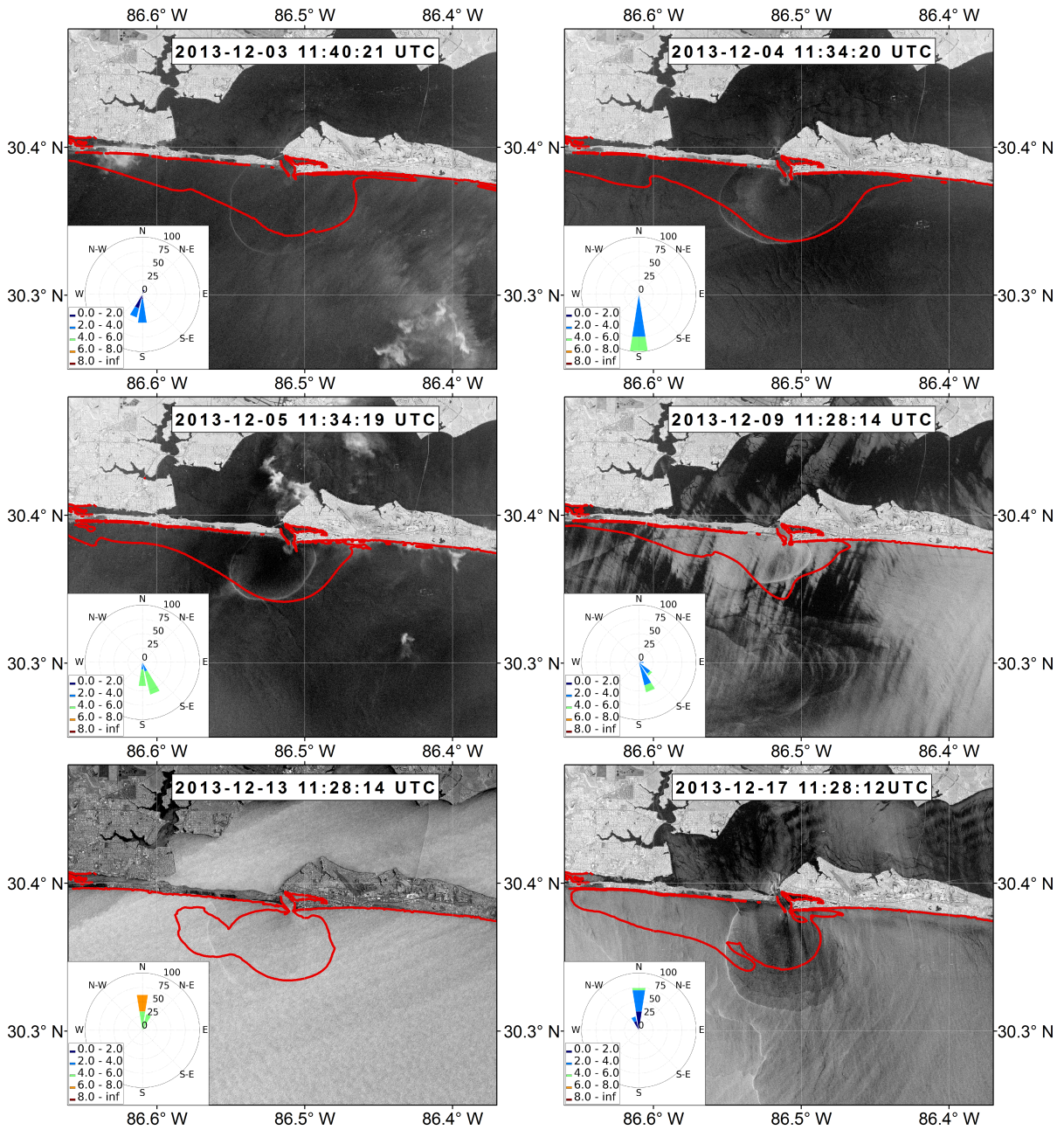


Figure 3.8 Ebb-phase plume footprint at Destin Inlet observed in SAR satellite imagery and represented by the 33 psu model salinity contour (red line). Wind roses represent the wind forcing over the past 24 hours. (COSMO-SkyMedTM Product ©ASI 2013 processed under license from ASI – Agenzia Spaziale Italiana. All rights reserved. Distributed by e-GEOS. Downlinked and processed by CSTARS.)

earlier than the real drifters travel. On 10 December, the particle movement match the observed drifter movement. Just like the real drifters, the particles do not trace a radial bulge or coastal jet in the vicinity of the inlet and are transported far south by the model currents and winds. Overall, particle trajectories are able to reflect changes in the plume response with changing wind conditions as is being described by the observed drifters. However, the model underestimates the strength of the ambient surface shelf currents during the simulation period, and therefore the model particles do not travel as far as the real drifters. Also, the particle tracking method does not take into account windage effects, which may also be causing inaccuracies in the track predictions.

3.5 Summary

A recently-enhanced, three-dimensional, baroclinic version of ADCIRC was applied after minor improvements for high resolution simulations of the mixing and transport of fresh water at the river-estuarine-shelf scale. The model was successfully applied to represent the wind- and density-driven circulation inside Choctawhatchee Bay and adjacent shelf waters during November-December 2013, a period of low river flows. Initial conditions were derived by combining model output from a regional ocean model with near-shore observations. The applied forcings include tides, winds, freshwater inflows and surface heat flux. Model performance was evaluated by comparisons with observed tides, vertical salinity profiles, satellite imagery and observed drifter movement. Although ADCIRC water levels underestimate observed water levels at some stations by 0.1 to 0.2 m, they are overall in good agreement. Salinity behavior in the study area consists of fully-stratified, partially-stratified, and fully-mixed conditions inside the bay, in the inner shelf region near the inlet, and in the shelf waters away from the inlet, respectively. In the stratified portion of the water column, there is a high degree of correlation (> 0.6) between observed and modeled salinity profiles at most locations. The computed error statistics (with E_{CRMS} less than 0.5 and B_M less than 2 psu) also indicate a good match between observed and modeled salinities in regions where the water column is fully mixed. The 33 psu salinity contour is used to mark the model plume signature. Model plume predictions compare well with the visible plume in satellite imagery. Finally, the surface transport of lagrangian particles advected by modeled surface currents are compared against observed drifter movement. The comparisons reveal that model predictions underestimate the

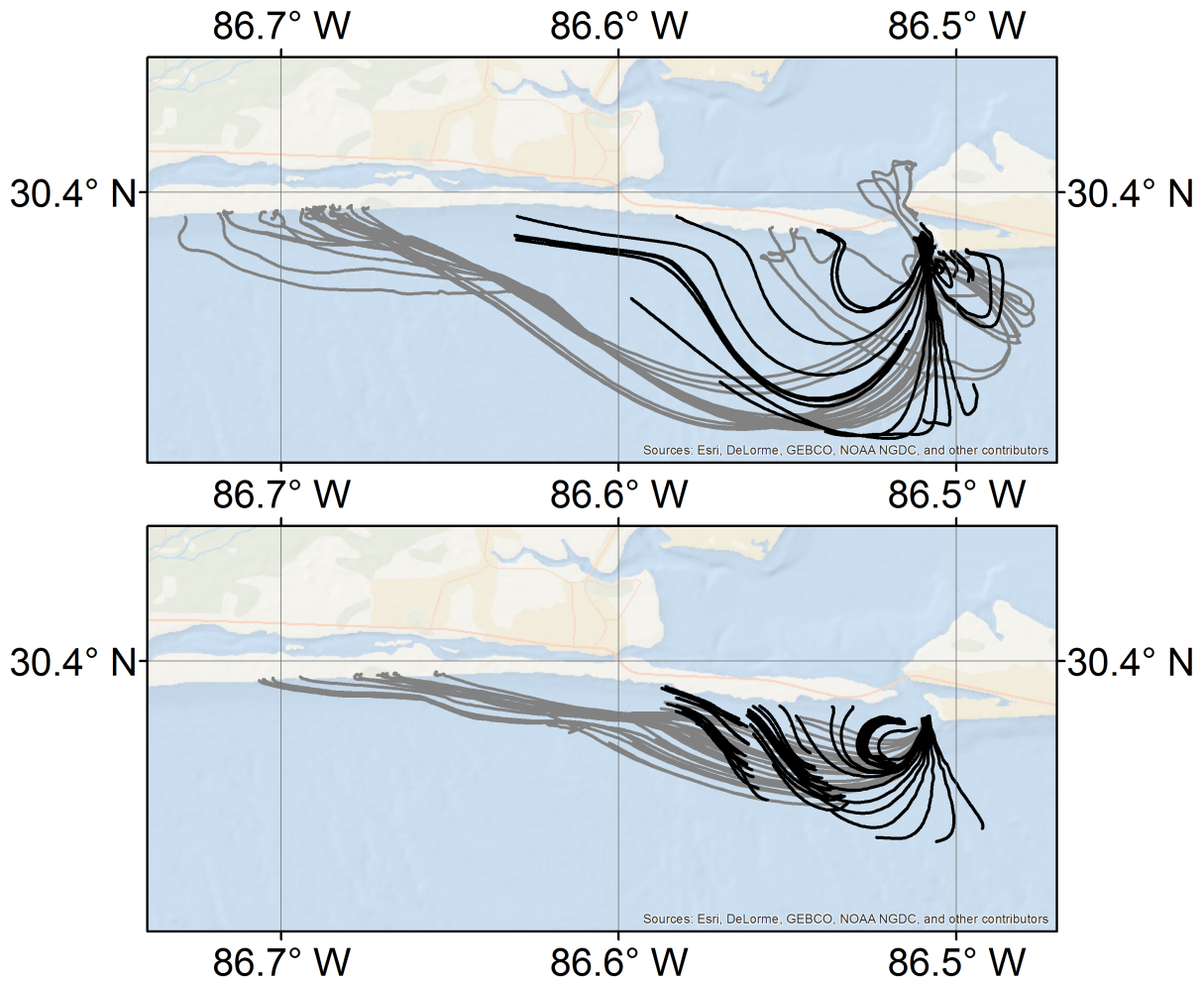


Figure 3.9 Observed drifter movement (grey lines) and trajectories of Lagrangian particles advected by modeled surface currents (black lines). Drifters are released in the inlet during the ebb-phase on 5 December and 8 December.

along-shore currents in the shelf. However, modeled surface currents are able to illustrate key features of the variability in the wind and plume driven shelf currents.

This study marks the first time a recently enhanced baroclinic version of ADCIRC is applied to model estuarine and shelf circulation. Model validation efforts presented here demonstrate ADCIRC's ability to capture the characteristics of salinity transport within the bay and in the shelf. The validation model is now applied in the next chapter to perform exploratory studies that provide new insights about estuarine salinity and plume behavior in the vicinity of Choctawhatchee Bay.

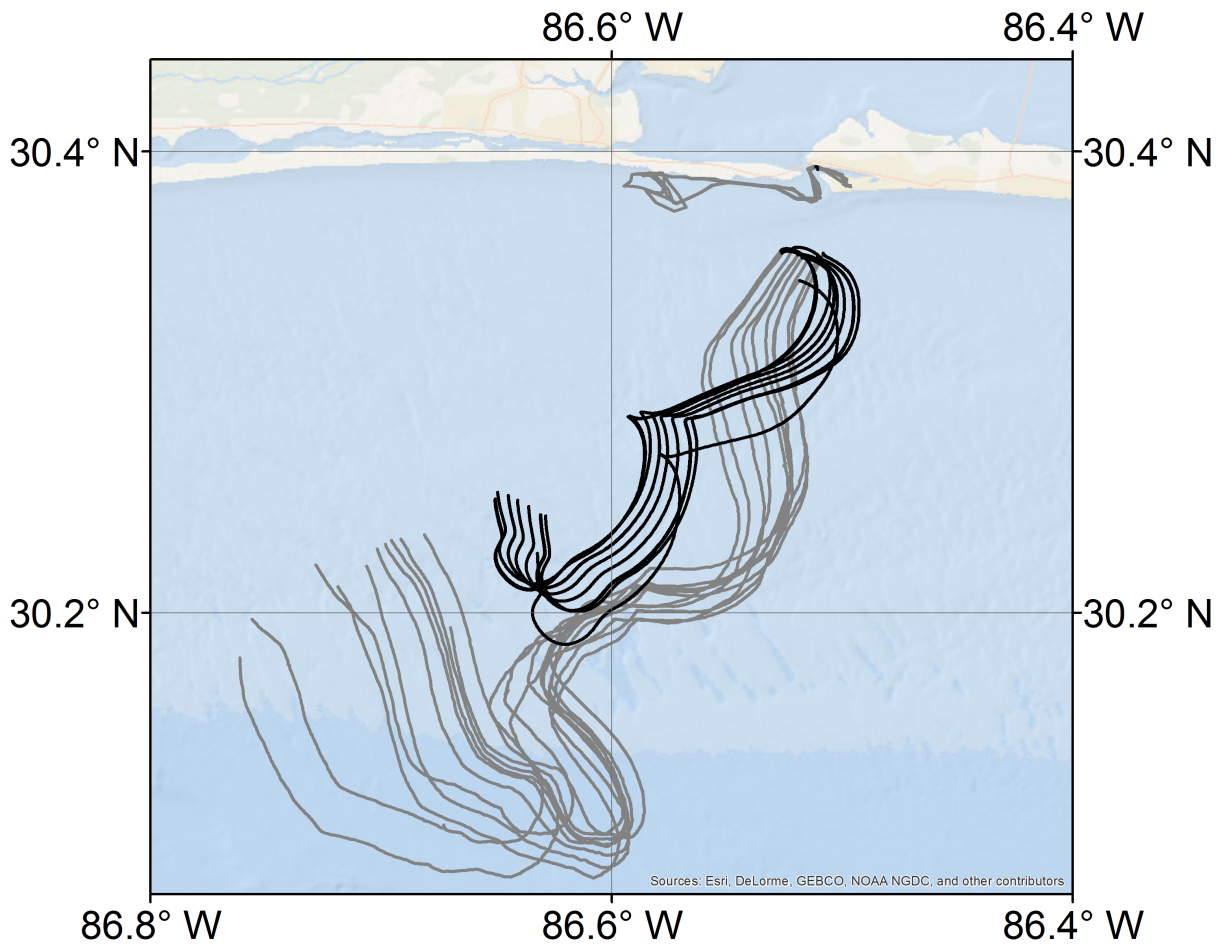


Figure 3.10 Observed drifter movement (grey lines) and trajectories of Lagrangian particles advected by modeled surface currents (black lines) on 10 December.

Chapter 4

Wind and Tide Effects on Salinity Characteristics in Choctawhatchee Bay and the Adjacent Continental Shelf

4.1 Overview

This chapter describes the application of the validated model described in Chapter 3 to perform exploratory studies to understand the characteristics of salinity transport in Choctawhatchee Bay and adjacent shelf waters. The validated model is applied first to investigate the response of the ebb-phase plume at Destin Inlet to changing wind and tidal conditions. In the rest of this chapter, key features of salinity transport in the inlet and within the bay are analyzed using model predictions.

4.2 Introduction

An estuary is defined as “a semi-enclosed coastal body of water, which has free connection to the open sea, extending into the river as far as the limit of tidal influence, and within which sea water is measurably diluted with fresh water derived from land drainage” (Dyer, 1998). Estuaries may differ in their geometrical and physical forcing characteristics, but they are generally expected to have a longitudinal salinity gradient

that ranges from freshwater input at the head of the estuary to saline conditions where the estuary connects to the ocean (Geyer, 2010). The freshwater inflow rate, tidal range, meteorological forcing, and estuarine geometry play important roles in determining the eventual longitudinal, vertical, and lateral salinity profiles within an estuary. The salinity distribution within an estuary is an important water quality and ecological indicator (Huang et al., 2014) and, together with tides and winds, determine circulation patterns within the estuary.

River-dominated estuaries can cause strong density gradients due to the transport and mixing of brackish estuarine outflows in the continental shelf. These density gradients can cause the slowing down and convergence of offshore surface material (Roth et al., 2017) and thus prevent its transport into coastal regions. The interaction of river plumes with the shelf waters can therefore determine the fate and transport of river-borne nutrients, larvae, plankton, chemical and oil spills in the nearshore environment and influence biogeochemical processes in coastal ecosystems (Mestres et al., 2007; Xia et al., 2007; Chant et al., 2008; Shi et al., 2010; Androulidakis et al., 2011; Greer et al., 2018).

Brackish plumes generated by high-discharge river systems with wide mouths have been the subject of numerous observational and numerical studies (e.g., Johnson et al. (2001), Guo et al. (2007), Chant et al. (2008), Ou et al. (2009), Pan et al. (2014), Tarya et al. (2015), and Yu et al. (2018)). However, only limited studies have analyzed the response of small-scale river plumes, such as those formed at the mouths of several bays and estuaries situated in the Northern Gulf of Mexico (NGOM). These river-dominated estuaries have limited connectivity to the NGOM and form small-scale river plumes that introduce cross-shore salinity and velocity gradients in the shelf waters and form density fronts where surface material converges or slows (Roth et al., 2017).

The buoyant plume from Mobile Bay, Alabama, a river-dominated estuarine system with a narrow and shallow connection to the shelf, has been studied via satellite imagery and in-situ observations (Stumpf et al., 1993; Dzwonkowski et al., 2015). The plume was found to be sensitive to wind forcing despite relatively low wind speeds. The shallow nature of the plume made it highly susceptible to wind forcing, with the wind becoming more effective in modifying the plume structure, via weakening of the density gradients as the plume expanded offshore. Downwelling winds caused a westward elongation of the surface-advected plume, and upwelling winds reversed and widened the plume.

Perdido Bay estuary, situated adjacent to Mobile Bay along the Florida-Alabama coast, is another semi-enclosed bay system that interacts with the coastal ocean through a narrow inlet. Model salinities described a larger plume signature in the absence of wind forcing in comparison with the plume response during idealized wind conditions (Xia et al., 2011). In the absence of wind forcing, the plume has a relatively large size that spreads offshore and along the coast in both directions. The plume is farthest offshore for northerly winds and confined closest to the coast and smallest for southerly winds. Like the Mobile Bay plume, the Perdido Bay plume was predicted to extend westward for easterly downwelling-favorable winds and is deflected offshore and eastward for westerly upwelling-favorable winds.

Salinity dynamics within estuaries are influenced by several factors including tidal range, prevailing winds, bay geometry and freshwater flows (Huang et al., 2014; Rayson et al., 2015; Martyr-Koller et al., 2017; Coogan et al., 2018). Estuaries are classified according to their tidal ranges into different categories: micro-tidal (tidal range of 0 – 2 m), meso-tidal (tidal range of 2 – 4 m) and macro-tidal (tidal ranges greater than 4 m) (Davies, 1964). Estuaries are also classified according to the degree of stratification and mixing. In well-mixed estuaries, tidal flows have a stronger influence than freshwater flows and there is strong mixing of fresh and saline water. The reverse occurs in highly stratified estuaries where there is very little mixing between an upper fresh and a bottom saline layer. Strong salinity stratification can lead to conditions that cause hypoxia and affect the survival of aquatic species. Well-mixed estuaries are more common in meso- and macro-tidal environments whereas highly stratified estuaries are more common in micro-tidal environments (Tweedley et al., 2016). However, estuarine systems may exhibit daily, monthly or seasonal and spatial variability in their mixing and stratification patterns (Valle-Levinson, 2010). Periodic stratification and de-stratification can occur in meso- and macro-tidal estuaries with substantial river flows (Wang et al., 2011) and wind- and fresh-water induced vertical mixing can occur in shallow, micro-tidal estuaries.

Many estuaries in the northern Gulf of Mexico, such as Mobile Bay, Perdido Bay, Choctawhatchee Bay etc, are similar: they are shallow and wide, have diurnal tides with a micro-tidal range, are river-dominated and are connected to the Gulf via narrow openings (Coogan et al., 2018; Kim et al., 2012). In Mobile Bay, which is stratified 80% of the time (Noble et al., 1996), down-estuary winds enhances the stratification and up-estuary winds increases the mixing (Coogan et al., 2018). Periods of relatively high discharge

was found to increase stratification in Mobile Bay (Kim et al., 2012). In some estuaries, seasonal increases in freshwater flows can cause the water column to be well-mixed. For eg. in the Swan River Estuary, which is a micro-tidal estuary in south-western Australia, 80% of the fresh water discharge enters the bay between June - October and causes the water column to be fresh from top to bottom (Tweedley et al., 2016). Due to the more pronounced tidal effects, salinities in the middle of meso- and macro-tidal estuaries can change considerably over the course of a tidal cycle. However, mid-bay salinities undergo only small changes during a tidal cycle in micro-tidal environments. However, significant changes can occur in the salinities when there are substantial changes in incoming river flows (Tweedley et al., 2016).

One of the key indicators of estuarine water quality is the rate at which water exchange occurs at the inlet and the residence time of an estuary is computed to quantify this. Macro-tidal estuaries typically have wide mouths, which together with strong tides and river flows lead to efficient flushing and residence times of hours to days. Micro-tidal estuaries, on the other hand, typically have low connectivity to the ocean and therefore undergo limited flushing and may have residence times of the order of weeks or months (Uncles et al., 2002; Tweedley et al., 2016; Warwick et al., 2018).

The focus of the present study is to study characteristics of bay salinities and the behavior of the small-scale river plume from Choctawhatchee Bay, which is a micro-tidal estuary situated to the east of Mobile Bay and Perdido Bay along the Florida Panhandle and connects to the NGOM via the narrow Destin Inlet. Field measurements give us important insights about the wind and plume driven circulation offshore of Destin Inlet (Roth et al., 2017). Moderate winds with an easterly component create a coastal jet, which forms a coastal barrier that prevents offshore drifters from beaching. Plume conditions during light and variable winds also prevent drifter transport to the beach. However, due to limitations associated with a field experiment, the plume- and wind-driven nature of the circulation was observed only on specific days between 3-17 December 2013, and the relative effects of variability in tidal and wind forcing on the plume geometry are unknown. Little is also known about salinity characteristics inside the bay and the most recent comprehensive studies of the bay, dates back to the 1980's (Livingston, 2010).

In this chapter, the validated model described in Chapter 3, which provides a realistic description of the study area and environmental forcing conditions, is applied to address this gap and investigate key features of bay salinities and the flood- and ebb-

phase plume response on consecutive days of variable tidal and wind forcing. Winter cold fronts that pass over the Florida Panhandle are associated with rotary winds that cause considerable variability in the wind forcing over the study area. Changing wind conditions and spring-neap variability in tidal conditions are expected to cause significant differences in the plume response on consecutive days. The validated model is applied to quantify the length and width of the plume signature on consecutive days of near-constant tides and variable wind directions, and on consecutive days of near-constant wind speeds and neap-to-spring variability in the tidal forcing. Variability in longitudinal and vertical salinity gradients inside the bay and residence times within this bay are also computed from model results. This study is unique in two ways. Very few studies have investigated the dynamics of the wind- and plume-driven circulation within and offshore of Choctawhatchee Bay, and this study contributes to the scientific understanding of the characteristics of the Choctawhatchee River Plume and hydrodynamics of Choctawhatchee Bay. Secondly, this is the first time a recently-enhanced, three-dimensional, baroclinic version of the ADvanced CIRCulation (ADCIRC) model (Luettich et al., 1992; Westerink et al., 2008; Fathi et al., 2017), which has been widely applied for depth-averaged tidal and storm surge studies (Bunya et al., 2010; Dietrich et al., 2012b; Cyriac et al., 2018), is applied to study in-depth density-driven estuarine and shelf circulation.

4.3 SCOPE Observations near the Choctawhatchee Bay System

The study area is located in the estuarine and shelf waters in the vicinity of Choctawhatchee Bay, which is aligned in an east-west direction along the Florida Panhandle. Numerous bayous and creeks lining its banks are sources of freshwater for the bay. However, the bay receives 90% of its freshwater input from the Choctawhatchee River (CR) (Handley et al., 2007), which enters the bay at its eastern end. The bay is about 43 km long and has an average width of about 5 km with depths ranging from 3 to 10 m. It opens into the NGOM via the East Pass or Destin Inlet, which is about 450 m wide. The inlet contains a channel with depths varying from above 10 m at the estuarine end to around 4 m in the inlet region to about 7 m at the eastern end, where the inlet connects to the Gulf of Mexico (Valle-Levinson et al., 2015; Handley et al.,

2007). The West Florida continental shelf is a broad, low energy area, with the 50 m isobath located at a distance of 30 km from the mouth of Choctawhatchee Bay. Tides are diurnal and weak in this region (Murphy et al., 2008; Bilskie et al., 2016) with spring and neap tidal ranges of 0.5 m and 0.15 m, respectively (Huguenard et al., 2016).

A series of experiments collectively referred to as the Surfzone Coastal Oil Pathways Experiment (SCOPE, <http://carthe.org/scope/>) were performed in this region by scientists from the Consortium for Advanced Research on Transport of Hydrocarbon in the Environment (CARTHE, <http://carthe.org/>). Field observations were collected during SCOPE to identify processes that influence surface transport in the inner shelf, which must be better understood to improve future predictions of nearshore transport pathways during an oil spill. During a 2 week period between 3–17 December 2013, data were collected with GPS-equipped surface drifters, helicopters, drones, balloons/kites, jet skis, small boats, ADCPs, CTD casts, and dye releases to describe nearshore wave and current movements (Valle-Levinson et al., 2015; Huguenard et al., 2016; Roth, 2016; Roth et al., 2017). Observations collected during SCOPE are the first step to provide insights into the wind- and plume-driven nature of the inner shelf circulation offshore of Destin Inlet. Those insights are described in the next few paragraphs, followed by a discussion of remaining knowledge gaps to be addressed by this study.

SCOPE observations (Valle-Levinson et al., 2015) confirm that tides near Destin Inlet are diurnal and similar to those observed at the NOAA gage at Panama City Beach. In the middle of Choctawhatchee Bay, tidal amplitudes were attenuated to 30% of the amplitudes at the entrance, and with a phase delay of 5.5 hr. During spring tides, observations indicate a moderate brackish outflow from Choctawhatchee Bay, which spreads radially outward in a semi-elliptical manner with an along-shore extent of about 3.5 km and a cross-shore extent of about 7.0 km. Plume velocity was opposed to the ambient currents to the west of the inlet, creating a distinct convergence zone that was visible in satellite imagery (Huguenard et al., 2016). Inlet salinity observations collected over the duration of a neap tidal cycle (9–10 December) provide interesting insights about transport processes within the inlet. They observe the presence of a depth-independent tidal intrusion front during early flood stage that can transport oceanic material into the inlet as a concentrated pulse, and a depth-dependent plume front during early ebb stage that can transport material seaward and prevent transport into the estuary (Valle-Levinson et al., 2015).

Cold fronts associated with extratropical storms are common during winter in the NGOM. These fronts propagate from west to east over 3 to 10 day periods and cause a 360 degree reversal in wind direction, with winds shifting from being southwesterly pre-front to northwesterly post-front (Roth, 2016; Feng et al., 2010). During December 2013, several cold fronts lasting between 3 to 5 days passed over the study area with average wind speeds of 5 m/s. These cold fronts cause rapid along-shore current reversals in the inner shelf with westward flow slowing from about 0.2 m/s to zero within an hour and accelerating to about 0.2 m/s eastward within 1 to 2 days (Roth, 2016; “Along-shelf Currents Forced by Crossshore Winds in the Inner Shelf of the Northeastern Gulf of Mexico”).

Drifters were released within the inlet during the ebb stage to identify the orientation of the Choctawhatchee River Plume as it emerges into the inner shelf. During easterly winds, the plume forms a coastal jet that flows west, parallel to the beach, and acts as a barrier that prevents surface drifters from beaching. During weak and variable winds, the plume expands radially outward without any preferential movement toward the east or the west. In both cases, plume boundaries introduce horizontal velocity gradients that cause drifters deployed outside the plume to converge along plume edges or be redirected offshore (Roth, 2016). Thus, offshore plume boundaries are expected to act as natural barriers that prevent surface material such as oil from beaching. When onshore winds carry oil to the shore, the plume can be effective near the inlet in reducing the amount of oil that washes ashore during the ebb stages (Kuitenbrouwer et al., 2018). The efficiency of these barriers depends on the interaction of these plume fronts with the ambient shelf currents and can be quantified via the plume velocity and thickness. When the plume velocity and ambient shelf currents act in concert, the stratification of the water column is enhanced, thus maximizing the efficiency of the natural barrier created by the plume. However, when the plume velocity and ambient current velocities are opposed, mixing at the plume front is enhanced and plume thickness decreases, thereby reducing the likelihood of barrier formation (Roth, 2016).

The largest waves recorded during the experiment period had a significant wave height of about 0.5 m and coincided with the passage of a cold front that occurred between 12–16 December. Throughout the experiment, relatively larger waves occurred when winds were from the south ahead of the frontal passage. Wave heights were reduced when winds were from any other direction due to limited fetch (“Along-shelf Currents Forced

by Crossshore Winds in the Inner Shelf of the Northeastern Gulf of Mexico”). Discharge from the Choctawhatchee River during SCOPE was about $150 \text{ m}^3/\text{s}$, which is close to its annual minimum.

SCOPE datasets have provided rich insights into several aspects of the shelf circulation near Choctawhatchee Bay. However, due to the limitations associated with a field experiment, the characteristics of the ebb-phase plume have only been observed at specific instances during that two-week period. The relative impact of wind and tidal forcing on the Choctawhatchee River Plume is still unknown. Variability in plume geometry due to changes in the realistic wind speeds and changes in tidal amplitudes brought about by spring and neap tides have not been investigated previously. Features of salinity transport within the bay including trends in longitudinal salinity gradients, vertical stratification and hydrodynamic timescale are also unknown.

Numerical models provide a greater flexibility to analyze the response of the coastal ocean to variability in the environmental forcing conditions. The aim of the present study is to apply the validated three-dimensional, numerical model for the Choctawhatchee Bay and Destin Inlet system to quantify the plume signature and its variability in response to changing tidal and wind forcing and investigate the characteristics of salinity conditions within the bay.

4.4 Variability in Ebb– and Flood–Phase Plume Signature

4.4.1 Wind Effects on Plume Geometry

The validated ADCIRC model is now applied to identify the plume response to changing wind conditions (Figure 4.1). We identify a period (24–27 November) when the tidal forcing is weak and constant (amplitude of 0.15 m). During this time, passing cold fronts lead to moderately-strong winds (4 to 10 m/s) that undergo a 360° reversal in their directions over a span of 3 to 4 days. The model plume is compared on these days for two scenarios. In the first scenario, the wind forcing is enabled, and therefore model predictions represent the plume response to both tidal and wind forcing mechanisms. In the second scenario, the wind forcing is disabled, and therefore the model predictions indicate how the plume behaves in the absence of wind forcing.

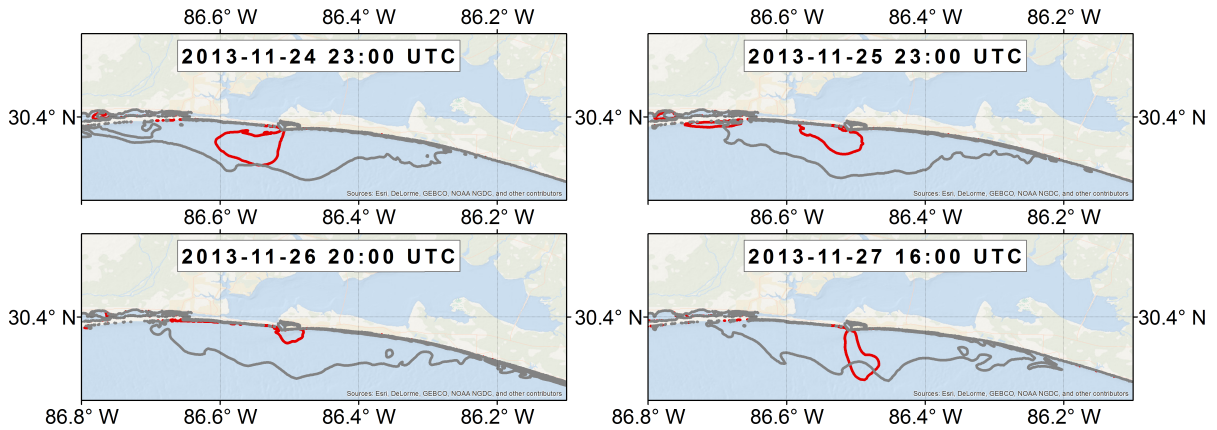


Figure 4.1 Model plume signature described by the 33 psu salinity contour on 24–27 November overlaid on ArcGIS Map Imagery. Red line shows model plume response to realistic wind forcing. Grey line shows model plume behavior when the wind forcing is disabled.

On 24 November, prevailing winds that are moderately strong (6 to 8 m/s) and northeasterly force the plume toward the west of the inlet, with a length of 6.58 km and a width of 9.0 km. In the absence of winds, the plume expands radially offshore with a similar length of 6.5 km. However it spreads offshore in a nearly symmetric manner and expands toward both the east and the west to a distance of roughly 20 km along the coastline.

On the next day (25 November), the winds remain northeasterly but are weaker (2 to 4 m/s). Due to the easterly component in the wind forcing, the plume is forced westward as it exits the inlet and stretches along the coastline to a distance of 7 km from the inlet. The width of the plume signature reduces to 6.5 km. The offshore spread of the plume to the south of the inlet is also limited, and the length of the plume (3.6 km) is roughly half of that of the previous day. When the wind forcing is disabled, the plume spreads along the coastline to east and west of the inlet, and it has a cross-shore extent of 5.5 km. Due to ambient currents flowing eastward, the advection of the surface plume to the east of the inlet is larger than the plume’s extension toward the west.

On 26 November, the winds have shifted and are blowing from the southeast and becoming southerly with wind speeds between 6 to 8 m/s. These winds prevent the plume from spreading farther offshore and restrict the plume length to be less than 3 km and width to be around 3 km. In the no-wind scenario, the plume expands radially offshore and spreads along the coastline to both the east and the west. The plume

signature has more than thrice the length of the realistic plume forced by both tides and winds.

On 27 November, while the wind speeds are similar at 6 to 8 m/s, the winds shift in direction and become northwesterly. The plume signature is significantly different from that of the previous days. The northerly component of the winds enhances the offshore advection and restricts the lateral (east-west) expansion of the plume, causing the length of the plume (8.0 km) to be more than twice its width (3.5 km). The plume signature changes dramatically when the winds are disabled, with the surface plume having a much larger width (20.0 km) and roughly the same length (3.0 km).

4.4.2 Tide Effects on Plume Geometry

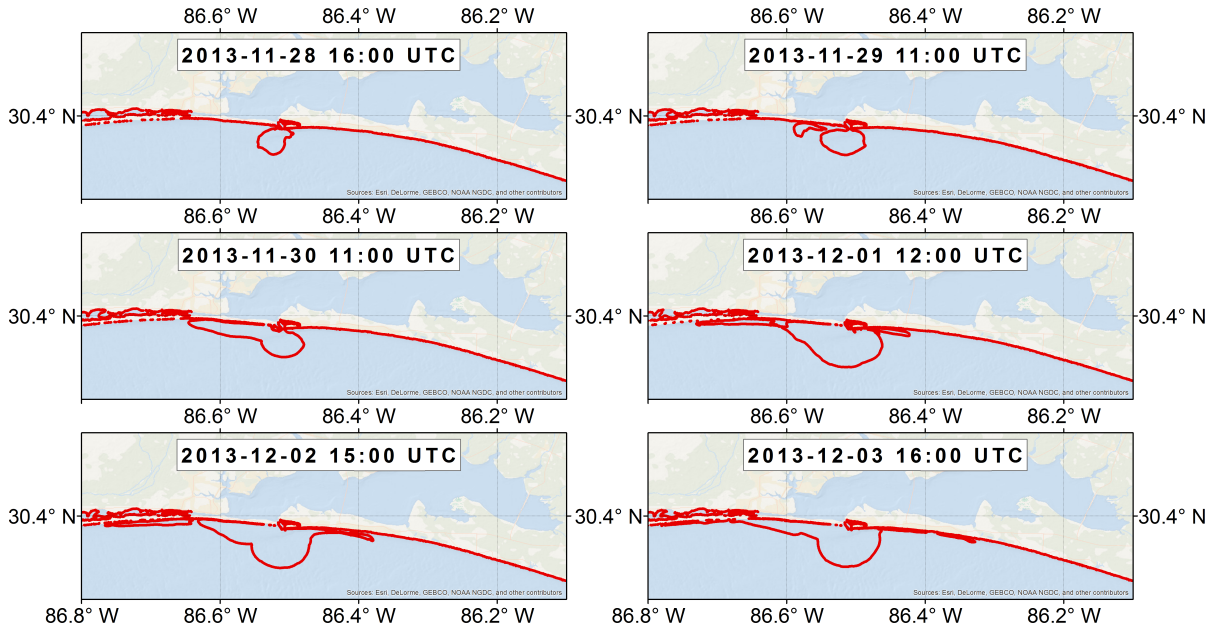


Figure 4.2 Model plume signature described by the 33 psu salinity contour (red line) during a period of neap-to-spring variability in the tides (28 November to 3 December) overlaid on ArcGIS Map Imagery.

To analyze tidal effects on the plume geometry, we choose a period when the tides transition from neap to spring and the wind speeds (near-constant between 4 to 6 m/s) and directions (near-constant and northerly) do not show a significant variability (Figure

4.2). On 28 November, the winds are northerly with wind speeds between 4 to 6 m/s. Tidal forcing is weak and has an amplitude of 0.12 m. The model plume is oriented slightly toward the west and has a length of 4.4 km and width of 3.6 km. On the next day, the winds are weaker (2 to 4 m/s) and northeasterly, and the tidal amplitude increases slightly to 0.13 m. The plume spreads out radially with a length of 4 km and width of 6.0 km.

The tides strengthen (to an amplitude of 0.22 m) on 30 November, whereas the wind forcing continue to be weak (2 to 4 m/s) and northeasterly. The ebb phase plume is advected farther toward the west along the coastline than in the previous days, and the width of the plume is larger and equal to 7 km. The cross-shore length of the plume is 4.26 km, similar to that of the previous day. The tidal amplitude strengthens further on 1 December (0.28 m). Wind forcing continues to be weak (2 to 4 m/s) and predominantly northeasterly. The plume spreads along the coastline to the west of Destin as in the previous day. However, the plume signature is larger with a width equal to 10.0 km and a length equal to 6.0 km on 1 December.

Very weak winds (0 – 2 m/s) blow from the northwest on 2 December. The plume footprint is identical to that of the previous day with an average length of 6.0 km and width of 10.0 km. The tidal amplitude steadily increases to 0.32 m on Dec 3. The plume is forced by weak (2 – 4 m/s) southerly winds. Although the plume advects to both the east and west of Destin, it remains restricted to the coastline. The plume footprint has a radial bulge south of Destin that has a length of 6.0 km and a width of 8.7 km.

4.4.3 Discussion

Winter cold fronts bring considerable variability in the wind conditions over the Florida Panhandle and influence the behavior of the ebb phase plume at Destin. Model predictions of salinities show that, during a period of near-constant tidal forcing and moderately strong winds of near-constant magnitude, the plume response can change significantly on consecutive days due to sharp changes in the direction of the prevailing winds. When there is a significant easterly component in the winds, the plume turns west as it exits the inlet and grows in its east-west extent (width). This is in agreement with the behavior of the drifters observed by SCOPE researchers in mid- to late-December (Roth et al., 2017). Our findings support their hypothesis that passing cold fronts can create sustained winds with an easterly component multiple times during winter 2013 and cause the ebb-phase

plume to form a coastal current west of Destin. Northerly or offshore winds enhance the cross-shore expansion of the plume, whereas southerly or onshore winds restrict the plume to the coastline. These results in a realistic model are also similar to the response of the adjacent Perdido Bay plume to idealized on-shore and off-shore wind conditions (Xia et al., 2011).

Wind speeds during 24–27 November are larger than 4 m/s and are therefore expected to influence plume dynamics in the near-field according to the criteria to delineate non-wind and wind forced conditions (Kakoulaki et al., 2014). Therefore, we expect a considerable difference in the model plume footprint when the winds are disabled and all other conditions remain the same. Model salinities reveal that the plume expands symmetrically to east and west of Destin with a larger footprint in the absence of wind forcing. Differences in the model plume response in the presence and absence of winds are in agreement with the behavior of the Perdido Bay plume, whose surface plume area, length, and width are smaller when forced by idealized wind conditions than without wind forcing (Xia et al., 2011). For the Choctawhatchee Bay plume, the only exception occurs when there are moderately strong northerly winds that enhance the surface advection of the plume south of the inlet and therefore increase the length of the plume. Ebb phase brackish outflows that enter the continental shelf are expected to turn right in the northern hemisphere and form a coastal current that extends down coast due to the influence of Earth’s rotation (Shi et al., 2010; Xia et al., 2007). The Kelvin number is used to quantify the relative importance of rotation effects on a river plume (Dzwonkowski et al., 2005). Due to the narrow geometry of Destin Inlet, the Choctawhatchee Bay plume is a small-scale river plume, with Kelvin number equal to 0.1 (Roth et al., 2017). Therefore, the effect of the Earth’s rotation is less pronounced for the Choctawhatchee Bay plume, which shows a preference to expand toward both the east and the west in the absence of wind forcing. Model tidal amplitudes decrease to less than 0.10 m between 26–27 November. The plume width is thus smaller on these days, when wind forcing is disabled, than in the previous days.

As the tides transition from neap to spring tides from 28 November to 3 December, the model plume grows in size. Under near-constant wind forcing, the length of the plume steadily increases from 4 to 6.0 km as the tidal amplitude increases from 0.12 to 0.31 m. There is an initial increase in the plume width as the tidal amplitudes change. However, the width of the plume remains constant 9 to 10.0 km when the tidal amplitude is larger

than 0.28 m.

This analysis provides an estimate of the variability associated with the plume signature as it responds to changing tidal and wind forcing. We can conclude that the cross-shore extent (length) of the plume is maximized (8.0 km) when spring tides combine with weak wind forcing or moderate northerly winds. The plume length is minimized (2.0 km) when neap tides combine with southerly winds. The alongshore extent (width) of the plume is largest (greater than 9.0 km) when the wind forcing is weak or absent. Under these conditions, the plume is restricted to near the coastline and expands in either direction to the east and the west. The plume width is minimized (3.0 km) when neap tides combine with moderate northerly and southerly winds.

The Choctawhatchee Bay plume plays a vital role in facilitating the offshore transport of surface material such as fish larvae, phytoplankton and pollutants out of the bay and the inlet into the continental shelf and preventing offshore chemical and oil pollutants from beaching. Therefore, understanding the variability in the east-west and north-south extents of the plume can provide useful guidance for local fisheries management and pollution control activities.

4.5 Estuarine Salinities

4.5.1 Inlet Salinities

During the flood and ebb phase of the tidal cycle, saline sea water is pushed in and out of Choctawhatchee Bay through Destin Inlet. Model salinities at the inlet during spring tide conditions indicate a surface-advected front during the ebb phase and a bottom-advected front during the flood phase of the tidal cycle. During early ebb, at 2 December 0600 UTC (Figure 4.3a), there is a large salinity gradient between the surface and the bottom layers when the buoyant brackish water (15 psu) from the bay arrives at the inlet. In about 3 hours at 2 December 0900 UTC (Figure 4.3b), inlet waters are well mixed in the central deeper portions with a salinity of 22 psu. Model predictions indicate a lateral salinity gradient across the inlet with brackish conditions in the deeper central region and more saline water being trapped along the shallow banks. During early flood (Figure 4.3c), at 2 December 1900 UTC, increase in salinities first occur in the bottom layer. About 3 hours later, at 2 December 2100 UTC (Figure 4.3d), the water column

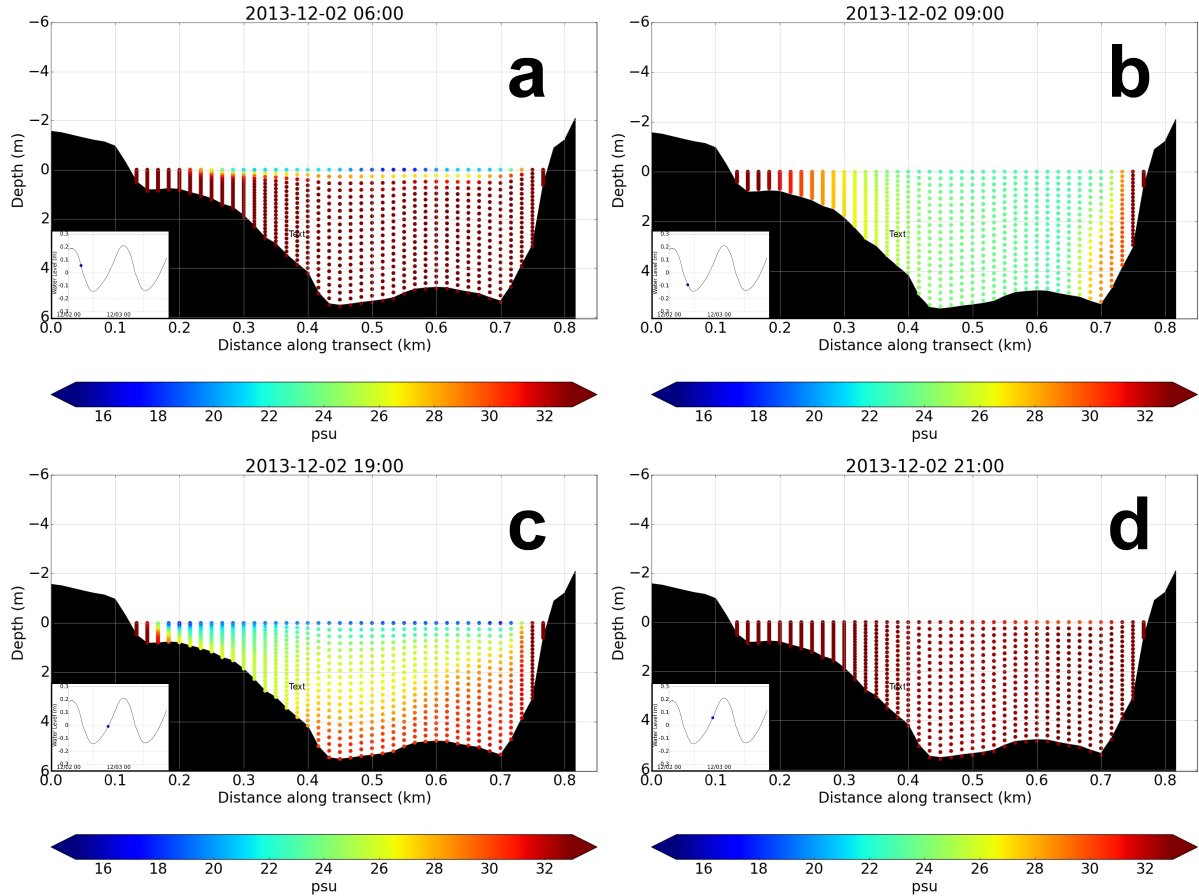


Figure 4.3 Model salinities across an east-west transect in the middle of the inlet (viewing from outside the bay). Inset images show the time relative to the tidal cycle.

is fully-mixed with a salinity of 33 psu throughout the water depth. Based on SCOPE observations, Valle-Levinson et al. (2015) reports that during neap tides, the salinity front at Destin Inlet is depth dependent (with surface changes leading bottom changes) during the ebb-phase and depth independent during the flood-phase. Model salinities capture the former behavior but mis-represents the latter. This is attributed to an under-representation of subgrid scale processes, which are responsible for horizontal and vertical diffusion of salinities in the inlet, within the model.

The flood phase of the tides is also associated with a distinct surface foot print. We now examine the geometry of the flood-phase plume signature and investigate its variability under changing wind and tidal conditions. The 31-psu salinity contour is used to represent the surface signature of the flood-phase plume predicted by the model.

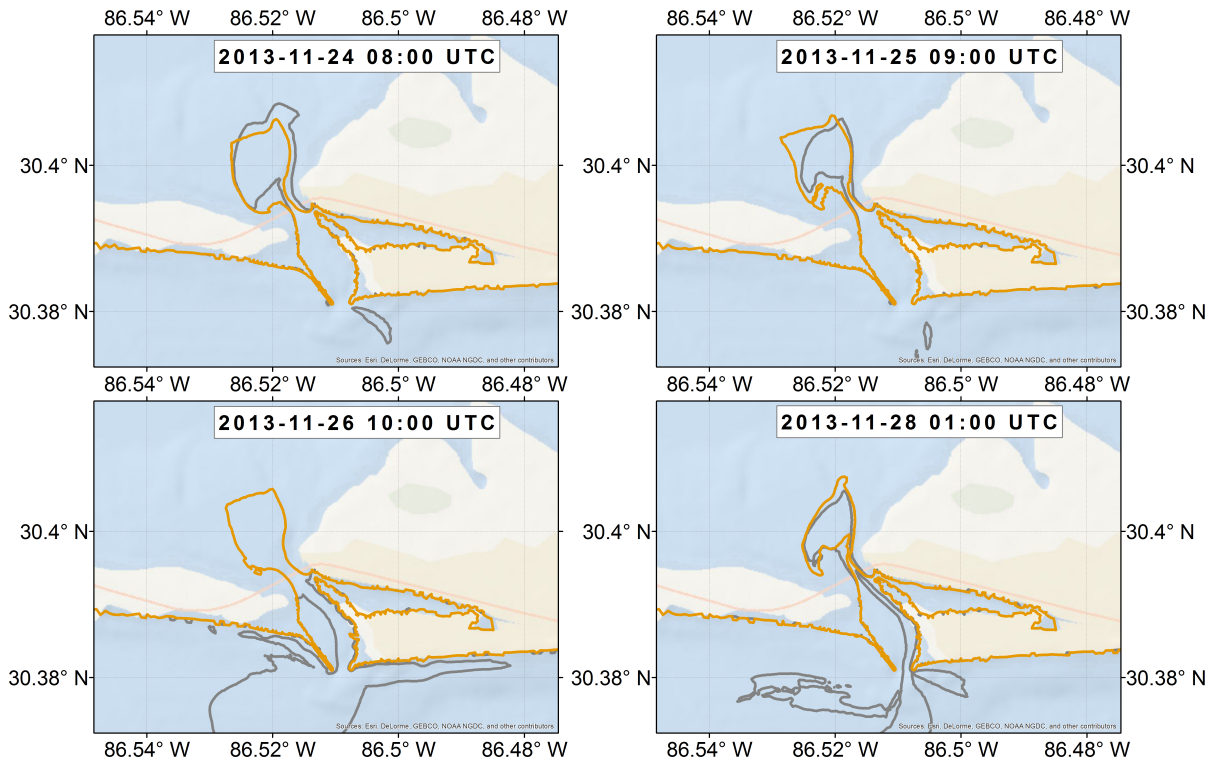


Figure 4.4 Model plume signature described by the 33 psu salinity contour on 24–27 November overlaid on ArcGIS Map Imagery. Red line shows model plume response to realistic wind forcing. Grey line shows model plume behavior when the wind forcing is disabled.

Throughout most of the study period, at late flood, the flood-phase plume advances to a distance of approximately 4 km from the mouth of the inlet and spreads horizontally as it enters the bay over a distance of 2 km. Unlike the buoyant ebb-phase surface plume, the flood-phase plume signature did not change significantly over consecutive days of variable wind and tidal forcing. For example, during a period (24–27 November) of near-constant tides and moderately-strong winds, which undergo a 360° reversal in their directions over a span of 3 to 4 days, we see that the geometry of the surface plume (orange lines in Figure 4.4) remains relatively the same at late flood during consecutive days. Also, even when the wind forcing is disabled, the plume geometry (dark grey lines in Figure 4.4) remains the same. Similarly, during a period (28 November – 3 December) when the tides transition from neap to spring and the wind speeds (near-constant between 4 to 6m/s) and directions (near-constant and northerly) do not show a significant variability, the geometry of the surface salt plume (Figure 4.5) at late-flood only changes slightly as we

transition from neap (28 November) to spring (3 December) conditions.

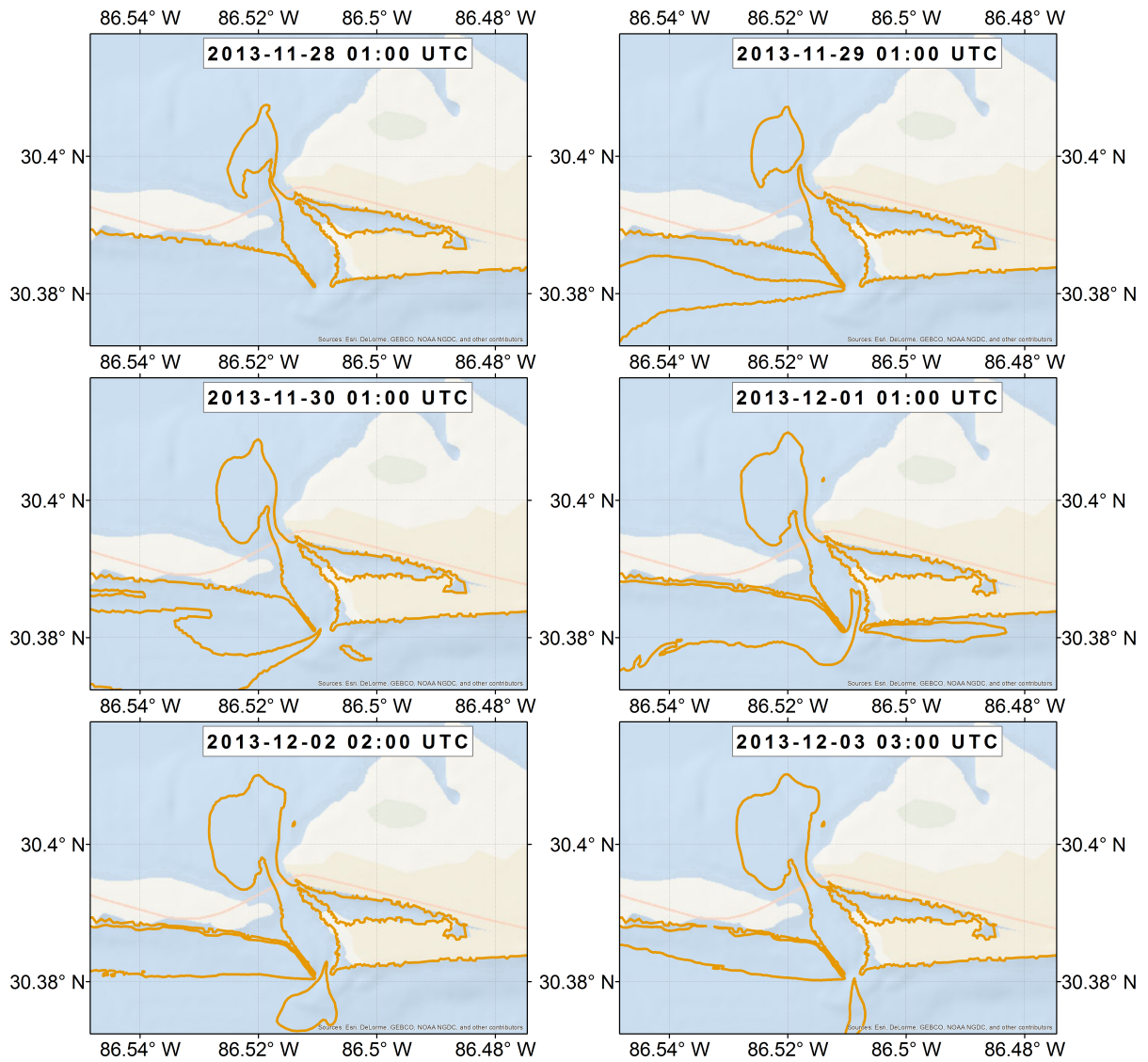


Figure 4.5 Model plume signature described by the 31 psu salinity contour (red line) during a period of neap-to-spring variability in the tides (28 November to 3 December) overlaid on ArcGIS Map Imagery.

4.5.2 Surface Salinities

Choctawhatchee Bay, like other estuaries, has a large spatial gradient in salinity with average salinities varying from a low of 7 psu near the river input on the east end to a high of 22 psu near the opening to the Gulf of Mexico towards the west end (Hoyer et al., 2013). For a mapping study of seagrass populations, the US Geological Survey identified three distinct zones in the Choctawhatchee Bay that are partly based on salinity: the most saline western bay, which included all areas west of the Hwy 293 Mid-Bay Bridge to Brooks Bridge (where Santa Rosa Sound begins); middle bay that includes all areas of the bay between the State Road (SR) 331 bridge and the Mid-Bay Bridge; and eastern bay that includes all areas east of the SR 331 bridge (Handley et al., 2007). Maximum depths range from 13 m in the west bay to 3 m in the east bay.

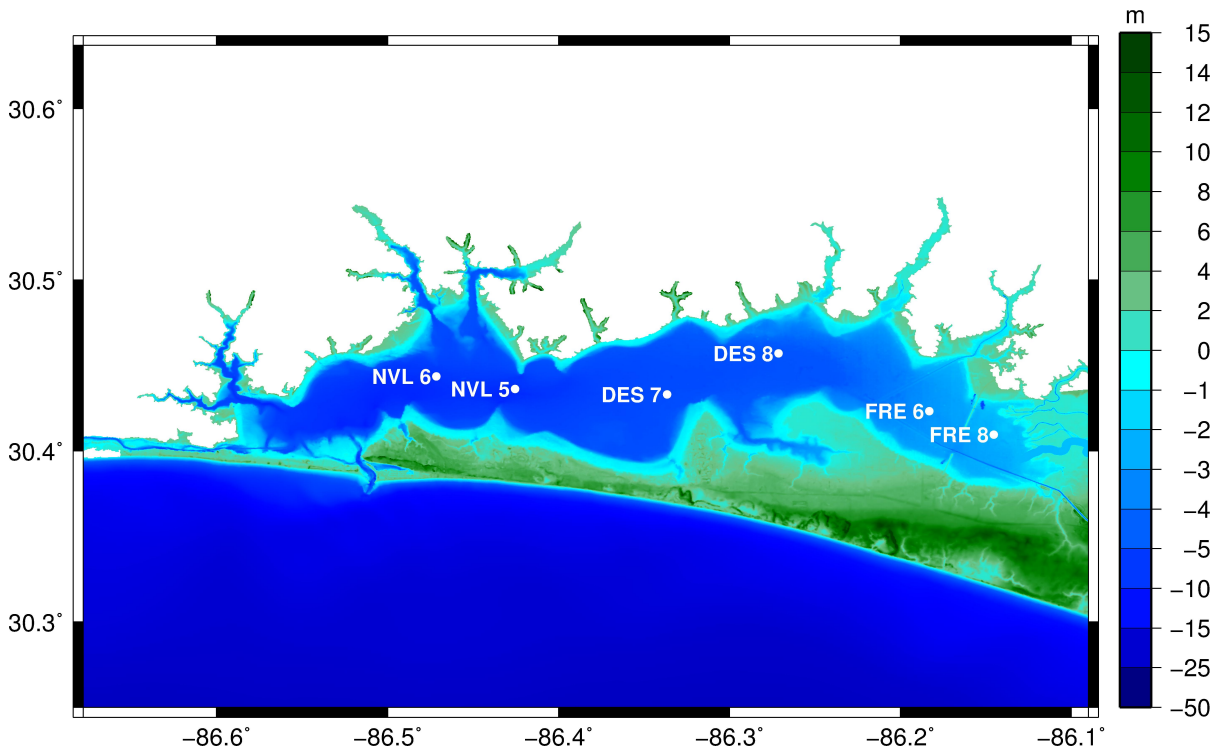


Figure 4.6 Locations at which monthly salinity measurements are collected by the Choctawhatchee Basin Alliance.

Based on monthly water quality data collected between 2001–2011 for 18 stations

within the bay, the Choctawhatchee Basin Alliance examined annual mean surface salinities to determine if there were identifiable zones with similar salinity (Hoyer et al., 2013). They applied a smoothing function to the salinity versus longitude plot and suggested that there are two identifiable sections of the bay, on either side of Longitude -86.30, which have different longitudinal salinity gradients. There is a rapid increase in salinity from east to west in the shallow part of the bay, which is followed by a much slower increase in salinity as the water enters the deeper part of the bay. However, their analysis also revealed that there is considerable monthly variance in the water chemistry of Choctawhatchee Bay due to seasonal fluctuations in the precipitation and river inflow. During the study period, when the river discharge was the largest (equal to 2000 m³/s in 2009) the salinities inside the bay were smaller and lesser than 20 psu throughout the bay. When the river discharge was small (equal to 100 – 200 m³/s in 2011), the bay was more saline with salinities greater than 20 psu throughout most of the bay, except near the river mouth.

Monthly salinity observations (Figure 4.7) collected by the Choctawhatchee Basin Alliance (CBA) between 2013–2014, at six locations within the bay, distributed from west to east (Figure 4.6), reveal substantial seasonal/monthly variability. Daily river flow records for Choctawhatchee River at the USGS station at Bruce, Florida during 2013–2014 are also available (Figure 4.7). Bruce is located about 30 km upstream from the mouth of the bay and water traveling at 1 m/s is expected to take about half a day to reach the river mouth (Jones et al., 1994).

During periods of large river discharge (more than 500 m³/s), such as during February–March 2013, July–September 2013 and April–May 2014, the surface layer is relatively fresh throughout most of the bay. Surface salinities are less than 10 psu at all the six stations. During periods of weak river flows (smaller than 200 m³/s), such as in October–December 2013 and September–December 2014, surface salinities are between 15 to 25 psu throughout most of the bay, except near the river mouth where the surface layer is mostly fresh due to inflow from Choctawhatchee River (Figure 4.7e-f). However, when there is a prolonged period of low river flows (e.g. October 2014), surface salinities can reach up to 20 psu even near the river mouth (FRE8 in Figure 4.7). Surface salinities are largest at the west end of the bay, with salinities of 25 psu at NVL6 (Figure 4.7) during low river flow conditions.

In the present study, we apply a river discharge of 150 m³/s, which is near the an-

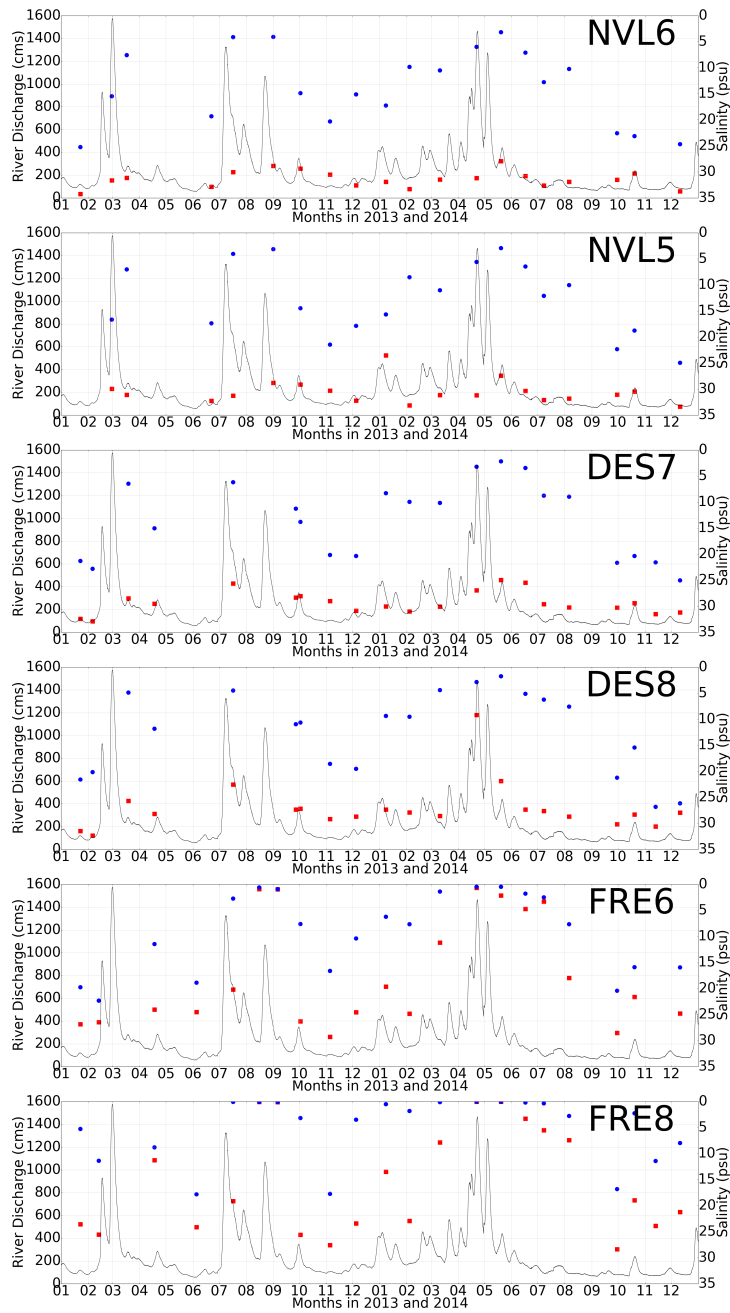


Figure 4.7 Observations for monthly surface (blue circles) and bottom salinities (red squares) collected by CBA at six stations inside the bay during 2013 and 2014. Black line represents the river discharge measured (in m^3/s) at the USGS gage located in Bruce, Florida for the same period.

nual minimum. Based on trends in the observed surface salinities at the CBA stations discussed above, we expect brackish conditions (15 to 25 psu) throughout most of the bay except near the river mouth. This trend is visible in the model salinities along the centerline of the bay (Figure 4.8) plotted for 2 December 2013 during late ebb. Although there is a steady increase in depths as we move from the shallow (3 m) eastern to the deeper middle (6 m) and western (10 m) parts of the bay, the salinities remain relatively constant throughout most of the bay. Beyond longitude -86.2, which is near the SR 331 Bridge that spans the bay at its east end, surface salinities sharply dip to around 5 psu due to the influence of the incoming freshwater inflow. Thus, due to the relatively low river discharge applied in the model, the freshwater influence is sharply felt only near the river mouth during winter 2013 unlike in summer months when the surface layer is fresh throughout the bay, even near the west end which is subject to stronger tidal effects. Also, surface salinities remained relatively constant during consecutive days of variable wind and tidal forcing conditions.

4.5.3 Stratification

For several decades, no comprehensive estuarine wide study has been conducted to analyze the hydrodynamics of Choctawhatchee Bay. Past studies that date back to the 1980s have concluded that the bay is highly stratified with limited flushing (Livingston, 2010). Low tidal energy, geometry of the bay, limited connectivity to the Gulf, and fluctuations in the discharge from Choctawhatchee River are expected to influence the spatial and temporal variability in the degree of stratification. Monthly surface and bottom salinities (Figure 4.7) collected by the CBA between 2013–2014 indicate the stratified nature of the bay. Bottom salinities stay larger than 25 psu in the western and central part of the bay irrespective of variability in the river inflow.

Stratification is larger during periods of high river inflow (more than 500 m³/s), such as during February–March 2013, July–September 2013 and April–May 2014, due to large gradient between the relatively fresh surface water and saline bottom layer in most of the bay. Differences between the surface and bottom salinities reach up to 25 psu at NVL6 and NVL5 during this time. The vertical salinity gradient continues to be large (15–20 psu) as we transition to mid-bay (DES7 and DES8 in Figure 4.7). At the west end of the bay, near the river mouth (FRE6 and FRE8 in Figure 4.7), the freshwater inflow penetrates most of the water column resulting in fresh or brackish conditions throughout

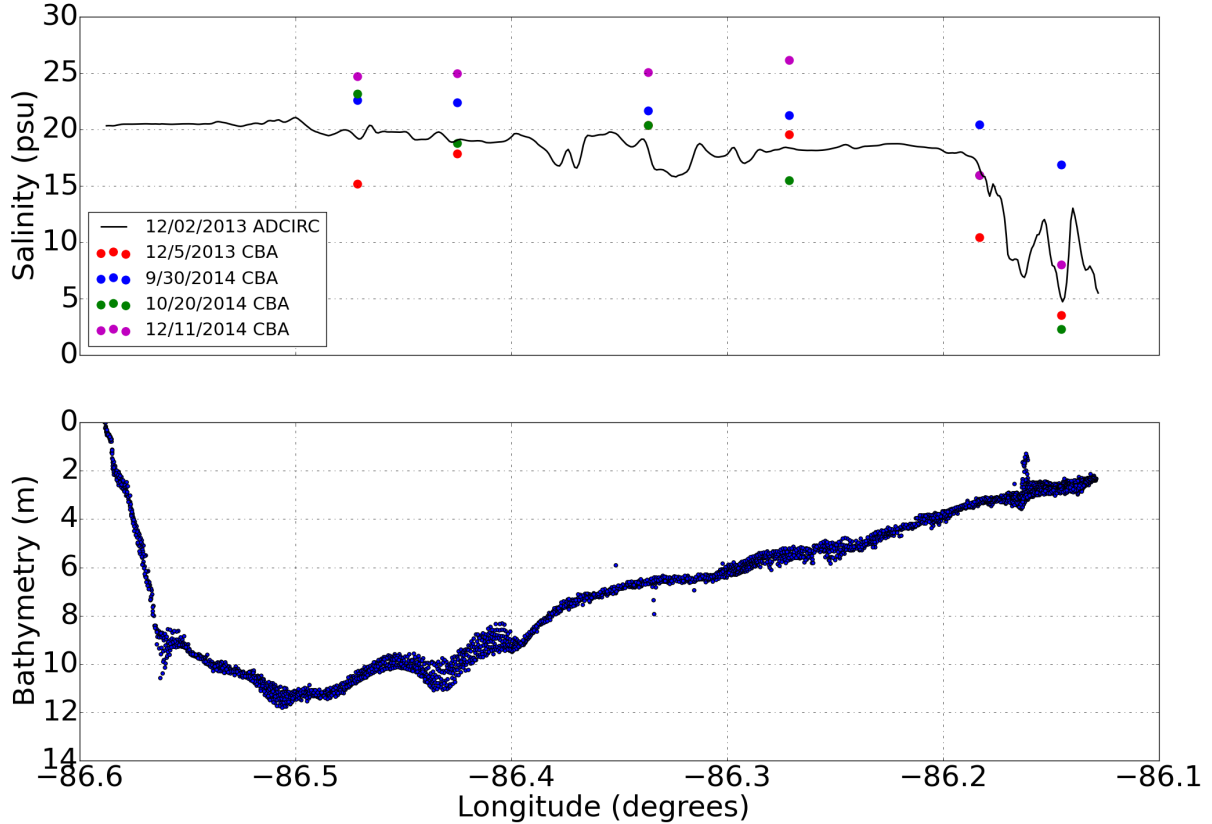


Figure 4.8 Top panel shows surface salinities inside the bay. Black line represents model salinities along the bay axis. Circles correspond to observed salinities at 6 stations inside the bay. Circles are colored according to their time-stamp. Bottom panel shows how bathymetry changes from west to east in the bay.

most of the water column. When river flows are low, such as in October–December 2013 and September–December 2014, the vertical salinity gradient is smaller due to more brackish and saline conditions in the surface layer. The magnitude of stratification ranges between 10 – 15 psu throughout the bay during this time.

Model predictions for November–December 2013, a period characterized by relatively low discharge from the Choctawhatchee River ($150 \text{ m}^3/\text{s}$), reveal significant vertical variability in the water salinities throughout most of the bay (Figure 4.9). This is in agreement with the highly-stratified conditions observed in the bay during low river flow conditions (discussed above). In NVL6 and NVL5, located in west bay, the water column has brackish (15 – 20 psu) conditions over the top 2 m, which gradually transitions to a bottom highly saline (32 psu) layer. The water column remains stratified at these

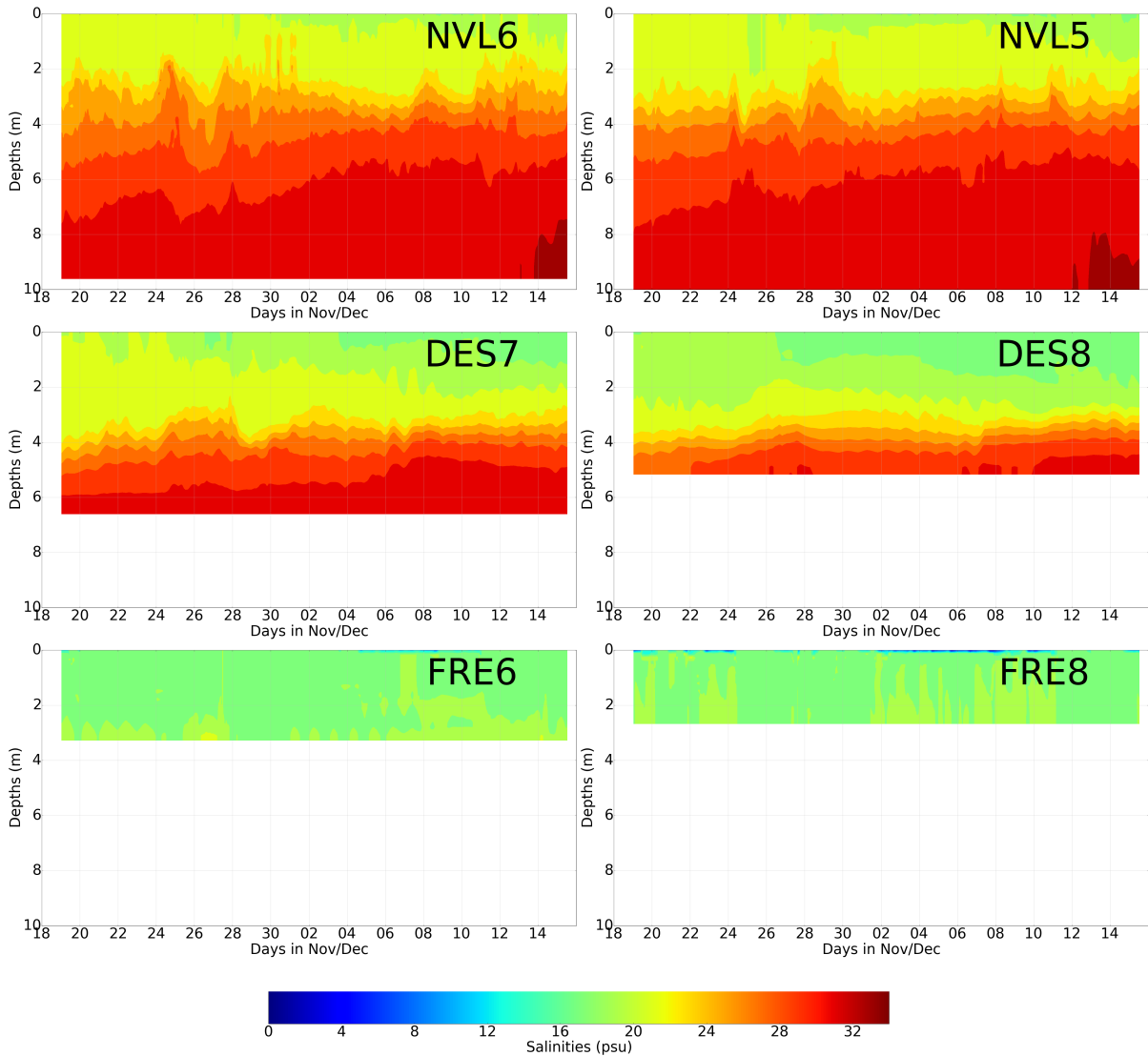


Figure 4.9 Model salinity contours at the six CBA stations inside the bay during November-December 2013.

two stations, with a difference of 10 – 15 psu between the surface and bottom salinities throughout the study period. In DES7 and DES8, located in mid-bay, the water column continues to be highly stratified with the same amount of stratification. However, unlike in the west bay, the brackish water penetrates lower into the water column (over the top 4m). Bottom salinities range from 30 – 32 psu at these stations. Model predictions indicate fully mixed brackish conditions in east bay, at FRE6 and FRE8,

with the incoming freshwater from Choctawhatchee Bay not penetrating the entire water column. It is suspected that there is ‘over-mixing’ in the model near the river mouth, which might be caused due to an overestimation of the vertical eddy diffusivity. More extensive sensitivity studies, beyond the scope of this work, would be necessary to resolve this issue.

4.6 Residence Time

Estuarine timescales, such as residence time and flushing rates, are important tools to compute the rate of removal of pollutants, contamination and nutrient levels, distributions of organisms and their spatio-temporal variations, rates of export of fish eggs and larvae released within a bay, etc. (Webb et al., 2016; Aikman et al., 2005). These hydrodynamic timescales are important indicators of estuarine health and water quality, but they have not been computed before for the Choctawhatchee Bay. Residence time is defined as “the time required for a fluid parcel, starting at a specific location, to leave a discrete region through one of its defined boundaries” (Webb et al., 2016; Aikman et al., 2005). Flushing time is calculated as “the amount of time required to reduce some initial concentration to $1/e$ ($e = 2.71828$; $1/e = 0.37$) of its initial value” (Zimmerman, 1976). Fine-mesh numerical models that provide a high level of spatial and temporal resolution are commonly used with particle tracking models for computing these quantities and describing the factors that influence their variability (Aikman et al., 2005; Liu et al., 2011; Defne et al., 2015; Marsooli et al., 2018). For example, Webb et al. (2016) applied a 2D ADCIRC model to analyze the spatially-dependent timescales of Mobile Bay, Alabama, and found that spatially-averaged timescales in the bay generally ranged from 4 to 130 days, with large deviations related to particle initial position, magnitude of river discharge, and local winds. Meteorological forcing was found to increase the spatial variance in hydrodynamic timescales by as much as 60 percent as compared with cases with discharge and tides only. Similar timescales were observed in a modeling study for a series of shallow, coastal bays in the Virginia Coastal Reserve with computed residence times ranging from hours in the tidally-refreshed water near the inlets, to days and weeks in the remaining water away from the inlets (Safak et al., 2015). The effect of winds was higher away from the inlets and in relatively confined bays with the wind forcing acting as a diffuser that shortens particle residence within the bays.

In the present study, we apply a particle tracking algorithm (Dietrich et al., 2012b; Webb et al., 2016) that uses surface currents from the validated ADCIRC model to predict the movement of Lagrangian particles that are released at the mouth of Choctawhatchee River. The surface currents computed by ADCIRC are applied in the particle tracking code to advect the passive particles every 10 minutes. The dispersion of the particles due to turbulence is parameterized by a stochastic velocity perturbation term that is computed using a random walk algorithm. More details of the particle tracking algorithm are described in Dietrich et al. (2012b).

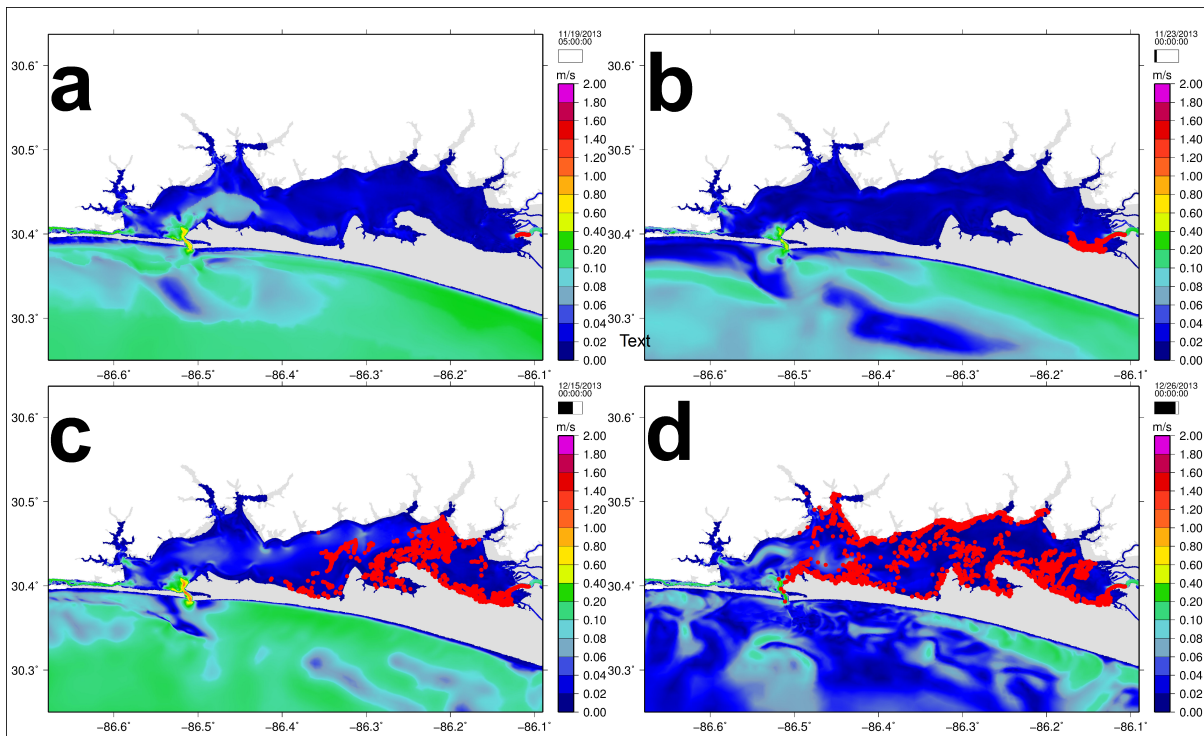


Figure 4.10 Path traced by Lagrangian particles advected by ADCIRC surface currents. Red circles denote particle position. Contours represent magnitude of surface currents predicted by the model.

Lagrangian particles are released continuously from a source located at the river mouth and advected by the underlying surface currents predicted by the validated model 4.10. The initial release of particles is made at 19 November 0500 UTC (Figure 4.10a). In roughly four days, by 23 November 0000 UTC, these particles cross the SR 331 bridge that

spans the bay at the east end (Figure 4.10b). The particles are advected to the middle of the bay by 15 December 0000 UTC (Figure 4.10c). Eventually, the particles arrive at the inlet on 26 December 0000 UTC (Figure 4.10d). Thus, the time taken for a Lagrangian particle or a passive tracer that is released at the mouth of the inlet to escape from the bay through Destin Inlet is about 36.75 days. This estimate matches anecdotal evidence about residence times in Choctawhatchee Bay collected through private correspondence.

4.7 Summary

The validated model described in Chapter 3 is applied to investigate salinity characteristics within Choctawhatchee Bay and the adjacent continental shelf. Our analyses reveal that the behavior of the ebb phase plume can be very different on consecutive days in Winter 2013 due to passing cold fronts and spring-neap transitions. During a continuous 2-3 day period of near-constant tides, there were substantial changes in the length, width and orientation of the plume as the wind direction varied. Easterly winds prompted the plume to turn west. Moderate northerly winds during spring tides limit the plume width and enhances the plume length or its offshore expansion. Southerly winds restricted the plume to the coastline. During a period of near-constant winds and variability in tidal amplitude, the model predicted a larger plume during spring tides than during neap conditions. When the wind forcing is weak, the plume signature is generally larger and spreads along the coastline to the east and the west.

Model salinities at the inlet indicate a surface advected brackish plume during the ebb-phase and bottom advected salt plume during the flood-phase of the tidal cycle. Unlike the ebb-phase surface plume, the surface salt plume during late flood remains relatively constant under changing tidal and wind forcing conditions. Observed monthly salinities indicate that bay salinities undergo seasonal variability in response to fluctuation in the incoming river discharge. Model salinities indicate that the bay is highly stratified during periods of low river discharge such as November-December 2013 and is in agreement with trends in observed salinities. Finally, the residence time of passive pollutants released at the river mouth is computed using a Lagrangian particle tracking method and is found to be equal to 37 days. The highly stratified conditions in the bay and long residence time predicted by the model are reasonable considering the micro-tidal character of Choctawhatchee Bay.

Surface advected estuarine plumes create density fronts which significantly influence the transport of surface material such as fish larvae, phytoplankton, oil and other chemical pollutants. Salinity characteristics within estuaries and its spatial and temporal variability play a crucial role in the sustenance of estuarine plant and animal habitats. This modeling study provides insights about the expected variability plume geometry under changing environmental conditions. Model predictions also illustrate key features of salinity transport within Choctawhatchee Bay. Research findings can therefore guide efficient decision making for estuarine resource management, oil spill response operations and pollution management.

Chapter 5

Concluding Remarks

The response of the shallow coastal ocean, which is subject to tides, winds, waves and river inflows, can have considerable spatial and temporal variability. During storm events, large winds and waves combine with daily tidal effects to generate surge that can cause flooding in the low-lying areas along estuarine banks and on the sound- and ocean-side of barrier island systems. Salinities within estuaries fluctuate as river flows undergo seasonal variability. In the vicinity of tidal inlets, ebb-phase buoyant plumes, which may be shallow and susceptible to wind effects, can influence inner shelf surface transport and stratification.

This thesis contributes to the scientific understanding of estuarine behavior in the following three ways: a) improving storm surge prediction for estuarine systems by showing how separate errors in storm track and strength can cause errors in wind and surge predictions in the estuaries and sounds of North Carolina, b) development and validation of a three-dimensional, fully baroclinic shelf-estuarine scale numerical model for Choctawhatchee Bay, c) application of the validated model to investigate variability of the ebb-phase estuarine plume at Destin and d) quantification of trends in surface salinities, stratification and residence times within Choctawhatchee Bay. Important insights that were gained in each of these areas and their significance are summarized in the following paragraphs.

The coastline of North Carolina is characterized by a network of rivers, estuaries, sounds and barrier islands and is vulnerable to storm surge flooding due to its unique location in the East Coast of the United States. Hurricane Arthur made landfall in early July 2014 and caused storm surges up to 2.5 m in the low lying areas along the

coastline. As the hurricane moved over the Pamlico and Albemarle sounds, which receive freshwater input from many mainland rivers, winds first pushed water against the river estuaries and the inner banks of the sound, and then moved eastward to threaten the sound-side of the barrier islands. Forecast advisories issued by the National Hurricane Center were applied within the ADCIRC Surge Guidance System to develop real-time storm surge predictions. The storm track predictions from the NHC improved over time. However, successive advisories predicted an unrealistic increase in the storm's strength. Due to these forecast errors, the global root mean square errors of the predicted wind speeds and water levels within the estuaries and sounds increased as the storm approaches landfall. In the present study, the sensitivity of these storm surge predictions to errors in the NHC forecast storm track and strength are separately investigated. First, the high-resolution SWAN+ADCIRC model is applied to perform hindcast simulations on a large unstructured mesh to analyze the surge impact of Arthur along the NC coastline. The effects of Arthur are best represented by a post-storm, data-assimilated wind product with parametric vortex winds providing a close approximation. Second, the relative impacts of the track and strength errors on the surge predictions are assessed by replacing forecast storm parameters with the best-known post-storm information about Arthur. In a "constant track" analysis, Arthur's post-storm determined track is used in place of the track predictions of the different advisories, but each advisory retains its size and intensity predictions. In a "constant storm strength" analysis, forecast wind and pressure parameters are replaced by corresponding parameters extracted from the post-storm analysis, while each advisory retains its forecast storm track. A strong correlation is observed between the forecast errors and the wind speed predictions. However, the correlation between these errors and the forecast water levels is weak, thus signifying a nonlinear response of the shallow estuarine and sound waters to meteorological forcing. This study demonstrates the potential for forecast errors in peak wind speeds and surge levels due to separate errors in storm track and power. It provides guidance for real-time forecast systems to account for both track errors and intensity errors as they design what-if scenarios to forecast hurricane impacts in estuarine systems.

A recently-enhanced, three-dimensional, baroclinic version of ADCIRC is then applied, after recent improvements, to simulate the tide-, wind- and density-driven circulation in the vicinity of Choctawhatchee Bay. The model is initialized by combining observed salinities within the bay and model output from a regional ocean model. The

physical forcings that are applied include winds, tides, freshwater input and surface heat flux. Model water levels and vertical salinities are validated against in-situ observations available for December 2013. The observed and modeled water levels are in good agreement, with ADCIRC sometimes underestimating the observed water levels by 0.1 to 0.2 m. In the stratified portion of the water column, there is a high degree of correlation (> 0.6) between observed and modeled salinity profiles at most locations. The computed error statistics (with E_{CRMS} less than 0.5 and B_M less than 2 psu) also indicate a good match between observed and modeled salinities in regions where the water column is fully mixed. Lagrangian particles advected by ADCIRC surface currents are compared against the observed transport pathways of drifters released during SCOPE. Although along-shore currents in the shelf are under-estimated, salient features of the wind- and plume-driven circulation that drive drifter movement are captured reasonably well by the modeled surface currents. Model predictions of the ebb-phase plume signature at Destin are compared against the visible plume in SCOPE satellite imagery. The model and observed plume footprints are in good agreement with the cross-shore extent of the plume being underestimated by roughly 1.5 to 2 km in the model. Overall, the validation efforts indicate that the three-dimensional baroclinic ADCIRC model is able to successfully represent the chief characteristics of the salinity transport and wind- and plume-driven nature of the circulation in the vicinity of Choctawhatchee Bay.

Due to the passage of cold fronts and fortnightly variations in the tidal amplitudes, the ebb-phase brackish outflow at Destin is subject to changing environmental conditions. The response of the ebb-phase plume at Destin to these changes is investigated in two scenarios. In the first case, model plume behavior is analyzed on successive days of near-constant tidal amplitudes and changing wind directions due to passing cold fronts. In the second case, plume response is studied during consecutive days of neap-spring variability in the tides and near-constant wind speeds. Model results reveal a larger plume during spring tides and periods of weak wind forcing. Offshore winds enhance the north-south expansion of the plume, whereas onshore winds restrict the plume to the coastline. The plume geometry can influence the transport of biological and chemical material in the vicinity of the inlet, and therefore insights from this study can be useful for oil spill response operations, fisheries and pollution management.

The present study is novel because there have not been any estuary-wide modeling studies in recent decades to investigate the hydrodynamics within Choctawhatchee Bay.

The validated ADCIRC model is applied in this thesis to perform exploratory studies to gain insights about bay salinities. Model salinities at the inlet during spring tide reveal that salinity changes first occur at the surface layer during early ebb. The behavior is reversed during the flood phase, with the salt front entering the inlet in a bottom advected manner. The latter behavior contradicts the depth dependent nature of the salt plume reported in SCOPE observations during neap tide. Further investigations are necessary to improve model behavior at the inlet. The surface footprint of the flood-phase salt plume do not exhibit much variability during periods of changing wind and tidal forcing.

Observed monthly salinities during 2013 and 2014 indicate that, during periods of high river discharge from Choctawhatchee River, salinities within the bay fall below 10 psu. During periods of low river flows, more saline conditions (15 – 25 psu) exist throughout the bay. The time period for the present study is November–December 2013, which is a period of relatively low river discharge. Trends in model salinities match that of observations. Salinities throughout the bay stay around 20 psu except near the river mouth, where the surface water is fresh. During November–December 2013, model salinities reveal a high degree of stratification (10 – 15 psu) throughout most of the bay, except near the east end, where the effect of freshwater do not penetrate adequately into the water column. Further tuning of eddy diffusivity and a more realistic representation of the river channel (described below as future work) is expected to provide more realistic results. Residence times within the bay are computed by estimating the time taken for a passive tracer released at the river mouth to be transported out of the inlet. Lagrangian particles are advected by the modeled surface currents within the bay using a particle tracking algorithm. The residence time within the bay is estimated to be roughly 40 days, which matches anecdotal evidence.

Insights from this work can be further expanded by future exploratory studies. One of the limitations associated with this study is that Choctawhatchee River is represented using a ‘synthetic’ channel (panel a in Figure 5.1), which is three times wider than the real channel. Upstream of Bruce, all the twists and turns that are present in the real channel are replaced by a simpler profile in the synthetic channel. Future work will simulate freshwater transport in Choctawhatchee River using a “realistic” channel (panel b in Figure 5.1), which incorporates the complexities in the upstream river profile. A more accurate representation of the channel geometry is expected to improve the prediction of surface currents and salinity transport within the bay, especially in east bay. Work

on designing this channel and integrating it to the mesh has already been completed in collaboration with an undergraduate researcher. This was done by painstakingly tracing the banks and centerline of the channel with the help of satellite imagery and mesh editing tools within SMS (Surface-water Modeling Software).

For the present study, we have implemented a constant river discharge throughout the study period, which is near the annual minimum discharge for the river. Observed monthly salinity data discussed in Chapter 4 reveal that bay salinities exhibit significant variability depending on the incoming river discharge. Future work will explore the response of estuarine salinities over a range of discharge conditions that are typical for Choctawhatchee River. The present study has only explored aspects of estuarine and shelf salinities because density changes in the study area are primarily driven by changes in salinities. Future work will attempt to validate model temperature predictions and quantify the range of surface and bottom temperatures within Choctawhatchee Bay. In this thesis, a preliminary analysis based on a Lagrangian particle release experiment was performed to assess residence times within the bay. There are several different ways to compute residence times. Future work will explore the computation of residence times by freshwater fraction method and compare with corresponding estimates from particle tracking experiments. Residence times within the bay might have considerable spatial variability and be influenced by prevailing winds and river flows. Future work will explore the relative effects of each of these factors on residence time behavior in Choctawhatchee Bay.

Although this work was specific to the sounds and estuaries of North Carolina and Florida, insights from this study can be applied to other estuarine systems. High winds during hurricanes can result in positive and negative surge along estuarine banks. Forecast systems should take into account errors in both intensity and track errors while making surge predictions. The behavior of brackish, estuarine, ebb-phase plume could be different on consecutive days depending on the environmental conditions. Prediction of the plume geometry is useful as expected plume behavior will be critical for predicting the transport of surface material such as fish larvae, oil and chemical pollutants. Estuarine salinities exhibit a strong correlation with river flows, with lower salinities associated with higher discharges and larger salinities associated with low river flows. Our results indicate that in highly-stratified estuaries with low tidal energies, the large vertical salinities remain relatively unaffected by the passage of cold fronts and neap-spring tidal

variations. Trends in estuarine surface salinities, stratification and residence times have important implications for estuarine water quality and the survival of estuarine plant and animal habitats and therefore, insights from this study will be useful for estuarine resource management.

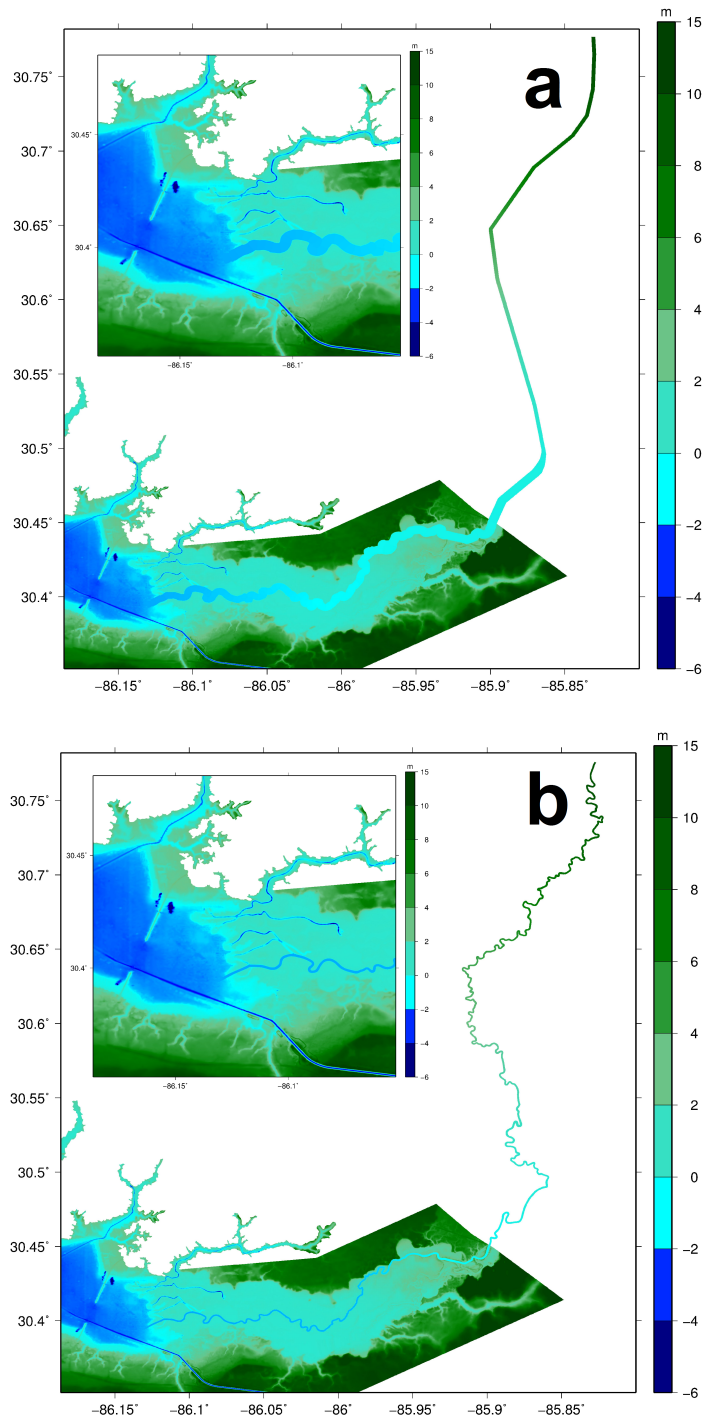


Figure 5.1 Representation of Choctawhatchee River in the ADCIRC mesh. Top panel shows the ‘synthetic’ channel and bottom panel shows the ‘realistic’ channel. Inset images zoom to the east end of the bay where the river enters the bay.

BIBLIOGRAPHY

- Adcroft, A., Campin, J.-M., Dutkiewicz, S., Evangelinos, C., Ferreira, D., Forget, G., Fox-Kemper, B., Heimbach, P., Hill, C., Hill, E., Hill, H., Jahn, O., Losch, M., Marshall, J., Maze, G., Menemenlis, D. & Molod, A. (2016). *MITgcm user manual*. Tech. rep. Cambridge, MA.
- Aikman, F & Lanerolle, L. W. J. (2005). “Report on the NOS Workshop on Residence/Flushing Times in Bays and Estuaries. Silver Spring, Maryland”.
- Androulidakis, Y. S. & Kourafalou, V. H. (2011). “Evolution of a buoyant outflow in the presence of complex topography: The Dardanelles plume (North Aegean Sea)”. *Journal of Geophysical Research: Oceans* **116**.C4.
- Asselin, R (1972). “Frequency filter for time integrations”. *Monthly Weather Review* **100**, pp. 487–490.
- Atkinson, J. H., Smith, J. M. & Bender, C (2013). “Sea-Level Rise Effects on Storm Surge and Nearshore Waves on the Texas Coast: Influence of Landscape and Storm Characteristics”. *Journal of Waterway, Port, Coastal, and Ocean Engineering* **139**, pp. 98–117.
- Barnes, J (2013). *North Carolina’s Hurricane History*. 4th ed. University of North Carolina Press.
- Barnier, B, Marchesiello, P, Miranda, A. P. D., Molines, J. M. & Coulibaly, M (1998). “A sigma–coordinate primitive equation model for studying the circulation in the South Atlantic. Part I: Model configuration with error estimates”. *Deep Sea Research Part I: Oceanographic Research Papers* **45**.4–5, pp. 543–572.
- Berg, R (2015). *Tropical Cyclone Report, Hurricane Arthur, 1 - 5 July 2015*. Tech. rep. National Hurricane Center.
- Bhaskaran, P. K., Nayak, S, Bonthu, S. R., Murthy, P. L. N. & Sen, D (2013). “Performance and validation of a coupled parallel ADCIRC-SWAN model for THANE cyclone in the Bay of Bengal”. *Environmental Fluid Mechanics* **13**, pp. 601–623.
- Bilskie, M. V., Hagen, S. C., Medeiros, S. C., Cox, A. T., Salisbury, M & Coggin, D (2016). “Data and numerical analysis of astronomic tides, wind–waves, and hurricane storm surge along the Northern Gulf of Mexico”. *Journal of Geophysical Research: Oceans* **121**.5, pp. 3625–3658.

- Blain, C. A., Cambazoglu, M. K. & Kourafalou, V. H. (2009). “Modeling the Dardanelles strait outflow plume using a coupled model system”. *OCEANS 2009*, pp. 1–8.
- Blain, C. A., Cambazoglu, M. K., Linzell, R. S., Dresback, K. M. & Kolar, R. L. (2012). “The predictability of near-coastal currents using a baroclinic unstructured grid model”. *Ocean Dynamics* **62**.3, pp. 411–437.
- Blanton, B. O. & Luettich, R. A. (2008a). *North Carolina Coastal Flood Analysis System: Model Grid Generation*. Tech. rep. TR-08-05. Renaissance Computing Institute.
- Blanton, B. O., Madry, S, Gallupi, K, Gamiel, K, Lander, H, Reed, M, Stillwell, L, Blanchard-Montgomery, M, Luettich, R, Mattocks, C, Fulcher, C, Vickery, P, Hanson, J, Devaliere, E & McCormick, J (2008b). *Report for State of North Carolina Floodplain Mapping Project Coastal Flood Analysis System*. Tech. rep. TR-08-08. Renaissance Computing Institute.
- Blanton, B. O., Luettich, R. A., Hanson, J. L., Vickery, P, Slover, K & Langan, T (2012a). *North Carolina Floodplain Mapping Program, Coastal Flood Insurance Study: Production Simulations and Statistical Analyses*. Tech. rep. TR-12-03. Renaissance Computing Institute.
- Blanton, B. O., McGee, J, Fleming, J. G., Kaiser, C, Kaiser, H, Lander, H, Luettich, R. A., Dresback, K. M. & Kolar, R. L. (2012b). “Urgent Computing of Storm Surge for North Carolina’s Coast”. *Proceedings of the International Conference on Computational Science*. Vol. 9, pp. 1677–1686.
- Bunya, S, Dietrich, J. C., Westerink, J. J., Ebersole, B. A., Smith, J. M., Atkinson, J. H., Jensen, R. E., Resio, D. T., Luettich, R. A., Dawson, C. N., Cardone, V. J., Cox, A. T., Powell, M. D., Westerink, H. J. & Roberts, H. J. (2010). “A High-Resolution Coupled Riverine Flow, Tide, Wind, Wind Wave and Storm Surge Model for Southern Louisiana and Mississippi: Part I – Model Development and Validation”. *Monthly Weather Review* **138** (2), pp. 345–377.
- Callies, U, Groll, N, Horstmann, J, Kapitza, H, Klein, H, Maßmann, S & Schwichtenberg, F (2017). “Surface drifters in the German Bight: model validation considering windage and Stokes drift”. *Ocean Science* **13**.5, pp. 799–827.
- Chant, R. J., Wilkin, J, Zhang, W, Choi, B, Hunter, E, Castelao, R, Glenn, S, Jurisa, J, Schofield, O, Houghton, R, Kohut, J, Frazer, T. K. & Moline, M. A. (2008). “Dispersal of the Hudson River Plume in the New York Bight: Synthesis of Observational and Numerical Studies During LaTTE”. *Oceanography* **21**.

- Chen, C, Liu, H & Beardsley, R. C. (2003). “An unstructured grid, finite-volume, three-dimensional, primitive equations ocean model: Application to coastal ocean and estuaries”. *J. Atmos. Oceanic Technol.* **20** (1), pp. 159–186.
- Cheung, K. F., Phadke, A. C., Wei, Y, Rojas, R, Douyere, Y. J. M., Martino, C. D., Houston, S. H., Liu, P. L. F., Lynett, P. J., Dodd, N, Liao, S & Nakazaki, E (2003). “Modeling of storm-induced coastal flooding for emergency management”. *Ocean Engineering* **30** (11), pp. 1353–1386.
- Coogan, J & Dzwonkowski, B (2018). “Observations of Wind Forcing Effects on Estuary Length and Salinity Flux in a River-Dominated, Microtidal Estuary, Mobile Bay, Alabama”. *Journal of Physical Oceanography* **48**.8, pp. 1787–1802.
- Cyriac, R, Dietrich, J. C., Fleming, J. G., Blanton, B. O., Kaiser, C, Dawson, C. N. & Luettich, R. A. (2018). “Variability in Coastal Flooding Predictions due to Forecast Errors during Hurricane Arthur (2014)”. *Coastal Engineering* **137**, pp. 59–78.
- Danilov, S (2013). “Ocean modeling on unstructured meshes”. *Ocean Modelling* **69**, pp. 195–210.
- Davies, J. L. (1964). “A morphogenic approach to world shorelines”. *Zeitschrift fur Geomorphologie*.
- Dawson, C. N., Westerink, J. J., Feyen, J. C. & Pothina, D (2006). “Continuous, Discontinuous and Coupled Discontinuous-Continuous Galerkin Finite Element Methods for the Shallow Water Equations”. *International Journal for Numerical Methods in Fluids* **52**, pp. 63–88.
- Defne, Z & Ganju, N. K. (2015). “Quantifying the Residence Time and Flushing Characteristics of a Shallow, Back-Barrier Estuary: Application of Hydrodynamic and Particle Tracking Models”. *Estuaries and Coasts* **38**.5, pp. 1719–1734.
- Dietrich, J. C., Bunya, S, Westerink, J. J., Ebersole, B. A., Smith, J. M., Atkinson, J. H., Jensen, R. E., Resio, D. T., Luettich, R. A., Dawson, C. N., Cardone, V. J., Cox, A. T., Powell, M. D., Westerink, H. J. & Roberts, H. J. (2010). “A High-Resolution Coupled Riverine Flow, Tide, Wind, Wind Wave and Storm Surge Model for Southern Louisiana and Mississippi: Part II – Synoptic Description and Analysis of Hurricanes Katrina and Rita”. *Monthly Weather Review* **138** (2), pp. 378–404.
- Dietrich, J. C., Westerink, J. J., Kennedy, A. B., Smith, J. M., Jensen, R. E., Zijlema, M, Holthuijsen, L. H., Dawson, C. N., Luettich, R. A., Powell, M. D., Cardone, V. J., Cox, A. T., Stone, G. W., Pourtaheri, H, Hope, M. E., Tanaka, S, Westerink, L. G.,

- Westerink, H. J. & Cobell, Z (2011a). “Hurricane Gustav (2008) Waves and Storm Surge: Hindcast, Validation and Synoptic Analysis in Southern Louisiana”. *Monthly Weather Review* **139** (8), pp. 2488–2522.
- Dietrich, J. C., Zijlema, M, Westerink, J. J., Holthuijsen, L. H., Dawson, C. N., Luettich, R. A., Jensen, R. E., Smith, J. M., Stelling, G. S. & Stone, G. W. (2011b). “Modeling Hurricane Waves and Storm Surge using Integrally-Coupled, Scalable Computations”. *Coastal Engineering* **58**, pp. 45–65.
- Dietrich, J. C., Tanaka, S, Westerink, J. J., Dawson, C. N., Luettich, R. A., Zijlema, M, Holthuijsen, L. H., Smith, J. M., Westerink, L. G. & Westerink, H. J. (2012a). “Performance of the Unstructured-Mesh, SWAN+ADCIRC Model in Computing Hurricane Waves and Surge”. *Journal of Scientific Computing* **52** (2), pp. 468–497.
- Dietrich, J. C., Trahan, C. J., Howard, M. T., Fleming, J. G., Weaver, R. J., Tanaka, S, Yu, L, Luettich, R. A., Dawson, C. N., Westerink, J. J., Wells, G, Lu, A, Vega, K, Kubach, A, Dresback, K. M., Kolar, R. L., Kaiser, C & Twilley, R. R. (2012b). “Surface Trajectories of Oil Transport along the Northern Coastline of the Gulf of Mexico”. *Continental Shelf Research* **41** (1), pp. 17–47.
- Dietrich, J. C., Zijlema, M, Allier, P. E., Holthuijsen, L. H., Booij, N, Meixner, J. D., Proft, J. K., Dawson, C. N., Bender, C. J., Naimaster, A, Smith, J. M. & Westerink, J. J. (2013a). “Limiters for Spectral Propagation Velocities in SWAN”. *Ocean Modelling* **70**, pp. 85–102.
- Dietrich, J. C., Dawson, C. N., Proft, J, Howard, M. T., Wells, G, Fleming, J. G., Luettich, R. A., Westerink, J. J., Cobell, Z & Vitse, M (2013b). “Real-time forecasting and visualization of hurricane waves and storm surge using SWAN+ADCIRC and FigureGen”. *Computational Challenges in the Geosciences*. Ed. by Dawson, C. N. & Gerritsen, M, pp. 49–70.
- Dietrich, J. C., Muhammad, A, Curcic, M, Fathi, A, Dawson, C. N., Chen, S. S. & Luettich, R. A. (2018). “Sensitivity of Storm Surge Predictions to Atmospheric Forcing During Hurricane Isaac”. *Journal of Waterway, Port, Coastal and Ocean Engineering* **144** (1).
- DiNapoli, S. M., Bourassa, M. A. & Powell, M. D. (2012). “Uncertainty and Intercalibration Analysis of H*Wind”. *Journal of Oceanic and Atmospheric Technology* **29**, pp. 822–833.

- Dresback, K. M., Blain, C. A. & Kolar, R. L. (2002). “Methods to Compute Baroclinic Pressure Gradients in FE Models”. *Estuarine and Coastal Modeling, Proceedings of the Seventh International Conference*. Ed. by Spaulding, M. L. & Bedford, K. American Society of Civil Engineers, pp. 103–119.
- Dresback, K. M., Kolar, R. L., Blain, C. A., Szpilka, C. M., Szpilka, A. M., Luettich, R. A. & Shay, T (2010). “Development and application of the coupled HYCOM and ADCIRC system”. *Estuarine and Coastal Modeling - Proceedings of the 11th International Conference on Estuarine and Coastal Modeling*. Vol. 388, pp. 259–277.
- Dresback, K. M., Fleming, J. G., Blanton, B. O., Kaiser, C, Gourley, J. J., Tromble, E. M., Luettich, R. A., Kolar, R. L., Hong, Y, Van Cooten, S, Vergara, H. J., Flamig, Z, Lander, H. M., Kelleher, K. E. & Nemunaitis-Monroe, K. L. (2013). “Skill assessment of a real-time forecast system utilizing a coupled hydrologic and coastal hydrodynamic model during Hurricane Irene (2011)”. *Continental Shelf Research* **71**, pp. 78–94.
- Dyer, K (1998). *Estuaries: A Physical Introduction, 2nd Edition*. Wiley.
- Dzwonkowski, B & Yan, X (2005). “Tracking of a Chesapeake Bay estuarine outflow plume with satellite-based ocean color data”. *Continental Shelf Research* **25**.16, pp. 1942–1958.
- Dzwonkowski, B., Park, K. & Collini, R. (2015). “The coupled estuarine-shelf response of a river-dominated system during the transition from low to high discharge”. *Journal of Geophysical Research: Oceans* **120**.9, pp. 6145–6163.
- Edwards, K. P., Werner, F. E. & Blanton, B. O. (2006). “Comparison of Observed and Modeled Drifter Trajectories in Coastal Regions: An Improvement through Adjustments for Observed Drifter Slip and Errors in Wind Fields”. *Journal of Atmospheric and Oceanic Technology* **23**.11, pp. 1614–1620.
- Emanuel, K (2005). “Increasing destructiveness of tropical cyclones over the past 30 years”. *Nature* **436**, pp. 686–688.
- Fathi, A, Dietrich, J. C., Dawson, C. N., Dresback, K. M., Samii, A, Cyriac, R, Blain, C. A. & Kolar, R. L. (2017). “Prediction of surface oil transport in the Northern Gulf of Mexico by using a three-dimensional high-resolution unstructured-grid baroclinic circulation model”. [In Preparation].
- Federal Emergency Management Agency (2008). *Flood Insurance Study, Walton County, Florida*. Tech. rep.
- (2010). *Flood Insurance Study, Walton County, Florida*. Tech. rep.

- Feng, Z & Li, C (2010). “Cold-front-induced flushing of the Louisiana Bays”. *Journal of Marine Systems* **82.4**, pp. 252–264.
- Fleming, J, Fulcher, C, Luettich, R. A., Estrade, B, Allen, G & Winer, H (2008). “A Real Time Storm Surge Forecasting System Using ADCIRC”. *Estuarine and Coastal Modeling (2007)*, pp. 893–912.
- Forbes, C, Luettich, R. A., Mattocks, C. A. & Westerink, J. J. (2010). “A Retrospective Evaluation of the Storm Surge Produced by Hurricane Gustav (2008): Forecast and Hindcast Results”. *Wea. Forecasting* **25**, pp. 1577–1602.
- Fox-Kemper, B & Menemenlis, D (2013). “Can Large Eddy Simulation Techniques Improve Mesoscale Ocean Models?” *Ocean Modeling in an Eddying Regime*. American Geophysical Union, pp. 319–337.
- Fringer, O., Gerritsen, M. & Street, R. (2006). “An unstructured-grid, finite-volume, nonhydrostatic, parallel coastal ocean simulator”. *Ocean Modelling* **14.3**, pp. 139–173.
- Garratt, J. R. (1977). “Review of drag coefficients over oceans and continents”. *Monthly Weather Review* **105**, pp. 915–929.
- Geyer, W. R. (2010). “Estuarine Salinity Structure and Circulation”. *Contemporary Issues in Estuarine Physics*. Ed. by Valle-Levinson, A. Cambridge University Press, pp. 12–26.
- Greer, A. T., Shiller, A. M., Hofmann, E. E., Wiggert, J. D., Warner, S. J., Parra, S. M., Pan, C, Book, J. W., Joung, D, Dykstra, S, Krause, J. W., Dzwonkowski, B, Soto, I. M., Cambazoglu, M. K., Deary, A. L., Briseno-Avena, C, Boyette, A. D., Kastler, J. A., Sanial, V, Hode, L, Nwankwo, U, Chiaverano, L. M., Brien, S. J. O., Fitzpatrick, P. J., Lau, Y. H., Dinniman, M. S., Martin, K. M., Ho, P, Mojzis, A. K., Howden, S. D., Hernandez, F. J., Church, I, Miles, T. N., Sponaugle, S, Moum, J. N., Arnone, R. A., Cowen, R. K., Jacobs, G. A., Schofield, O & Graham, W. M. (2018). “Functioning of Coastal River-Dominated Ecosystems and Implications for Oil Spill Response: From Observations to Mechanisms and Models”. *Oceanography*.
- Guo, X & Valle-Levinson, A (2007). “Tidal effects on estuarine circulation and outflow plume in the Chesapeake Bay”. *Continental Shelf Research* **27.1**, pp. 20–42.
- Handley, L, Altsman, D & DeMay, R, eds. (2007). *Seagrass Status and Trends in the Northern Gulf of Mexico: 1940–2002*. US Geological Survey Scientific Investigations Report 2006–5287, pp. 143–153.

- Haney, R. L. (1991). “On the Pressure Gradient Force over Steep Topography in Sigma Coordinate Ocean Models”. *Journal of Physical Oceanography* **21.4**, pp. 610–619.
- Holland, R. W. (1980). “An Analytic Model of the Wind and Pressure Profiles in Hurricanes”. *Monthly Weather Review* **108**, pp. 1212–1218.
- Holland, W. R. (1978). “The Role of Mesoscale Eddies in the General Circulation of the Ocean—Numerical Experiments Using a Wind-Driven Quasi-Geostrophic Model”. *Journal of Physical Oceanography* **8.3**, pp. 363–392.
- Hope, M. E., Westerink, J. J., Kennedy, A. B., Kerr, P. C., Dietrich, J. C., Dawson, C. N., Bender, C. J., Smith, J. M., Jensen, R. E., Zijlema, M, Holthuijsen, L. H., Luettich Jr, R. A., Powell, M. D., Cardone, V. J., Cox, A. T., Pourtaheri, H, Roberts, H. J., Atkinson, J. H., Tanaka, S, Westerink, H. J. & Westerink, L. G. (2013). “Hindcast and Validation of Hurricane Ike (2008) Waves, Forerunner, and Storm Surge”. *Journal of Geophysical Research: Oceans* **118**, pp. 4424–4460.
- Hoyer, M. V., Terrell, J. B. & Jr., D. E. C. (2013). “Water Chemistry in Choctawhatchee Bay, Florida USA: Spatial and Temporal Considerations Based on Volunteer Collected Data”. *Florida Scientist* **76** (3–4), pp. 453–466.
- Huang, W, Hagen, S & Bacopoulos, P (2014). “Hydrodynamic Modeling of Hurricane Dennis Impact on Estuarine Salinity Variation in Apalachicola Bay”. *Journal of Coastal Research*, pp. 389–398.
- Huguenard, K. D., Bogucki, D. J., Ortiz-Suslow, D. G., Laxague, N. J. M., MacMahon, J, Ozgokmen, T. M., Haus, B. K., Reniers, A. J.H. M., Hargrove, J, Soloviev, A. V. & Graber, H (2016). “On the nature of the frontal zone of the Choctawhatchee Bay plume in the Gulf of Mexico”. *Journal of Geophysical Research: Oceans* **121.2**, pp. 1322–1345.
- Jiayi, P, David, J. A. & Orton, P. M. (2006). “Analyses of internal solitary waves generated at the Columbia River plume front using SAR imagery”. *Journal of Geophysical Research: Oceans* **112**.
- Johnson, D. R., Weidemann, A, Arnone, R & Davis, C. O. (2001). “Chesapeake Bay outflow plume and coastal upwelling events: Physical and optical properties”. *Journal of Geophysical Research: Oceans* **106.C6**, pp. 11613–11622.
- Jones, W. K. & Huang, W (1994). *Hydrodynamic Analysis of the SR 331 Causeway at Choctawhatchee Bay, Florida*. Tech. rep. The Florida Department of Transportation.

- Kakoulaki, G, MacDonald, D & Horner-Devine, A. R. (2014). “The role of wind in the near field and midfield of a river plume”. *Geophysical Research Letters* **41**.14, pp. 5132–5138.
- Kerr, P. C., Donahue, A. S., Westerink, J. J., Luettich, R. A., Zheng, L. Y., Weisburg, R. H., Huang, Y, Wang, H. V., Teng, Y, Forrest, D. R., Roland, A, Haase, A. T., Kramer, A. W., Taylor, A. A., Rhome, J. R., Feyen, J. C., Signell, R. P., Hanson, J. L., Hope, M. E., Estes, R. M., Dominguez, R. A., Dunbar, R. P., Semeraro, L. N., Westerink, H. J., Kennedy, A. B., Smith, J. M., Powell, M. D., Cardone, V. J. & Cox, A. T. (2013). “U.S. IOOS coastal and ocean modeling testbed: Inter-model evaluation of tides, waves, and hurricane surge in the Gulf of Mexico”. *Journal of Geophysical Research: Oceans* **118**, pp. 5129–5172.
- Kim, C.-K. & Park, K (2012). “A modeling study of water and salt exchange for a micro-tidal, stratified northern Gulf of Mexico estuary”. *Journal of Marine Systems* **96-97**, pp. 103–115.
- Koh, T. & Ng, J. S. (2012). “Improved diagnostics for NWP verification in the tropics”. *Journal of Geophysical Research: Atmospheres* **114**.D12.
- Kolar, R. L., Kibbey, T. C. G., Szpilka, C. M., Dresback, K. M., Tromble, E. M., Toohey, I. P., Hoggan, J. L. & Atkinson, J. H. (2009). “Process-oriented tests for validation of baroclinic shallow water models: The lock-exchange problem”. *Ocean Modelling* **28** (1), pp. 137–152.
- Kuitenbrouwer, D, Reniers, A, MacMahan, J & Roth, M. K. (2018). “Coastal protection by a small scale river plume against oil spills in the Northern Gulf of Mexico”. *Continental Shelf Research* **163**, pp. 1–11.
- Lin, N, Emmanuel, K, Oppenheimer, M & Vanmarcke, E (2012). “Physically based assessment of hurricane surge threat under climate change”. *Nature Climate Change* **2**, pp. 462–467.
- Lin, N & Emmanuel, K (2016). “Grey swan tropical cyclones”. *Nature Climate Change* **6**, pp. 106–111.
- Liu, W, Chen, W & Hsu, M (2011). “Using a three-dimensional particle-tracking model to estimate the residence time and age of water in a tidal estuary”. *Computers & Geosciences* **37**.8, pp. 1148–1161.
- Livingston, R. J. (2010). *The Choctawhatchee Bay System Nutrient Report for Florida Department of Environmental Protection*. Tech. rep.

- Luettich, R. A., Westerink, J. J. & Scheffner, N. W. (1992). *ADCIRC: An Advanced Three-Dimensional circulation model for shelves coasts and estuaries, report 1: Theory and methodology of ADCIRC-2DDI and ADCIRC- 3DL*. Tech. rep. United States Army Corps of Engineers.
- Luettich, R. A. & Westerink, J. J. (2004). *Formulation and Numerical Implementation of the 2D/3D ADCIRC Finite Element Model Version 44.XX*. http://adcirc.org/adcirc_theory_2004_12_08.pdf.
- Marshall, J, Adcroft, A, Hill, C, Perelman, L & Heisey, C (1997). “A finite-volume, incompressible Navier Stokes model for studies of the ocean on parallel computers”. *J. Geophysical Res.* **102**.C3, pp. 5753–5766.
- Marsooli, R, Orton, P. M., Fitzpatrick, J & Smith, H (2018). “Residence Time of a Highly Urbanized Estuary: Jamaica Bay, New York”. *Journal of Marine Science and Engineering* **6**.2.
- Martyr-Koller, R. C., Kernkamp, H. W. J., Dam, A van, Wegen, M van der, Lucas, L. V., Knowles, N, Jaffe, B & Fregoso, T. A. (2017). “Application of an unstructured 3D finite volume numerical model to flows and salinity dynamics in the San Francisco Bay–Delta”. *Estuarine, Coastal and Shelf Science* **192**, pp. 86–107.
- Mattocks, C, Forbes, C & Ran, L (2006). *Design and Implementation of a Real-Time Storm Surge and Flood Forecasting Capability for the State of North Carolina*. Tech. rep. University of North Carolina.
- Mattocks, C & Forbes, C (2008). “A real-time, event-triggered storm surge forecasting system for the state of North Carolina”. *Ocean Modelling* **25**, pp. 95–119.
- McDougall, T. J., Jackett, D. R., Wright, D. G. & Feistel, R (2003). “Accurate and Computationally Efficient Algorithms for Potential Temperature and Density of Seawater”. *Journal of Atmospheric and Oceanic Technology* **20**.5, pp. 730–741.
- Mestres, M, Sierra, J. P. & Sanchez-Arcilla, A (2007). “Factors influencing the spreading of a low–discharge river plume”. *Continental Shelf Research* **27**.16, pp. 2116–2134.
- Murphy, P. L. & Valle-Levinson, A (2008). “Tidal and residual circulation in the St. Andrew Bay system, Florida”. *Continental Shelf Research* **28**.19, pp. 2678–2688.
- Murty, P. L. N., Sandhya, K. G., Bhaskaran, P. K., Jose, F, Gayathri, R, Balakrishnan Nair, T. M., Srinivasa Kumar, T & Shenoi, S. S. C. (2014). “A coupled hydrodynamic modeling system for PHAILIN cyclone in the Bay of Bengal”. *Coastal Engineering* **93**, pp. 71–81.

- Nash, J. D. & Moum, J. N. (2005). “River plumes as a source of large-amplitude internal waves in the coastal ocean”. *Nature* **437**.
- National Hurricane Center (2017). *Official Average Track Errors*. http://www.nhc.noaa.gov/verification/figs/ALtkerr_decade_noTD.jpg. [Retrieved 21 August 2017].
- Noble, M. A., Schroeder, W. W., Wiseman, W. J., Ryan, H. F. & Gelfenbaum, G (1996). “Subtidal circulation patterns in a shallow, highly stratified estuary: Mobile Bay, Alabama”. *Journal of Geophysical Research: Oceans* **101**.C11, pp. 25689–25703.
- Ou, S, Zhang, H & Wang, D (2009). “Dynamics of the buoyant plume off the Pearl River Estuary in summer”. *Environmental Fluid Mechanics* **9**.5, pp. 471–492.
- Pan, J, Gu, Y & Wang, D (2014). “Observations and numerical modeling of the Pearl River plume in summer season”. *Journal of Geophysical Research: Oceans* **119**.4, pp. 2480–2500.
- Passeri, D. L., Hagen, S, Bilskie, M & Medeiros, S. C. (2015). “On the significance of incorporating shoreline changes for evaluating coastal hydrodynamics under sea level rise scenarios”. *Natural Hazards* **75**.2, pp. 1599–1617.
- Peng, M, Xie, L & Pietrafesa, L. J. (2004). “A numerical study of storm surge and inundation in the Croatan-Albemarle-Pamlico Estuary System”. *Estuarine, Coastal and Shelf Science* **59**, pp. 121–137.
- (2006). “A numerical study on hurricane-induced storm surge and inundation in Charleston Harbor, South Carolina”. *Journal of Geophysical Research* **111**, pp. 81–101.
- Powell, M. D., Houston, S. H. & Reinhold, T. A. (1996). “Hurricane Andrew’s landfall in South Florida, Part I: Standardizing Measurements for Documentation of Surface Wind Fields”. *Weather and Forecasting* **11**, pp. 304–328.
- Powell, M. D., Houston, S. H., Amat, L. R. & Morisseau-Leroy, N (1998). “The HRD real-time hurricane wind analysis system”. *J. Wind Eng. Ind. Aerodyn.* **77–78**, pp. 53–64.
- Rayson, M. D., Gross, E. S. & Fringer, O. B. (2015). “Modeling the tidal and sub-tidal hydrodynamics in a shallow, micro-tidal estuary”. *Ocean Modelling* **89**, pp. 29–44.
- Resio, D. T., Powell, N. J., Cialone, M. A., Das, H. S. & Westerink, J. J. (2017). “Quantifying impacts of forecast uncertainties on predicted storm surges”. *Natural Hazards* **88** (3), pp. 1423–1449.

- Roth, M. K. (2016). “Material transport in the inner shelf of the northern Gulf of Mexico”. PhD thesis. Monterey, California: Naval Postgraduate School.
- Roth, M. K., Kuitenbrouwer, D, MacMahan, J, Reniers, A & Ozgokmen, T. M. “Along-shelf Currents Forced by Crossshore Winds in the Inner Shelf of the Northeastern Gulf of Mexico”. *Journal of Geophysical Research - Ocean*. [Submitted].
- Roth, M. K., MacMahan, J, Reniers, A., Ozgokomen, T. M., Woodall, K & Haus, B (2017). “Observations of inner shelf cross-shore surface material transport adjacent to a coastal inlet in the northern Gulf of Mexico”. *Continental Shelf Research* **137**, pp. 142–153.
- Safak, I, Wiberg, P. L., Richardson, D. L. & Kurum, M. O. (2015). “Controls on residence time and exchange in a system of shallow coastal bays”. *Continental Shelf Research* **97**, pp. 7–20.
- Shapiro, R (1970). “Smoothing, filtering, and boundary effects”. *Reviews of Geophysics* **8.2**, pp. 359–387.
- Shi, J. Z., Lu, L & Liu, Y (2010). “The Hydrodynamics of an Idealized Estuarine Plume along a Straight Coast: A Numerical Study”. *Environmental Modeling & Assessment* **15.6**, pp. 487–502.
- Sikiric, M. D., Janekovic, I & Kuzmic, M (2009). “A new approach to bathymetry smoothing in sigma-coordinate ocean models”. *Ocean Modelling* **29.2**, pp. 128–136.
- State Climate Office of North Carolina (2017). <http://climate.ncsu.edu/climate/hurricanes/statistics.php>. [Retrieved 21 June 2017].
- Stumpf, R. P., Gelfenbaum, G & Pennock, J. R. (1993). “Wind and tidal forcing of a buoyant plume, Mobile Bay, Alabama”. *Continental Shelf Research* **13.11**, pp. 1281–1301.
- Tarya, A, Vegt, M van der & Hoitink, A. J. F. (2015). “Wind forcing controls on river plume spreading on a tropical continental shelf”. *Journal of Geophysical Research: Oceans* **120.1**, pp. 16–35.
- Taylor, K. E. (2011). “Summarizing multiple aspects of model performance in a single diagram”. *Journal of Geophysical Research* **106** (D7), pp. 7183–7192.
- Tweedley, J. R., Warwick, R. M. & Potter, I. C. (2016). “The Contrasting Ecology of Temperate Macrotidal and Microtidal Estuaries”. *Oceanography and Marine Biology*. Ed. by Hughes, R. N., Hughes, D. J., Smith, I. P. & Dale, A. C. Boca Raton: CRC Press, pp. 73–171.

- UCF (2011a). *Digital Elevation Model and Finite Element Mesh Development*. Tech. rep. Northwest Florida Water Management District and the Federal Emergency Management Agency.
- (2011b). *Flood insurance study: Florida Panhandle and Alabama, Model Validation*. Tech. rep. Federal Emergency Management Agency.
- Uncles, R. J., Stephens, J. A. & Smith, R. E. (2002). “The dependence of estuarine turbidity on tidal intrusion length, tidal range and residence time”. *Continental Shelf Research* **22**.11. Proceedings from the Tenth Biennial Conference on the Physics of Estuaries and Coastal Seas, pp. 1835–1856.
- Valle-Levinson, A (2010). “Definition and classification of estuaries”. *Contemporary Issues in Estuarine Physics*. Ed. by Valle-Levinson, A. Cambridge University Press, pp. 1–11.
- Valle-Levinson, A, Huguenard, K, Ross, L, Branyon, J, MacMahan, J & Reniers, A. (2015). “Tidal and nontidal exchange at a subtropical inlet: Destin Inlet, Northwest Florida”. *Estuarine, Coastal and Shelf Science* **155**, pp. 137–147.
- Vickery, P & Skerlj, P (2005). “Hurricane Gust Factors Revisited”. *Journal of Structural Engineering* **131**, pp. 825–832.
- Wang, B, Giddings, S. N., Fringer, O. B., Gross, E. S., Fong, D. A. & Monismith, S. G. (2011). “Modeling and understanding turbulent mixing in a macrotidal salt wedge estuary”. *Journal of Geophysical Research: Oceans* **116**.C2.
- Warwick, R. M., Tweedley, J. R. & Potter, I. C. (2018). “Microtidal estuaries warrant special management measures that recognise their critical vulnerability to pollution and climate change”. *Marine Pollution Bulletin* **135**, pp. 41–46.
- Webb, B. M. & Marr, C (2016). “Spatial Variability of Hydrodynamic Timescales in a Broad and Shallow Estuary: Mobile Bay, Alabama”. *Journal of Coastal Research*, pp. 1374–1388.
- Westerink, J. J., Luettich Jr, R. A., Feyen, J. C., Atkinson, J. H., Dawson, C. N., Roberts, H. J., Powell, M. D., Dunion, J. P., Kubatko, E. J. & Pourtaheri, H (2008). “A Basin to Channel Scale Unstructured Grid Hurricane Storm Surge Model Applied to Southern Louisiana”. *Monthly Weather Review* **136** (3), pp. 833–864.
- Wilkin, J. L. & Hunter, E. J. (2013). “An assessment of the skill of real-time models of Mid-Atlantic Bight continental shelf circulation”. *Journal of Geophysical Research: Oceans* **118**.6, pp. 2919–2933.

- Xia, M, Xie, L & Pietrafesa, L. J. (2007). “Modeling of the Cape Fear River Estuary plume”. *Estuaries and Coasts* **30.4**, pp. 698–709.
- Xia, M, Xie, L, Pietrafesa, L. J. & Whitney, M. M. (2011). “The ideal response of a Gulf of Mexico estuary plume to wind forcing: Its connection with salt flux and a Lagrangian view”. *Journal of Geophysical Research: Oceans* **116**.C8. C08035.
- Xie, L, Bao, S, Pietrafesa, L. J., Foley, K & Fuentes, M (2006). “A Real-Time Hurricane Surface Wind Forecasting Model: Formulation and Verification”. *Monthly Weather Review* **134**, pp. 1355–1370.
- Yu, X, Guo, X, Morimoto, A & Buranapratheprat, A (2018). “Simulation of river plume behaviors in a tropical region: Case study of the Upper Gulf of Thailand”. *Continental Shelf Research* **153**, pp. 16–29.
- Zhang, Y, Baptista, A. M. & Myers, E. P. (2004). “A cross-scale model for 3D baroclinic circulation in estuary–plume–shelf systems: I. Formulation and skill assessment”. *Continental Shelf Research* **24.18**. Recent Developments in Physical Oceanographic Modelling: Part I, pp. 2187–2214.
- Zhang, Y & Baptista, A. M. (2008). “Selfe: A semi-implicit Eulerian–Lagrangian finite-element model for cross-scale ocean circulation”. *Ocean Modelling* **21** (3), pp. 71–96.
- Zhang, Y, Ye, F, Stanev, E. V. & Grashorn, S (2016). “Seamless cross-scale modeling with SCHISM”. *Ocean Modelling* **102**, pp. 64–81.
- Zheng, Q, Clemente-Colon, P, Yan, X, Liu, W. T. & Huang, N. E. (2004). “Satellite synthetic aperture radar detection of Delaware Bay plumes: Jet–like feature analysis”. *Journal of Geophysical Research: Oceans* **109**.C3.
- Zhong, L, Li, M & Zhang, D.-L. (2010). “How do uncertainties in hurricane model forecasts affect storm surge predictions in a semi-enclosed bay?” *Estuarine, Coastal and Shelf Science* **90**, pp. 61–72.
- Zimmerman, J. T. F. (1976). “Mixing and flushing of tidal embayments in the western Dutch Wadden Sea part I: Distribution of salinity and calculation of mixing time scales”. *Netherlands Journal of Sea Research* **10.2**, pp. 149–191.

APPENDIX

Appendix A

Kalpana Visualization Tool

Kalpana is a Python script that converts ADCIRC output files to ArcGIS compatible shapefiles and Google Earth compatible KMZ files. The code accepts NetCDF formatted ADCIRC outputs for maximum water levels, wind speeds, wave heights and peak wave period and converts these to polyline/polygon shapefiles and polygon KMZ files. The code is also capable of converting timeseries ADCIRC outputs for water levels, wind speeds and wave heights into polygon shapefiles.

Kalpana was built by Rosemary Cyriac, and her efforts were aided by the initial attempts of Rich Signell (USGS) and Rusty Holleman to generate shapefiles from ADCIRC results. Jason Fleming improved Kalpana and incorporated the code into the ADCIRC Surge Guidance System (ASGS) that he maintains at the Renaissance Computing Institute (RENCI). The latest version of the code is maintained at the following GitHub repository: <https://github.com/ccht-ncsu/Kalpana>. Examples with detailed instructions on how to run Kalpana are provided here: <https://ccht.ccee.ncsu.edu/kalpana/>

The user input consists of a netCDF-formatted ADCIRC output file, the selection of output variable to be visualized (time series or maxima of water levels, wave heights, etc.) and the desired number of contour levels. Kalpana uses specialized Python libraries (indicated in parentheses) for reading in netCDF formatted ADCIRC output files (netCDF4), contouring ADCIRC output data (matplotlib), extracting contour information in the form of polygon objects (shapely), and writing them into shape files (fiona) or KMZ (simplekml) files. The shapely polygon objects are processed to remove geometry

errors and separated into outer and inner polygons before being written in the final file format.

There are limitations on the size of a geometric polygon that can be visualized in Google Earth. This is addressed in Kalpana by dividing the entire geographic domain into smaller parts, interpolating mesh and variable data for each part and contouring each part separately. The current KMZ creation capabilities of Kalpana have been specialized for the NC coast. The KMZ creation also permits a user-defined color palette that specifies the contour coloring scheme. The user can also define additional information (legend, logos etc.) as image overlays that form a part of the KMZ file.

Kalpana is a modular code that can be integrated into ASGS such that real-time predictions are converted to shape files and KMZ files, which can be distributed to end users in real-time or archived online. For example, for visualization of Arthur results on the North Carolina ADCIRC mesh (NC9) with a user input of 10 contour levels, the shape file visualization of the maximum water levels (equivalent to one time snap) required 14 sec, while shape file visualization of the time series of water levels (120 time snaps) required 2.5 min. The shape files range in size from 2.12 MB for the former to 379 MB for the latter. The spatial visualizations for model winds, and water levels in Chapter 2 are created from the corresponding shape files generated by Kalpana and visualized in ArcMap 10.1 with ArcGIS satellite imagery overlay.